UCLA

UCLA Electronic Theses and Dissertations

Title

The Study of Extrasolar Planetary Systems through Direct Imaging and Infrared Instrumentation

Permalink

https://escholarship.org/uc/item/5zg9r2nb

Author

Lopez, Ronald Alexander

Publication Date

2023

Peer reviewed|Thesis/dissertation

UNIVERSITY OF CALIFORNIA

Los Angeles

The Study of Extrasolar Planetary Systems through Direct Imaging and Infrared Instrumentation

A dissertation submitted in partial satisfaction

of the requirements for the degree

Doctor of Philosophy in Astronomy and Astrophysics

by

Ronald Alexander Lopez

2023

ABSTRACT OF THE DISSERTATION

The Study of Extrasolar Planetary Systems through Direct Imaging and Infrared Instrumentation

by

Ronald Alexander Lopez

Doctor of Philosophy in Astronomy and Astrophysics

University of California, Los Angeles, 2023

Professor Michael P. Fitzgerald, Chair

Direct imaging and spectroscopy is fundamental to understanding the composition, evolution, and formation of exoplanets, and as such these techniques have been given high priority in the 2020 Decadal Survey on Astronomy and Astrophysics. At its heart, the field of exoplanet science has been driven by advancements in technology and data reduction methods. This thesis focuses on direct imaging techniques, including their applications to circumstellar debris disks and the instrumentation required therein, addressing the following questions: What can we learn about the formation and dynamical history of planetary systems through direct imaging of warped debris disks? How can we improve upon our ability to detect planets and disks through advancements in astronomical instrumentation?

To date, observers have found several debris disks containing asymmetries and warps. Dynamical interactions between planetesimals, dust, radiation, and possibly planets work in tandem to shape dust into distinct morphologies. I discuss the morphological characteristics of the edge-on debris disk around HD 110058 as seen in infrared scattered light by the Gemini Planet Imager, and attempt to probe the dynamical history of the system. The presence

of an asymmetric warp in the disk at a radius of 0.35 arcseconds ($\sim$38 AU) is revealed in PSF-subtracted total-intensity images, reminiscent of the disk around β Pictoris. We discuss the results of scattered-light modeling intended to constrain the three-dimensional morphology of the warp. This complex morphology suggests the existence of large-scale dynamical perturbations due to a possible unseen planet.

As we seek to learn more about the universe, we must continually build astronomical instruments that can uncover more of the inner workings of the physical processes that underlie. Detailed studies of exoplanets and debris disks, such as that of HD 110058, are only made possible by well designed astronomical instruments. Through a set of instrument focused projects I will illustrate the cycle of instrument development from design to data and scientific discovery. With the characterization of the upgraded NIRSPEC detector, I explain the process used to ensure the data taken with the instrument is well-understood. Finally, I illustrate the instrument design process and the steps taken to transform scientific inquiries into instrument designs with the Fabry-Pérot etalon calibration system concept for OSIRIS.

The dissertation of Ronald Alexander Lopez is approved.

Erik A. Petigura

Tuan Do

Smadar Naoz

Michael P. Fitzgerald, Committee Chair

University of California, Los Angeles

2023

To my parents

TABLE OF CONTENTS

LIST OF TABLES

ACKNOWLEDGMENTS

I want to thank the astronomy grad community for making UCLA such an amazing place to study the universe. Thank you to Emily Martin and Pauline Arriaga for setting a wonderful example and always helping me when I needed it. Thank you to Briley Lewis for being the first person I talk to when astronomy gets difficult. Thank you to Adam Trapp and Rick Mebane for keeping me sane through rough times. Thank you to Bao Minh Hoang for always being there and keeping me level headed. I want to thank Maxx Tepper, Olivia Liebman, and Dorian Johnson for being with me through every step of my journey, and being some of the best friends I could have wished for.

I want to thank Kelly Kosmo O'Neil, Sanaea Rose, Tony Pahl, and Veronica Dike for being the greatest cohort I could ever ask for. I will forever cherish the highly helpful and hilarious late-night homework sessions; the transcendently therapeutic tea times; the fantastically fancy functions; the difficult to schedule, yet casually deluxe dinners; and of course the generously giving, gargantuan gold mine that is our group chat. I wouldn't be where I am today if it was not for your never ending support and everlasting friendship.

I want to thank my family for always being there in my time of need. I am so grateful to have such an incredible and dynamic family. You have always believed in me and you never fail to show me your support.

Finally, I want to thank my parents for everything they have done for me. I am who I am because of you, and I am so grateful for all of your sacrifice and love. Thank you for inspiring me at a young age to pursue my dreams and allowing me to stay singularly focussed on my goals. You have always been there for me in the best and worst times of my life, and I am here because of you.

tration. The Observatory was made possible by the generous financial support of the W.M. Keck Foundation. I wish to recognize and acknowledge the very significant cultural role and reverence that the summit of Maunakea has always had within the indigenous Hawaiian community. We are most fortunate to have the opportunity to conduct observations from this mountain.

I acknowledge the results presented in this thesis are based upon published works with additional coauthors, and are reprinted here with permission. Chapter 2 of this dissertation is a version of López et al. (2020) and is reproduced by permission of SPIE. Chapter 3 of this dissertation is a version of López et al. (2022) and is reproduced by permission of SPIE.

VITA

2015–2016	**Undergraduate Research Assistant**, Department of Physics & Astronomy, University of California, Los Angeles, Los Angeles, CA
2015	**B.S., Astrophysics**, University of California, Los Angeles, Los Angeles, CA
2017–present	**Graduate Student Researcher**, Department of Physics and Astronomy, UCLA, Los Angeles, CA
2018–2020	**Teaching Assistant**, Department of Physics and Astronomy, UCLA, Los Angeles, CA. Astronomy 180 – Astrophysics Laboratory (Fall 2018, Fall 2019), Astronomy 6 – Cosmology: Our Changing Concepts of the Universe (Winter 2018) Physics 4AL – Physics Laboratory for Scientists and Engineers: Mechanics (Winter 2019) Astronomy 3 – Nature of the Universe (Spring 2019)
2019	**M.S., Astronomy and Astrophysics**, UCLA, Los Angeles, CA
2020	**Course Development**, Department of Physics and Astronomy, UCLA, Los Angeles, CA. Astronomy 180 – Astrophysics Laboratory (Fall 2020)

PUBLICATIONS

Concept for Calibration of OSIRIS with a Fabry-Pérot Etalon.

López, R., von Raesfeld, C., Fitzgerald, M. P., and Do, T., 2022, Proc. SPIE, 12184, 213

Characterization and performance of the upgraded NIRSPEC on the W. M. Keck Tele-

scope."

López, R. A., Hoffman, E. B., Doppmann, G., Fitzgerald, M. P., Johnson, C., Kassis, M., Lanclos, K., Lyke, J., Martin, E. C., McLean, I., Sohn, J.M., and Weiss, J., 2020, Proc. SPIE, 11447, 114476B

Keck Planet Imager and Characterizer Emission Spectroscopy of WASP-33b
Finnerty, L., ..., López, R. A., 2023, ApJ, 166, 31

Detecting Exomoons from Radial Velocity Measurements of Self-luminous Planets: Application to Observations of HR 7672 B and Future Prospects
Ruffio, J.-B, ..., López, R., 2023, ApJ, 165, 113

Retrieving C and O Abundance of HR 8799 c by Combining High- and Low-resolution Data
Wang, J., ..., Lopez, R. et al., 2023, ApJ, 165, 4

The Atmospheric Composition of a Cloudy Brown Dwarf Companion from High- and Low-Resolution Spectroscopy.
Xuan, J. W., ..., López, R. et al., 2022, ApJ, 937, 54

Phase II of the Keck Planet Imager and characterizer: system-level laboratory characterization and preliminary on-sky commissioning.
Echeverri, D., ..., Lopez, R. et al., 2022, Proc. SPIE, 12184, 66

On-sky performance and lessons learned from the phase I KPIC fiber injection unit.
Finnerty, L., ..., Lopez, R. et al. 2022, Proc. SPIE, 12184, 186

Retrieving the C and O Abundances of HR 7672 AB: a Solar-Type Primary Star with a Benchmark Brown Dwarf.

Wang, J., ..., Lopez, R. et al., 2022, ApJ, 163, 189

Detection and Bulk Properties of the HR 8799 Planets with High Resolution Spectroscopy.

Wang, J. J., ..., Lopez, R. et al., 2021, ApJ, 162, 148

The Keck Planet Imager and Characterizer: A dedicated single-mode fiber injection unit for high resolution exoplanet spectroscopy.

Delorme, J.-R., ..., Lopez, R. et al., 2021, JATIS, 7, 035006

Debris Disk Results from the Gemini Planet Imager Exoplanet Survey's Polarimetric Imaging Campaign.

Esposito, T. M., ..., Lopez, R. et al., 2020, ApJ, 160, 24

The Gemini Planet Imager View of the HD 32297 Debris Disk.

Duchêne, G., ..., Lopez, R. et al., 2020, ApJ, 159, 251

CHAPTER 1

Introduction

For many years, planet formation theories were based solely from knowledge of our own solar system. The observed dichotomy between the inner rocky planets and outer gas giants suggested that the ice that formed beyond the "ice-line" could more easily create protoplanetary cores. This abundance of mass makes it easier for protoplanets to accrete great amounts of gas before it can be blown out by the star, creating gas giants (Stevenson, 1982). While this process is still believed to be an important mechanism in planet formation, we have discovered thousands of new planets outside of our own system which challenge the simpler models we have had in the past (Lissauer, 1993). Many of these systems look surprisingly different from our own, and as such, planet formation theory has evolved to reflect this. Giant planets, found close to their host stars (Mayor & Queloz, 1995), have enhanced our view of system dynamics, and the discovery of super-Earths (Rivera & Lissauer, 2001) and sub-Neptunes have expanded on the process in which planets accrete mass (Bean et al., 2021).

With the detection of circumstellar disks, we have been able to paint a much broader picture of planet formation starting from the earliest stages of solar system formation. As a molecular cloud gravitationally collapses, it begins the formation of protostars. Around these protostars, the cloud of gas and dust begins to flatten out in a battle between gravity and angular momentum into a thick disk of material known as protoplanetary disks. These disks are the nurseries for the formation of new planets. As the star collapses further, its density and temperature increase enough to ignite fusion in its core and it begins to emit a flood

of photons and a powerful stellar wind. This radiation-driven force begins to remove the gas from the disk, slowly depleting these gas rich protoplanetary disks (Williams & Cieza, 2011). In this phase, these disks become known as transition disks. Over time, most of the gas has either been accreted onto the star, onto large bodies, like planets, or ejected from the system, leaving behind only dust.

However, this dust does not remain in the system long enough to be observable during the long lifetimes of main sequence stars. Small dust grains are subject to the same radiative forces as the gas, and will eventually be ejected from the system, or fall in towards the star via Poynting-Robertson drag (Burns et al., 1976). As such, debris disks are not simply the remnant disks of dust left over from star formation; they can exist for time periods longer than the expected lifetime of the dust that composes them. Their prolonged existence suggests that they must be replenished by a dynamical mechanism capable of creating new dust (Hughes et al., 2018a). The most common explanation for this dust creation is collisional cascade: the process in which planetesimals continuously collide, creating smaller and smaller grains (Dohnanyi, 1969; Pan & Schlichting, 2012).

Debris disks may continue to exist long enough to be molded by the dynamics occurring in their host systems. Disk features, like sharp edges and gaps, can be used as hints to the locations of unseen planets in the same way Saturn's rings are carved out by moons. Warps and asymmetries may reveal the influences of major dynamical events such as stellar fly-bys, ISM interactions, large collisions, and misaligned planets. Thus, the morphology of the disks can often shed light onto the dynamical history of the system, even when the dynamical processes that shaped them remain unseen (Wyatt et al., 1999; Lee & Chiang, 2016).

With the trove of information we can gather from disks, it is unfortunate that only a handful have been resolved, and even fewer studied spectroscopically. The ability to image the morphological structures and study the compositions of these disks is crucial for our understanding of system formation. Specialized coronagraphic integral-field spectrographs (IFSs)

built behind extreme adaptive optics (AO) systems, such as GPI (Macintosh et al., 2014), SPHERE (Beuzit et al., 2019) and CHARIS (Groff et al., 2015), are excellent at creating high-contrast regions and directly imaging faint disks and planets, however they are still limited in their capabilities. The inner regions of disks, where we might find the location of "ice-lines" or sharp inner edges, are out of reach with the inner-working angles of current instruments. Resolving thin gaps and imaging abnormal features, like "clumps", are challenging with current methods of direct imaging and data reduction. The ability to characterize smaller, dimmer, planets through direct imaging and spectroscopy will add to our knowledge of extrasolar system architecture and expand the parameter space of exoplanet demographics. Analyzing these planets in detail will bridge the gap between the systems that we detect directly, the systems we detect indirectly, and the systems much like our own that are too difficult to detect. For this reason, great efforts are being put into advancing extreme adaptive optics, coronagraphy, speckle suppression, and high resolution spectroscopy in order to better detect and characterize disks and planets close to their host stars (Snellen et al., 2015). The ability to image disks and planets in the same systems dramatically aids in the understanding of planet-disk interactions and the dynamical effects of planet formation.

New technologies improve our ability to see fainter objects, take more precise spectroscopic data, and take detailed observations through the aberrations caused by the earth's atmosphere. As such, new instruments are continually being developed and upgraded leveraging such technical developments. The advancement of astronomical instrumentation enables new and exciting observations, and in turn advances our theories of the universe. In these works I will address all three of these aspects of astronomical research through the characterization of the upgraded NIRSPEC detectors, the design concept for a new calibration system for OSIRIS, and the direct imaging of the HD 110058 debris disk. With these works I aim to push instrumentation and observation toward the ultimate goal of finding signs of life through the imaging and characterization of Earth-like planets around Sun-like stars.

In Chapter 2 I characterize the spectrometer detector and slit-viewing camera on the newly upgraded NIRSPEC instrument on the W. M. Keck II Telescope. Through the use of photometry and spectroscopy of standard stars and internal calibration lamps, we assess the performance of the upgraded spectrometer detector and slit-viewing camera detectors. In doing so, I address a light leak in the system and describe the steps taken to attempt to mitigate the problem and eliminate improbable causes.

In Chapter 3 I present the design requirements and initial design concept for a Fabry-Pérot etalon calibration system for use on the OSIRIS instrument on the Keck I telescope. The aim of this concept is to produce evenly spaced calibration lines at high densities tuned specifically for OSIRIS that can be used to the overall spectral calibration process.

In Chapter 4 I examine the debris disk around the 17 Myr old, A0V star HD 110058 in the Scorpius-Centaurus region. I analyze H-band, total-intensity images taken with GPI's polarimetry mode to characterize the warp of HD 110058's debris disk. The unique complexity of the disk points to significant dynamical processes, possibly caused by perturbations from an unseen planet. Under this consideration, we estimate the timescale and possible planet-system architecture that may be consistent with the warp seen in HD 110058.

CHAPTER 2

Characterization and Performance of the Upgraded NIRSPEC on the W. M. Keck Telescope

2.1   Introduction

NIRSPEC is a near-infrared echelle spectrograph on the W. M. Keck II telescope commissioned in 1999. McLean et al. (1998, 2000) NIRSPEC's cryostat is equipped with two detectors: a slit viewing camera (SCAM) and a spectrometer detector (SPEC). The SPEC detector is sensitive to a wavelength range of 1-5 μm and capable of both low resolution (R$\sim$2000) and high-resolution (R$\sim$25,000) observations. As part of the 2018 NIRSPEC upgrade (Martin et al., 2018), both the SCAM and SPEC detectors were replaced in order to improve the sensitivity and longevity of the instrument. The original Aladdin III InSb 1024$\times$1024 array used in SPEC was replaced by a Teledyne Hawaii-2RG (H2RG) HgCdTe 2048$\times$2048 array. The H2RG's larger detector size and smaller (18 μm) pixel size enables increased sensitivity and higher signal-to-noise measurements. The original PICNIC 256$\times$256 array in SCAM has also been replaced by an engineering-grade H2RG, increasing the sensitivity range of SCAM from 1–2.5 μm to 1–5 μm. The use of the full 2048$\times$2048 array of the SCAM H2RG is not needed as the field of view is small enough to use only a portion of the detector. Using a 256$\times$256 sub-array allows for faster readout speeds. Here we report the characteristics of the upgraded detectors, along with helpful information for the use of NIRSPEC on sky. In Section 2.2, we discuss the characterization of the SPEC detector and

in Section 2.3, we discuss the characterization of the SCAM detector. In Section 2.5, we summarize the analysis done in this paper.

2.2 SPEC

The SPEC detector is the workhorse of NIRSPEC. SPEC is primarily used in taking high-resolution spectra in a large wavelength range (1–5 μm) and has produced many successful scientific results ranging from solar system science to extragalactic astronomy (McLean, 2005). In Section 2.2.1 we report the gain of the SPEC detector. In Section 2.2.2 we discuss the instrument background. In Section 2.2.3 we discuss the read noise and suspected contributions from the instrument background on the read noise levels. In Sections 2.2.4 and 2.2.5 we report the flux zero points and throughput for the NIRSPEC filters N1, N3, N5, and N7. In Section 2.2.6 we briefly discuss the persistence of the detector. In Sections 2.2.7 and 2.2.8 we report the the pixel scale and spectral dispersion of SPEC. Lastly, in Section 2.2.9 we discuss and provide a map of the resolving power across the detector.

2.2.1 Gain

The first step we take in understanding the behavior of the SPEC detector is measuring the gain. Here we measure the conversion gain, the ratio of photoelectrons (e^-) per analog-to-digital unit (ADU). We use a series of flat-field exposures with increasing exposure times to measure the gain. First, a bad pixel map is created by taking the ratio between two flats of different exposure times and marking pixels with values 3-sigma outside the value expected for the ratio of normal pixels. The bad pixel map is applied to each image, removing hot and cold pixels from consideration. The calculation of the gain follows a simplified and modified version of the methods described in (Mortara & Fowler, 1981). We first take the difference between the flats, however, during the process of taking flats, the lamp increases in temperature and flats taken later in the run tend to be brighter than those taken earlier. To compensate for this, we take the ratio between two flats with equal exposure times and

use this as a scaling factor to normalize the first image to the same light level as the second. Once this correction is made, the flats should be scaled to the same light level and can be differenced. The gain itself is determined by the slope of the relationship between the mean and variance of the differenced frame. In Figure 2.1, we plot the means and variances of flat field pairs of increasing exposure time and overplot a linear fit to the data, yielding a gain of $3.01 \pm 0.08 \ e^-/ADU$.
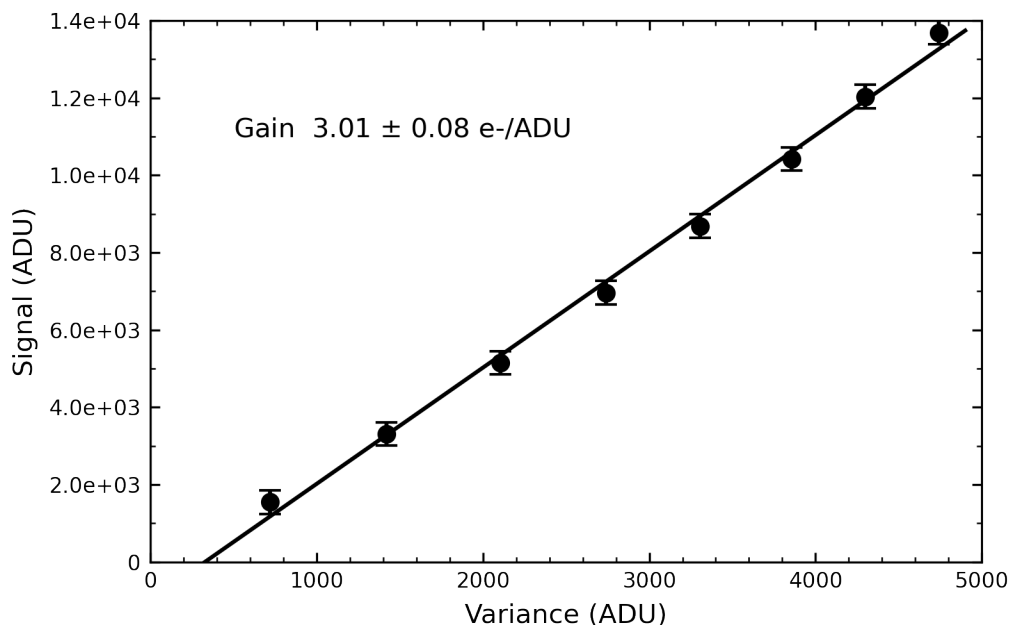
Figure 2.1: SPEC detector gain. The mean values of the processed flat images are plotted on the Y axis and the variance on the X axis. The gain is the slope of the best-fit line, which we measure to be 3.01 ± 0.08 e^-/ADU.

2.2.2 Instrument Background

In this section, we characterize the signal recorded when there are no expected photons interacting with the detector. In normal circumstances the background level of the detector is dominated by the dark current which builds over time. For this paper, we will simply refer to this as the "instrument background" ascribed to a potential light leak contributing to the background levels by thermal photons. We determine this background by measuring

the signal of dark frames of increasing exposure times. The background is calculated by taking the mean of the dark frames after removing bad pixels. The signal is then plotted against integration time in Figure 2.2 and fit with a line to determine the rate of change of the instrument background and integration time. The slope of this line is then multiplied by the gain to yield an instrument background of $0.7 \pm 0.10 \ e^-/s$.
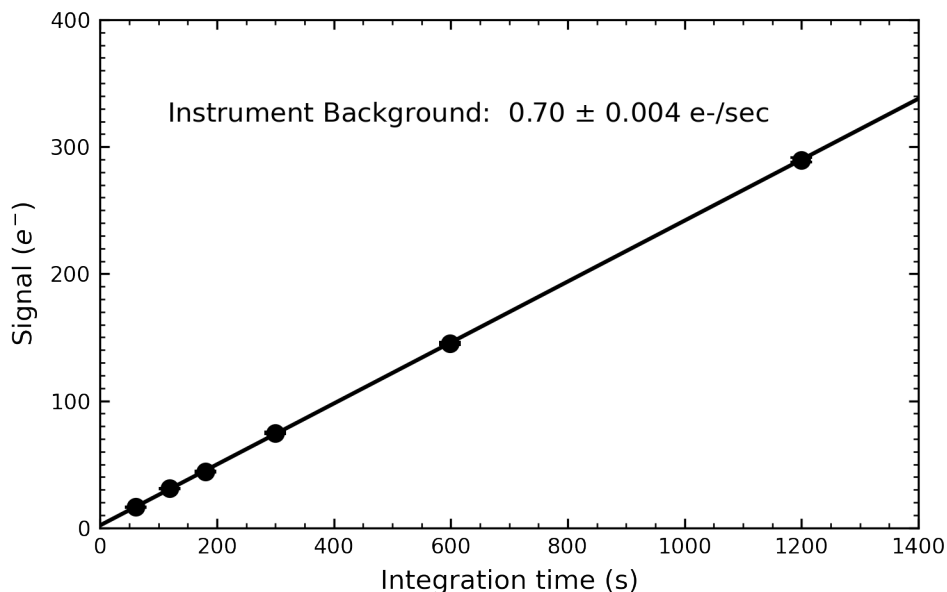
Figure 2.2: The instrument background is determined using the slope of the best fit line to the signal measurements. We measure an elevated background level of $0.7 \pm 0.10 \ e^-/s$ which is consistent with a light leak and is at or below that from previous array.

A major motivation for the detector upgrade to the H2RG was the promise of a much reduced dark current than the Aladdin III. The H2RG array is manufactured to achieve dark currents of less than $0.05 \ e^-/s$ (Blank et al., 2012). The elevated background signal we measure is consistent with a light leak. Figure 2.3 shows an example dark frame with an exposure time of 20 minutes. The long exposure time makes it easy to see contributions from a large external signal. In Figure 2.3, we plot a histogram of the background levels across the entire frame. For an instrument background dominated by dark current, we expect one

peak in the background rate, however the histogram shows multiple peaks. This elevated background is also consistent with background levels of the previous Alladin III, measured to be between 0.7–1.0 e^-/s. This suggests that the light leak may have gone undetected in the old configuration. Attempts to identify and correct the source of the light leak are ongoing. So far, modulation of the slit, the echelle grating, and the cross-disperser do not appear to modulate the pattern, suggesting the leak is occurring in the backend camera.
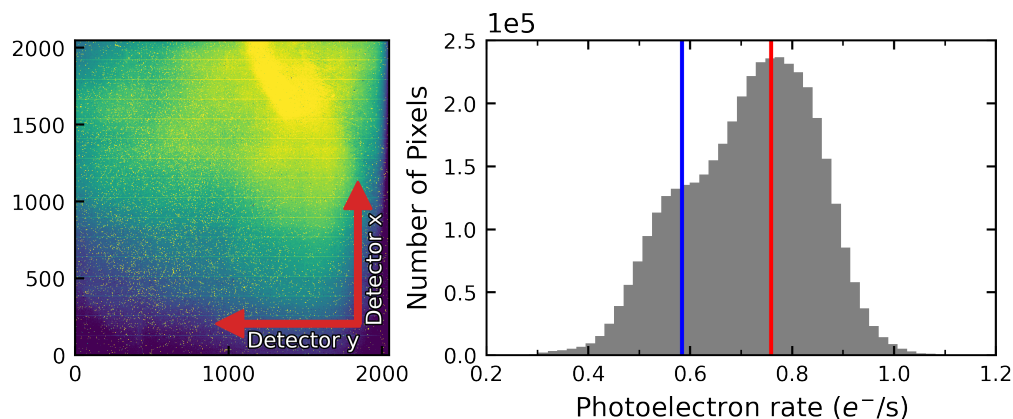
Figure 2.3: Left: sample 20-minute dark frame. With long exposure times, the elevated signal can be seen clearly in the upper right corner of the frame. Right: histogram of the photoelectron rate in e^-/s. The blue and red lines are the peaks of two distributions that contribute to the elevated instrument background.

2.2.3 Read noise

We further characterize the SPEC detector by measuring the read noise. Knowledge of the read noise levels is important for short-exposure time performance of the spectrometer. To measure the read noise, we take the difference between two dark frames of equal exposure time, compute the standard deviation, and divide by $\sqrt{2}$ to compensate for double counting. This gives us a measurement of the noise in a single frame. This is done for 5 pairs of dark frames, all of equal exposure times. The mean of these 5 measurements gives the final noise value and the variance of these values gives the uncertainty on the mean read noise. The noise in ADU is multiplied by the gain to convert to electrons. This process is then repeated

9

for dark exposures of increasing number of reads and exposure time. The increase in exposure time is needed to compensate for the 1.5 s clock time of reading out the detector. For this experiment, the array is read out using either correlated double sampling (CDS) or multiple correlated double sampling (MCDS) modes. Thus for each set, N refers to the number of Fowler pairs, or the number of reads taken at the beginning and end of each exposure. For example, CDS corresponds to $N = 1$ and MCDS 16 corresponds to $N = 16$.

Figure 2.4 provides the measured value of read noise as a function of number of Fowler pairs. We expect that for uncorrelated noise which has the same value for all reads, the noise should decrease as $\sqrt{N}$. While we do see a decrease in read noise, it goes as $N^{-0.42}$. The difference in the exponent is likely due in part to the elevated instrument background that we observe in Figure 2.3. The exposure time increases with the number of reads due to the time required to read out the detector. As a consequence, the exposures with more reads receive non-negligible shot noise contributions from the elevated instrument background. In an attempt to remove the bias caused by the background, we subtract out the variance of the background from the measured noise data, which for Poisson distributions is just the mean of the dark frames. In Figure 2.4, we plot both the measured read noise as well as the bias subtracted noise. In an attempt to find the exact relation between read noise and number of reads, we fit a power law to all of these data except the last point. We exclude the last point at 16 reads because we suspect that noise contributions from other sources begin to dominate, thus the $1/\sqrt{N}$ behavior begins to break down greatly. The contribution of the shot noise is negligible at a small number of reads, but becomes significant at around 8 reads. This effect is non-negligible for longer exposure times and is most likely a strongly contributing factor to a higher than normal read noise. However, additional unseen contributions to these elevated noise levels may still exist.
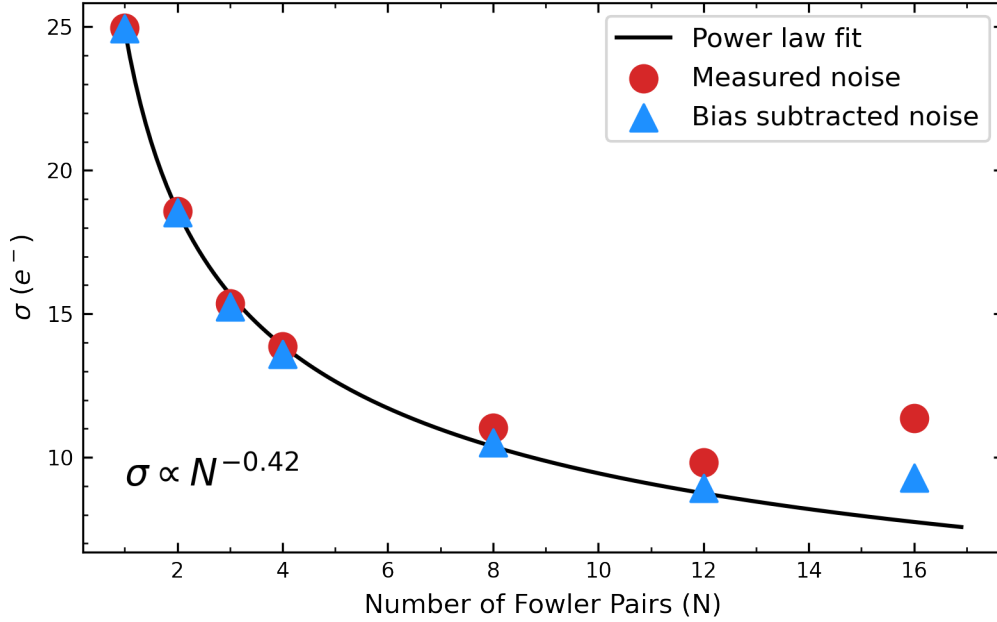
Figure 2.4: Read noise as a function of number of reads (Fowler pairs). The red points are the measured noise values from the raw dark frames. The Blue triangles are the bias subtracted noise measurements calculated by subtracting the variance of the instrument background from the noise measurements. A power law is fit to all the bias subtracted noise data except for the 16 reads point. The read noise decreases as a power law with power -0.42.

2.2.4 Zero points

We further characterize the SPEC detector by determining the zero points for the following filters: NIRSPEC-1, NIRSPEC-3, NIRSPEC-5, and NIRSPEC-7, which roughly correspond to the Y, J, H, and K bands respectively. Flux zero points provide a reference point for the signal strength on the detector for an astronomical source of known magnitude. They are helpful in characterizing instruments with non-standard filter sets and are useful for observation planning and assessing the performance of new detectors. On 2020 December 3rd, we took two exposures of the spectroscopic standard star SA 96-83 in each of the filters listed above using the $0.720'' \times 12''$ slit. We define the zero point as the monochromatic flux in Janskys corresponding to a signal of 1 ADU/s on the detector.

The SPEC zero points are determined by the total flux of the continuum of a standard star at a reference wavelength close to the band center. The reference wavelength is chosen by first identifying bright telluric emission lines in a high signal-to-noise region of the detector. These lines are used as a reference to determine the spectral dispersion locally, which allows for an accurate measure of the wavelength in a portion of the continuum between the telluric lines. Once a reference wavelength has been chosen, we take a 20-pixel-wide cut of the continuum in the spectral dimension centered at that wavelength and sum along the spatial dimension. Over this wavelength range, the continuum brightness is effectively constant, so this measurement of the mean brightness of the star accurately represents the star brightness at the reference wavelength. The uncertainty in this measurement is taken from the spread of each individual brightness measurement.

The average signal, divided by the integration time, provides a measure of flux in ADU/s. The known magnitude of the star is then converted to Janskys using the methods described in Tokunaga & Vacca (2005), which contain conversion factors for the Mauna Kea Observatories near-IR filters. The conversion to monochromatic flux is defined at the isophotal wavelength, which is close but not equal to the reference wavelength used to determine the measured flux on the detector. We apply a small correction to the star flux by generating a blackbody curve using the spectral type of the star and calculating the ratio between the fluxes at the reference wavelength and the isophotal wavelength. The corrected star flux is then divided by the measured flux on the detector to determine the zero point flux in Janskys corresponding to 1 ADU/s. (See Table 2.1).

2.2.5 Throughput

Light can be extincted as it propagates through the atmosphere and through the instrument. Light is lost due to effects from the atmosphere, mirrors, filters, the slit, and several other potential sources. The total loss in transmission is the total throughput of the instrument. We aim to calculate the throughput in each of the four NIRSPEC filters by comparing the

Table 2.1: SPEC Flux Zero Points.

Filter	Zero point (mJy)	Throughput (%)
NIRSPEC-1 (Y)	1.6 ± 0.3	17.0
NIRSPEC-3 (J)	1.80 ± 0.06	15.7
NIRSPEC-5 (H)	2.73 ± 0.11	9.7
NIRSPEC-7 (K)	1.09 ± 0.04	23.5

expected photon rate from the star to the measured photon rate on the detector. We use the same data and methods described in Section 2.2.4 to derive a flux in Janskys and convert this value into a photon flux using the reference wavelength for the photon energy. The photon flux is then multiplied by the Keck telescope collecting area of 72 m^2, as reported by the observatory, and multiplied by the dispersion at the reference wavelength to account for a one-pixel-wide flux measurement on the detector. The measured flux in ADU/s/px is divided by the expected flux in ADU/s/px, providing the throughput. We list these values in Table 2.1. The measure of throughput is highly dependent on the seeing and slit loss, and these numbers can change depending on other observing conditions, but should be accurate at their order of magnitude level.

2.2.6 Persistence

Persistence refers to the charge that remains on the detector after a light source has been removed. Persistence can be an issue when taking an exposure after taking an image of a bright source. To characterize the persistence, we conduct an experiment using a group of saturated pixels. We took an exposure of a very saturated emission line then took a long exposure (1200 s) dark in quick succession and could not detect any residual signal within the noise ($\sigma = 13 \ e^-$) of the same pixel region.

2.2.7 Pixel Scale

We calculate the pixel scale using the separation of known double stars aligned in the slit. Observations of the double star Struve 751 were taken in high-resolution mode using the N7 filter and $0.288'' \times 24''$ slit on 2020 December 3. Observations of UCAC 529-038252 were taken in low-resolution mode using the N1 filter and $42'' \times 0.380''$ slit on 2019 March 23. In both data sets, the thermal emission of the stars produces two traces on the detector along the wavelength dimension as shown in Figure 2.5. We calculate the plate scale by measuring the physical separation between the traces on the detector along the spatial dimension of the slit. The traces do not align with the orientation of the pixels due to their curvature. To account for this misalignment, the true separation was calculated by fitting a line to segments of each trace and a telluric line that bisects the two traces (Figure 2.5). The intersection of each trace with the telluric line produces a pair of coordinates which we use to calculate the pixel separation, and thus the physical distance between the traces. This measurement was calculated three times using different telluric lines and averaged to get the final measurement.
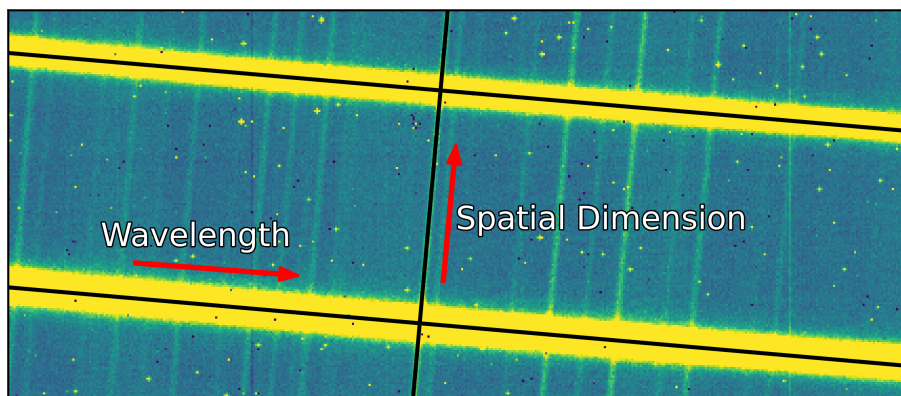
Figure 2.5: Double star image in low resolution mode depicting the two traces of the binary. The black lines are linear fits to the telluric line and stellar traces. The intersection of each pair of lines allows for accurate measures of the pixel separation of the two stars.

As outlined in Section 2.3.2, in low-resolution mode, we use an angular separation of $10.927 \pm 0.023''$ for the double star UCAC 529-038252, leading to a pixel scale of $0.098 \pm 0.004''$/px. For

the high-resolution mode measurement, we use the angular separation of Struve 751 which is estimated using the most recent observations from Schlimmer (2015) with an uncertainty based on the motion of the stars and the time since last observation. Using an angular separation of $15.54 \pm 0.2''$, we measure a pixel scale of $0.13 \pm 0.03''/px$.

2.2.8 Spectral Dispersion

The spectral dispersion is a measure of the change in wavelength on a per pixel basis, analogous to the pixel scale in wavelength space. The dispersion is dependent on the order and thus cannot be calculated using the same method as the pixel scale. Using IRAF packages `identify` and `dispcor`, we fit low order polynomials to arc lines of known wavelength. This gives a $\Delta\lambda/\text{px}$ which is unique for each echelle order and uniform within each order.

In Figure 2.6, we plot the spectral dispersion as a function of order m and anchor a curve to the order $m = 60$. As expected for grating spectrometers, the spectral dispersion is inversely proportional to the order. Other than a few outliers, this curve matches very closely to the dispersion measurements.

2.2.9 Resolution Across the field

NIRSPEC was originally designed for a 1024×1024, 27-μm pixel Aladdin III, which set the optical prescription for the backend camera three-mirror anastigmat. The H2RG is physically larger, and can achieve greater spectral grasp, albeit at potentially reduced optical performance. Here we characterize the resolving power as a function of position in order to assess performance over the entire field of view and identify the highest resolution region of the detector. In order to determine the change in resolution across the detector, we measured the width of a large sample of calibration lines placed in varying positions on the detector. We used a series of 245 individual 1.5 s exposures taken with NIRSPEC's N5 filter and the $0.288'' \times 12''$ slit. Each frame contains an average of $\sim$50 spectral lines from 4 calibration lamps (Argon, Krypton, Xenon, Neon) for a total of 11,750 data points. By stepping the

$$\frac{d\lambda}{dx} = d_0\left(\frac{60}{m}\right)$$

$$d_0 = 0.122455\frac{\text{Å}}{px}$$
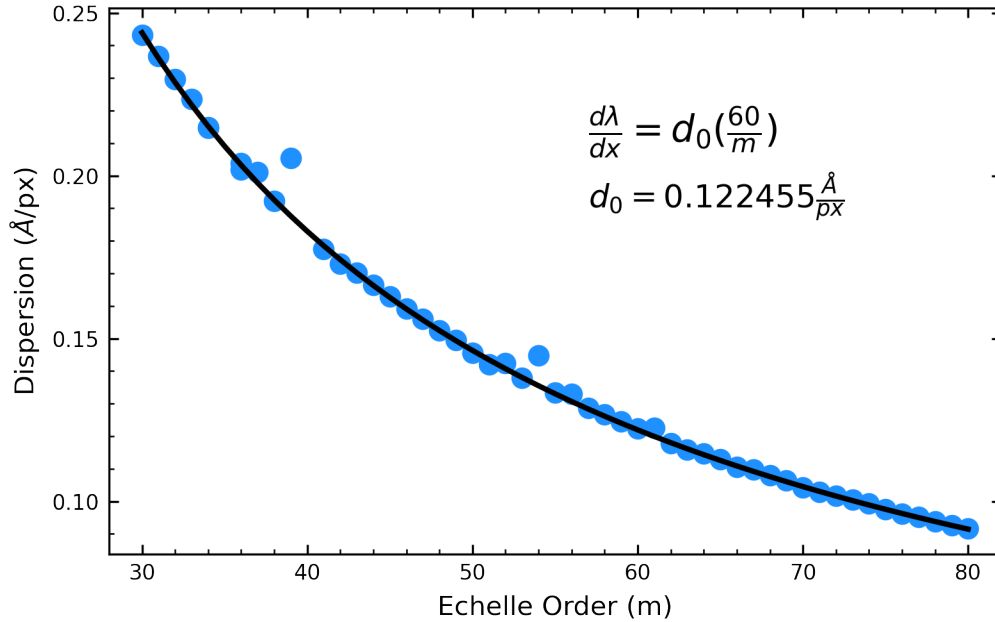
Figure 2.6: The spectral dispersion as a function of echelle order in the high-resolution mode on NIRSPEC. The curve is not a fit, but instead a curve anchored on the order $m = 60$. Other than a few outliers, the spectral dispersion is inversely proportional to echelle order m as expected for an echelle spectrograph.

spectra across the detector between each exposure, we ensured robust coverage of the entire frame. Each set of calibration lines are shifted in each exposure by altering the echelle and cross-disperser angles by 0.2° in order to obtain adequate coverage of the entire field. The exposures span a range of 62.0°–64.0° in echelle angle and 34.0°–38.0° in cross-disperser angle.

2.2.9.1 Measuring Line Width

The first step we take in determining the resolution across the field is creating a line finding algorithm that can reject unusable data like lines cut off by the edge of the detector. This algorithm takes in a NIRSPEC image, locates the positions of spectral lines and determines if the selected lines should be used in the analysis. The algorithm rejects lines that are either saturated or too dim, and rejects doublets or lines that are too close to each other. Each spectral line on the frame is uniquely angled relative to the orientation of the rows and

columns of pixels on the detector due in part to the quasi-Littrow spectrometer configuration. For this reason, we do a line fit to each spectral line to find the angle of rotation locally and then de-rotate it. The width of a line is the FWHM of a Gaussian profile fitted to a row of pixels perpendicular to the emission line. This process is done for each row of pixels perpendicular to the line, creating a set of 40 width measurements per line. The median width value is used as the final width measurement of the line. This process is done for every identified line in the frame and is repeated for every exposure. The result is a large set of width measurements and their associated positions in the field.

2.2.9.2 Resolution Map

To create the map, we use the scikit-learn Birch clustering algorithm (Pedregosa et al., 2011) to group the line width measurements based on their position on the detector. Each group contains a set of width measurements in a cell that are averaged to determine the resolution of the detector in their region. The position of the cell is determined by the geometric mean of each point in the group. A Voronoi diagram is then generated using these cells as seeds. The Voronoi diagram represents the mean resolution in each cell designated by a single color. The result is a color map illustrating the resolution across the detector as seen in Figure 2.7. The Voronoi diagram resembles a "plus" pattern with the lowest resolution in the corners and the highest resolution in the middle of the pattern. This pattern is consistent with the predictions of Martin et al. (2014) which demonstrate, via ray tracing, a larger RMS spot size on the edges of the detector, with the largest spots in the corners. This result is not surprising as the optical performance is expected to be worse in these regions. Taking this into consideration, an observer can prioritize specific wavelengths in the highest resolution region of the detector by manipulating the echelle and cross-disperser angles.

2.3 SCAM

SCAM is used for target acquisition and guiding, providing a 40″ field of view surrounding each selected slit of the spectrograph. In Section 2.3.1 we report the magnitude zero points in the NIRSPEC filters N1, N3, N5, and N7. In Section 2.3.2 we report the pixel scale. In Section 2.3.3 we discuss in length our methods and results for the SCAM geometric distortion.

2.3.1 Zero points

To determine the zero points for SCAM, images of the UKIRT Faint Standard star FS 20 (G163-50; α = 11 07 59.93, δ = -05 09 26.1) were taken on 2019 March 23. Exposures at the minimum time were taken across the SCAM field in a square dither pattern with the star positioned off the slit. Four to nine exposures, 0.655 s each, were obtained in filters N1, N3, and N5, both with and without the short bandpass. For N7, images of the UKIRT Faint Standard star FS 10 (GD 50; α = 3 48 50.2, δ = -00 58 32) were taken 2020 December 3. Six exposures, 9.83 s each, were obtained in filter the N7 with only the short bandpass (called 'short' in Table 2.2). Filters N1, N3, N5, N7 correspond approximately to Y, J, H, and K bandpasses, respectively. The FS 20 images were reduced using standard techniques, specifically dark and sky subtraction, flat-fielding, and bad-pixel masking. Due to the small amount of data for each filter and the occasional bad pixels directly on the star, we attempt to reduce noise in our data by replacing the masked pixels by the median of the 4-pixel radius circle around it. Each the star radius is comparatively 14 pixels. The zero points for each image are calculated individually and then converted to magnitudes corresponding to 1 ADU/s. The average for each filter was taken as the final result.

The SCAM zero point in N3 was found to be about 26.1 magnitudes, while the magnitude reported in McLean et al. (2000) was 24.7. The improved sensitivity may be due to increased quantum efficiency of the new detector.

Table 2.2: SCAM Magnitude Zero Points.

Filter	Zero point Magnitude	Uncertainty
NIRSPEC 1	26.30	0.03
NIRSPEC 1 + short	26.26	0.01
NIRSPEC 3	26.11	0.02
NIRSPEC 3 + short	26.08	0.01
NIRSPEC 5	26.28	0.02
NIRSPEC 5 + short	26.22	0.02
NIRSPEC 7 + short	24.4	0.1

2.3.2   Pixel Scale

To determine SCAM's pixel scale, 30 images of the optical double star UCAC 529-038252 were taken with the target off the slit on 2019 March 23 (WDS 07106+1543; $\alpha = 07\ 10\ 37.92$, $\delta = +15\ 43\ 14.2$). Using the separation and proper motion measurements from Dugan et al. (2019) we calculated the arcsecond separation by inserting the date for our night of observations into their equations of motion. We determined that the separation on our night was $10.86 \pm .023''$ which we divided by the averaged pixel separation to determine the scale. With an average separation of 69.1 ± 0.3 pixels, the pixel scale of SCAM was found to be $0.157 \pm 0.001''/\text{px}$.

2.3.3   Distortion

Optical distortion describes the changes in image magnification across the field of view, a consequence of the optical system. This effect means that the pixel scale can change across the detector, increasing error involved with acquisition and guiding. Mapping the distortion can reduce this error and allow for more accurate and reliable slit placement.

The 10 SCAM images of the Palomar 2 globular cluster used in this characterization were

taken on 2019 March 21, with an exposure time of 5 s in the filter N1. Our methods follow the concept of 'self-calibration' and involve no external data Libralato et al. (2014). The data contains exposures of Palomar 2, each taken on overlapping fields of view but shifted by at least a few arcseconds across.

Determining the distortion across the detector involved four major steps. We first catalogued the stars in their individual frames, which are within the detector exposure reference frame (Section 2.3.3.1). Second, we optimized their average positions in a larger master frame, which are in the reference frame of actual positions (Section 2.3.3.2). Third, we applied up to 4th-order polynomials to the transformation from the observed frames to the master frames (Section 2.3.3.3). The polynomial coefficients describe the best fit of the distortion across a single frame. Lastly, we conducted an array of tests to improve confidence in the solution (Section 2.3.3.4).

2.3.3.1 Identifying and Cataloguing Stars

The images were reduced using standard techniques, specifically dark and sky subtraction, flat-fielding, and bad-pixel masking. After basic data reduction, we designed a script that identifies stars through three major steps. In the first step, the script smooths each image with `scipy.ndimage.gaussian_filter` with a standard deviation of two. This reduces the strength of any leftover hot pixels. Secondly, the program applies `photutils.detection.find_peaks` to identify stars. In case the second step identifies still-persistent hot pixels instead of stars, a normalized inertia sifter, with a 10-pixel radius, checks to see if the surrounding area around the peak is also relatively bright, and if not, removes the data point from the list. Additionally, we check by visual inspection that all stars were correctly identified. The 10th frame yields significantly fewer stars then the rest, so is left out to ensure proper convergence for the overall fit.

Following the star identification, we organize each star by which exposure they are in and

when they are repeat in another exposure. To do this, we not only run the star finding code on each individual exposure to find around 300 data points in total, but also the "Master Mosaic," shown in Figure 2.8, which come up with around 100 unique stars. The mosaic is constructed by arranging the exposures in the approximate positions relative to each other in the global reference frame, and averaging the exposure values of the portions that overlap. The averaging retrieves a similar background brightness throughout, which allows us to run the star-finding script again, and this time determining the approximate positions of the stars in the global reference frame.

Next, another script compares and matches stars in the global star list and individual frame list that are the same. To do so, the script transforms the star's x and y positions from the detector reference frame into the global reference frame, via approximate position used to place the exposure in the Master Mosaic. Since the exposure positions are still approximate at this stage, we check with a script that matching stars meet certain criteria. To determine which exposure data points correspond to a unique star, they must be both the closest stars in their individual and the global frame, and at most a radius of 5 pixels from each other. Some stars yield no match (likely meaning they were identified in the individual frame but not the global, or vice versa), but the unique stars that had at least two corresponding data, or in other words appeared in more than one exposure, went onto the next round of analysis. Note in Figure 2.8 how none of the yellow circled global reference frame stars are near the edges of the mosaic, because that would mean they had only one corresponding exposure data point. Similarly to how two values are needed to make a meaningful average, two data points to a single real star are needed to determine distortion.

These global reference frame positions are approximate at this stage because we have not yet run any optimization or corrected for any distortion yet, but they are sufficient to cross-reference with the data in the individual frames, and later use as an initial guess for the optimization because they are unique on-sky stars. The ∼300 data points for the individual

frames are by contrast 'exact' in the sense that they are the data of the distortion in the reference frame of the detector. If this were a linear optimization problem, the individual exposure data would be the scatter of the scatter plot, and the unique global star positions would be the line we are trying to best-fit.

2.3.3.2 Distortion-less Solution

The fitting function uses each approximate unique star position and exposure placements in the global reference frame as the initial guess for the unique star's parameters and exposure position parameters. Using `scipy.optimize.leastsq`, the fitter optimized the placement of these global parameters in comparison to the data in the individual frames. One star was left out of the parameters, which could be thought of as the 'anchor,' to avoid degeneracy in the shifting of the entire global reference frame (red circle in Figure 2.8). The anchor star was positioned at the center to minimize parameter correlations, although moving the origin does not actually change the best fit. The optimized model at this point of the process could be considered as the "distortion-less" solution, because the solution represents the averaged locations of the Palomar 2 stars taken from images.

2.3.3.3 Applying Distortion

After determining the best average global star and exposure positions, the model applies a polynomial transformation from the distorted star positions in their individual exposures. The best-fit polynomial transformation is the distortion solution. We used 1st-, 2nd-, 3rd- , and then 4th-order polynomials for accumulating a better guess and finding the most exact solution. A new polynomial parameter is only kept if the solution retains a lower reduced chi squared while determining the best fit of the distortion across the detector. Note equations 2.1 and 2.2 show the 4th order polynomial transformations.

$$X_{\text{global}}(x, y) = \cancel{x_0} + X_0 + \cancel{a_1 x} + \cancel{a_2 y} + a_3 xy + a_4 x^2 + a_5 y^2 + a_6 x^2 y + a_7 xy^2 + a_8 x^3 + a_9 y^3$$

$$(2.1)$$

$$Y_{\text{global}}(x, y) = \cancel{b_0} + Y_0 + \cancel{b_1 x} + \cancel{b_2 y} + b_3 xy + b_4 x^2 + b_5 y^2 + b_6 x^2 y + b_7 xy^2 + b_8 x^3 + b_9 y^3 \quad (2.2)$$

a and b are new parameters the fitter must also optimize, and x and y are the star positions from the individual frames. a_0 and b_0 are removed to avoid degeneracy with the star position parameters. Also, we define the origin of the distortion at the center according to Equation 2.3 because the detector is a square 256×256 pixel array.

$$X_0 = Y_0 = 256/2 = 128 \quad (2.3)$$

We suspected degeneracy with the linear terms as well and confirmed it through principle component analysis of the fit covariance. After a_1, a_2, b_1 and b_2 are then removed as free parameters to avoid anamorphic distortion degeneracy with the scaling of both frames and stars. Since the star positions are kept as parameters during the polynomial fitting, the linear polynomials are redundant through the possibility of image magnification.

The final analysis is completed with 63-star parameters in the global reference frame, and 200 data points across 9 exposures, as shown in Figure 2.9. To ensure that we find the solution with the lowest χ^2, we test the convergence with different combinations of parameters. The best solution does not use every polynomial parameter. The final polynomial solution, transitioning from the distorted frame to the undistorted frame, is described in Tables 2.4 and 2.5.

Table 2.3: SCAM Polynomial Distortion Coefficients.

$(X)_{\text{global}}$	1	x	x^2	x^3
1	X_0	a_1	a_4	a_8
y	a_2	a_3	a_6	0
y^2	a_5	a_7	0	0
y^3	a_9	0	0	0

Table 2.4: SCAM Polynomial Distortion Coefficients.

X_{global}	1	x	x^2	x^3
1	128	1	0	1.6e-7 $\pm$ 4e-7
y	0	0	5.5e-7 $\pm$ 3e-7	0
y^2	6e-5 $\pm$ 2e-5	0	0	0
y^3	5.9e-7 $\pm$ 2e-7	0	0	0

Table 2.5: SCAM Polynomial Distortion Coefficients.

Y_{global}	1	x	x^2	x^3
1	128	0	-1.5e-5 $\pm$ 2e-5	1.5e-7$\pm$ 4e-7
y	1	9.3e-6 $\pm$ 2e-5	-6.7e-7 $\pm$ 3e-7	0
y^2	-5.8e-5 $\pm$ 2e-5	-8.4e-7 $\pm$ 3e-7	0	0
y^3	0	0	0	0

Figure 2.9 shows the exaggerated final solution and with corresponding uncertainty. The small red points represent the Gaussian uncertainty distribution for each transformation vector on the figure. The red dots are calculated by using polynomial coefficient covariance after being converted into detector position with 100 random 2-D Gaussian samples. Uncertainty increases at the edges due to both increased distortion and scarcity of data.

2.3.3.4   Ensuring Fit Confidence

Upon inspecting the correlation matrices of all optimized parameters to search for other possible degeneracies, it seems at first that the correlations between star and frame parameters were relatively high. Through further inspection and tests, the correlations were highly dependent on the origin star, and how many frames the origin star appeared in the real data. We chose an origin star which overlapped with the maximum number of overlapping frames, but it could not be all due to the large spread of data across the detector. Regardless, the

choice of origin star had no effect on the converged solution in any tests of real or synthetic data.

To ensure confidence in the fitter, we tested for recovery of synthetic data, both with and without synthetic uncertainty. The first tests contained no synthetic uncertainty, and confirmed basic success in fitter's ability to find the solution, even with an in-exact guess. The next synthetic data tests included uncertainty using `Numpy.Random.RandNumber` generator. The error bars of the optimized solution to synthetic data were within at least two third of the correct solution. This gives us confidence that with Gaussian uncertainty, our model and fitter can find a meaningful distortion solution.

2.4 Light Leak

Characterization of the NIRSPEC SPEC detector revealed an elevated instrument background of $0.7 \pm 0.10 \ e^-/s$ on a 20 minute dark exposure. The excess light is spread across most of the detector, but the highest signal is concentrated in a small pattern on the lower right side of the detector. The pattern resembles a parallelogram with sharp edges rather than a diffuse pattern (Fig. 2.10a). The signal is speculated to be due to a thermal light leak somewhere in the instrument. Initial cross-disperser tests have show no change in the light leak pattern after changing cross-disperser angles. Therefore, the source of the thermal light leak is most likely located inside of the TMA-enclosure.

2.4.1 Lens diagram & setup

Using KECK-NIRSPEC lens diagrams in `Zemax OpticStudio`, we attempt to pinpoint potential regions where the leak may exist. To do so, we examine the propagation of light rays through the instrument in `OpticStudio`. The optical set up is as follows: First, all optics in the light path before the K-mirrors were removed from the layout, then the layout is converted into non-sequential mode. In non-sequential mode, sources can be placed any-

where in the layout and can be used to emit light rays in any direction as opposed to only forward. Second, the three-mirror anastigmat (TMA) enclosure was added to the diagram as an opaque box with the dimensions of the real enclosure, but does not contain the precise shape of the real enclosure. Lastly, the baffle was added to the diagram which greatly limits the angles at which light can enter the detector. It should be noted that the lens diagrams are based on the design of the instrument and may not necessarily correspond exactly with the instrument as built. Any modifications in the instrument during construction, such as a shift in the position of the detector head, is not reflected in the diagrams. The optical layout is illustrated in Figure 2.11.

2.4.2 Backwards Propagation

To propagate the light backwards through the system, the detector is converted into a light source. The rays are traced in reverse to reveal the regions of the enclosure where a light source could illuminate the detector. This experiment also shows the correlation between detector location and light source location in the TMA enclosure. The size and shape of the detector light source was later modified to match only that of the light leak pattern seen on the long exposure dark frames. Instead of one light source the size of the detector, we created an array of smaller detectors filling the shape of the light leak pattern (Fig. 2.10b). Each small light source (denoted by a box) emits light radially, but rays that are stopped by the inside of the baffle are omitted. This is because any ray that hits the baffle is a ray that could not have reached the detector.

As a ray hits a mirror, it is reflected as it would in the real instrument. Any ray of light that misses a mirror may originate from outside of the regular optical path. Rays that land on the TMA enclosure may reveal a potential location for a light leak. For example, when examining the region around M3, some of the rays reflect off the mirror, while others miss. This implies that light originating from behind or the side of the mirror is able to reach the detector in the location of the light leak pattern. The areas of interest that arise from this

experiment are above M3 (TMA Mirror 3), to the left of M2 (TMA mirror 2), to the right of M1 (TMA mirror 1), and on three sides of the cross disperser. The optical diagram with the highlighted areas of interest are shown in Figure 2.12. While this does not guarantee that the light leak is caused by thermal radiation originating behind a mirror, it motivates further examination.

2.4.3   Regions of Interest

We closely examine each region of interest to determine if the source of the light leak can be attributed to its location. For the region behind M1, the light may come from a seam in the enclosure. All of the light rays that miss the M1 mirror stem from the right side of the detector (+X). Light that is cut off by M1 may produce some sharp edges that resemble the top of the pattern, but effect still does not reproduce the bottom edge cutoff. Regardless, there is enough evidence to motivate the covering up of any seams that may exist near M1.

Images formed on the detector have are highly correlated with the M2 mirror. An image formed on M2 closely resembles a horizontally and vertically flipped version of the image formed on the detector. Thus, most light that misses M2 also misses the detector. The only light that can hit the detector from behind M2 is at the very edge of the mirror. In this case, the light only hits the extreme right edge of the detector. Because it is not possible to have the source of the thermal emission exist on the mirror, there does not seem to be a way to produce the light leak pattern seen in the more interior regions of the detector.

Light from the region behind M3 does not interact with any optics, thus the light from this region needs to reproduce the pattern directly, While this is very unlikely, some of the light coming from behind M3 can be cut off by the mirror and also by the baffle. These areas can potentially create sharp edges on the detector.

Additionally, we consider a potential light leak emanating from near the detector. However, due to the shape, position, and angle of M3, there does not seem to be a way for light to

emanate from near the detector, bounce off M3, and reflect back into the detector. Instead, all rays that emanate from the detector and hit M3 will also propagate towards M2. This suggests that it is highly unlikely that the thermal source is coming from the detector head directly.

2.5   Summary

We presented on the characterization of the two NIRSPEC detectors in SPEC and SCAM. We begin with a report of the gain on the SPEC detector. Darks from the SPEC detector show an elevated instrument background of $0.7 \pm 0.10\ e^-/s$ caused by a light leak in the backend camera. The elevated background levels on SPEC appear to contribute to increases in read noise at long exposure times. We report the flux zero points and throughputs in four NIRSPEC filters: N1, N3, N5, and N7. The persistence on the SPEC detector is undetectable down to the noise. We measure a pixel scale of $0.098 \pm 0.004''/px$ in high-resolution mode and $0.1309 \pm 0.0750''/px$ in low-resolution mode. The spectral dispersion across 50 orders follows a $1/m$ relation predicted from the grating equation. The resolution map of the SPEC detector verifies previous models predicting a decrease in performance in the corners of the detector and guides observers to the high-resolution region of the detector.

For SCAM we reported the magnitude zero points for the four NIRSPEC filters and for the first three filters with their short bandpass filters. The SCAM detector pixel scale is measured to be $0.157 \pm 0.001''/px$. Lastly, we presented on the geometric distortion of the SCAM detector and provide a distortion solution which can be used to correct for optical aberrations.

More data is currently being taken to identify more spectral lines out to longer wavelengths. These measurements will allows us to determine the spectral dispersion of the SPEC detector out to longer wavelengths and calculate the flux zero points for additional filters: KL, K-prime, L-prime, M-prime, M-wide, and possibly narrow-band filters H2, HeI, and FeII. For

SCAM we are currently designing tests to determine the conversion gain, and in turn, the dark current, read noise, and persistence. We also plan to extend the table of magnitude zero points to include the bands mentioned before as well as the throughput in each filter.

Lastly, we examined potential locations for a thermal light leak in NIRSPEC. The TMA enclosure plates may have small areas that light can seep through and there is enough evidence to motivate the covering up of any seams that may exist near M1. Due to the strong correlation between M2 and the detector, there does not seem to be a way to produce the light leak pattern from the region around M2 alone. Light that is cutoff by the baffle can produce a sharp edge that could resemble light patterns that we see on instrument cool down. And finally, it is highly unlikely that the thermal source is coming from the detector head directly. Covering these regions of interest may help in reducing the elevated dark signal seen in long exposures. Reducing the effects of this light leak will decrease the instrument background and improve the performance of SPEC at long exposure times.
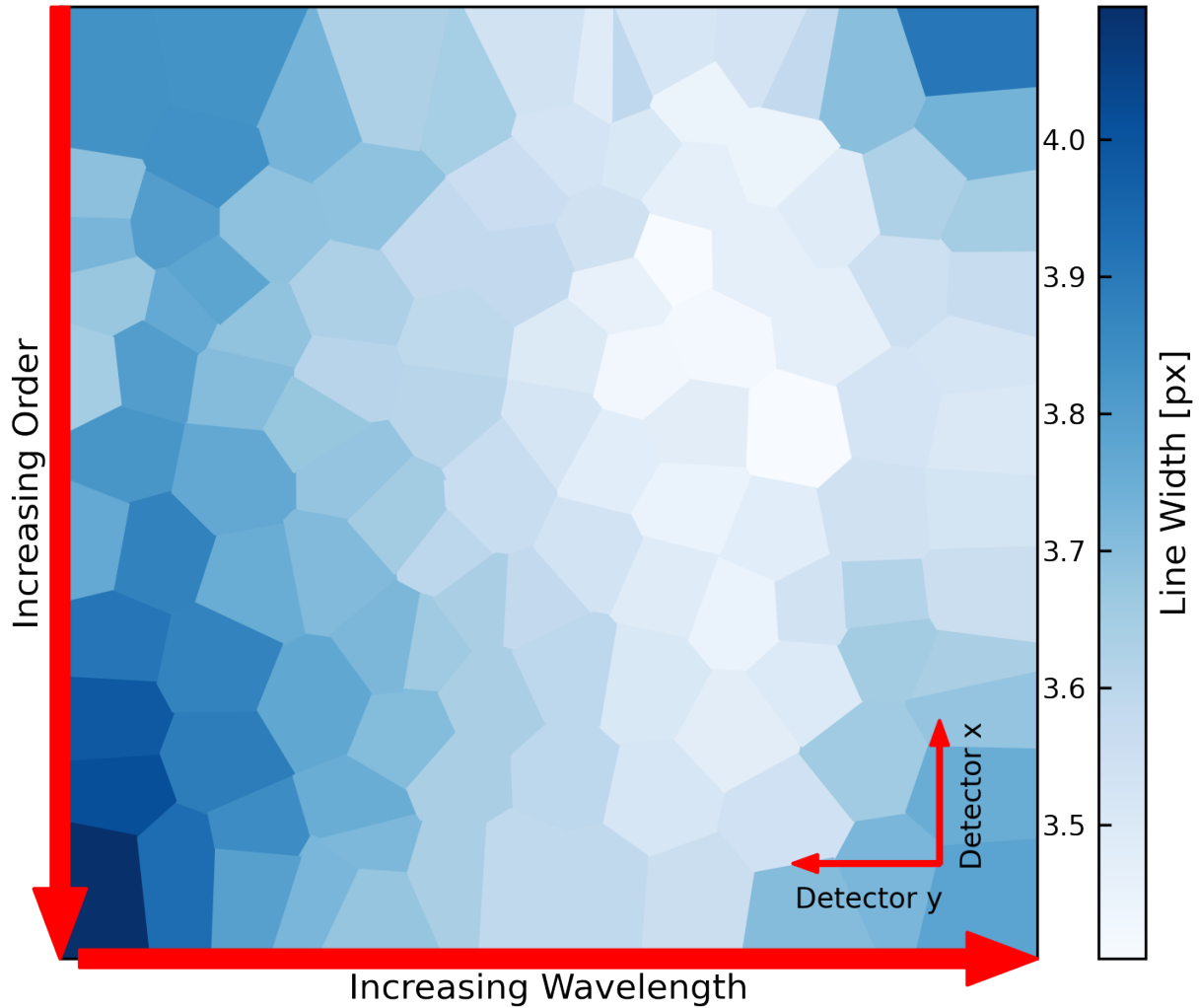
Figure 2.7: Voronoi diagram mapping the relative resolution of spectral lines. The resolution ranges from 3.4 to 4.1 pixels using the $0.288'' \times 12''$ slit in the N5 band. Lighter colors denote thinner lines and thus higher resolution. The resolution element of each individual region is determined using the mean resolution of lines enclosed by that region. The corners of the frame have the lowest resolution while the center of the "plus" pattern has the highest resolution.
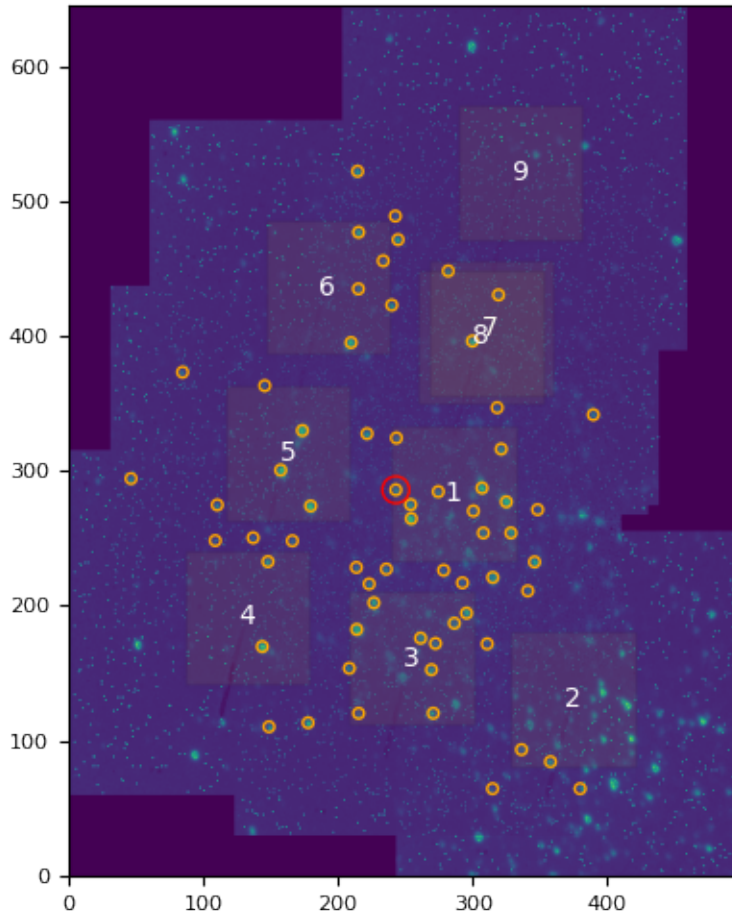
Figure 2.8: The Master Mosaic is the estimated initial guess for 63 on-sky stars in the globular cluster Palomar 2 and 9 frame relationships. The red circle identifies the "origin" star, which has a fixed position to avoid Mosaic shifting. Each of the 63 stars has 2 or more corresponding data points for which `scipy.optimize.leastsq` uses to optimize the Master Mosaic. The light-yellow squares are centered at each individual frame, and about one-eighth the size so each frame's approximate placement is visually discernible.
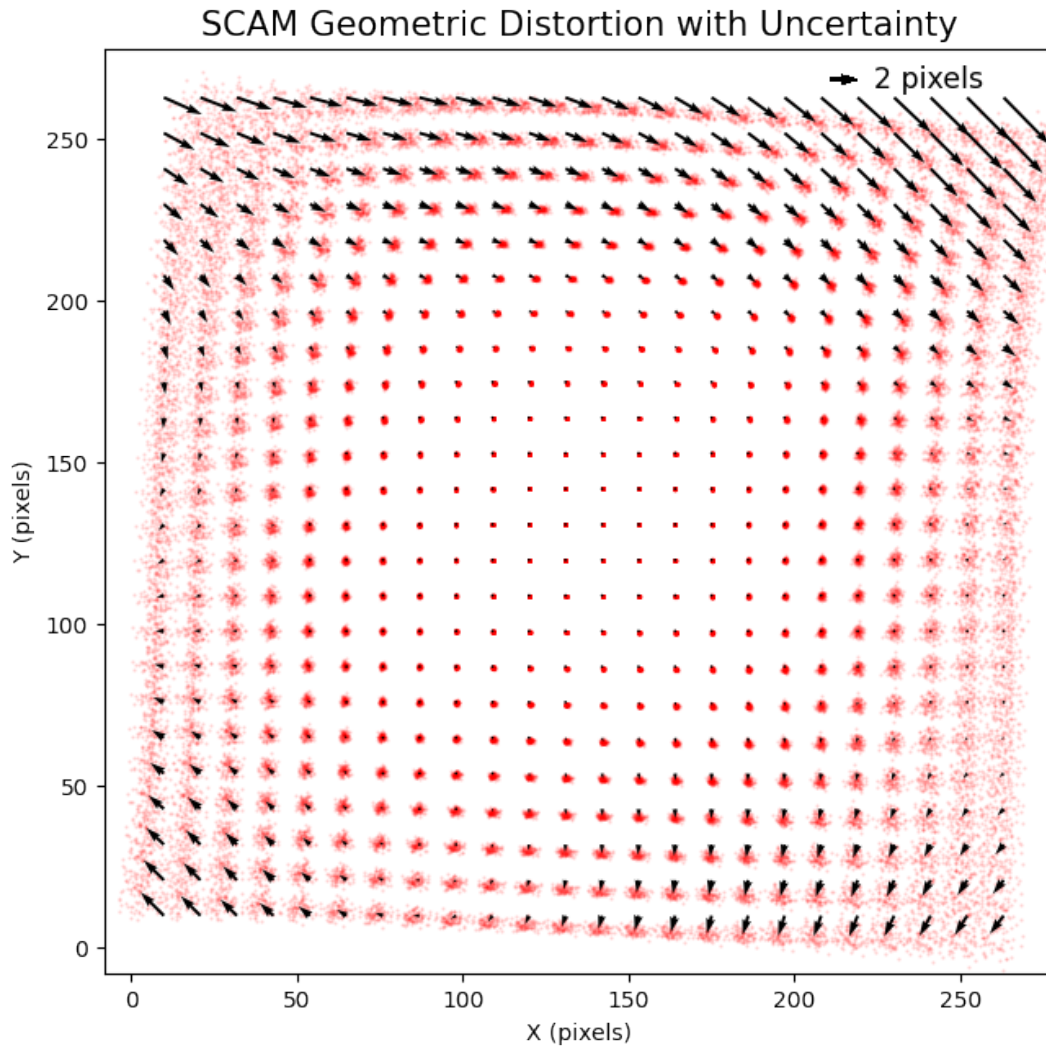
Figure 2.9: The exaggerated geometric distortion vector plot solution across the SCAM detector. The arrows point in the direction of translation, from observed (distorted) positions to real (undistorted) positions. The clouds of red dots represent the positional uncertainty of the undistorted position.
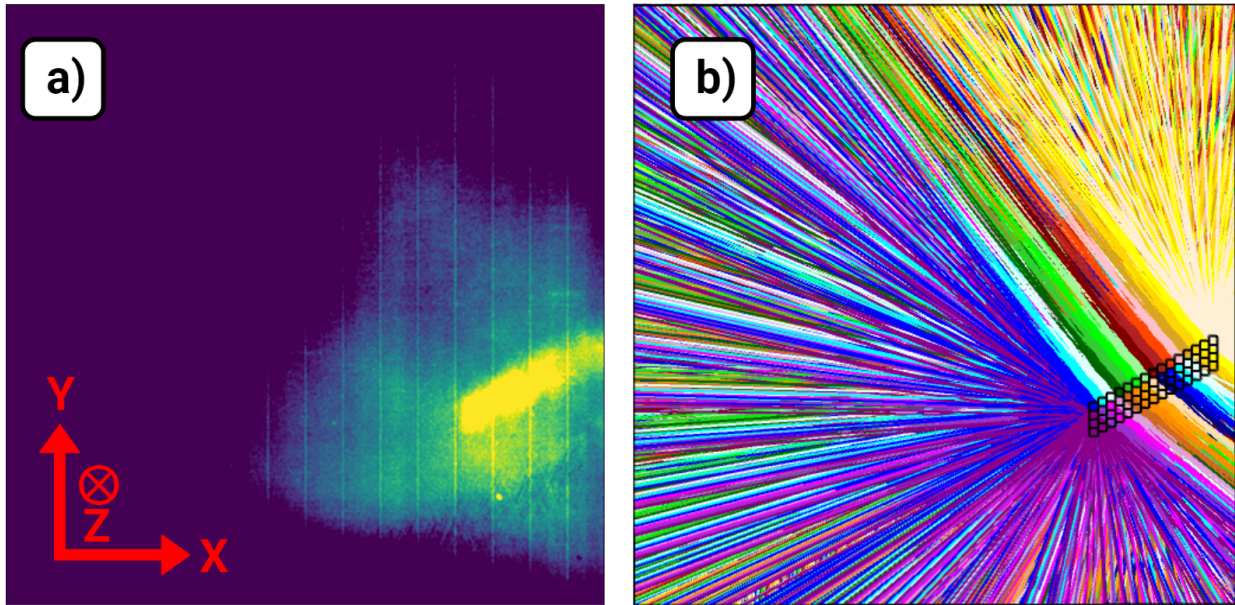
Figure 2.10: a) Sample 20-minute dark frame, same as in Figure 2.3, but with a different color stretch to show the sharp structure in the leak pattern. The orientation is denoted in the bottom left corner, where the Z-axis is "out of the page". b) Backward propagation of light in OpticStudio, designed to match the pattern in 'a'. The small boxes act as light sources, that emit light radially. Any rays of light that would be stopped by the baffle are omitted. The colored rays emanate from the detector and propagate through the instrument. The colors of the rays were chosen only to differentiate each light source and do not have any other intrinsic meaning.
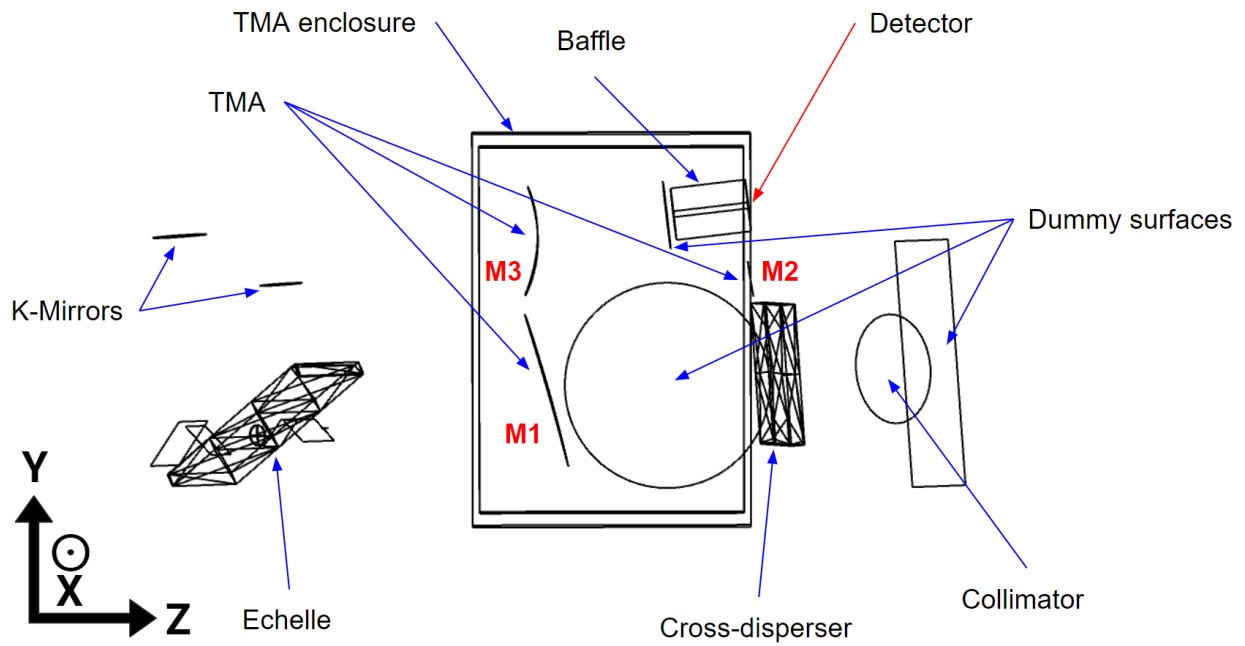
Figure 2.11: The optical layout of NIRSPEC used for ray tracing in `OpticStudio`. The areas of interest is the three-mirror anastigmat (TMA) which contains three mirrors: M1, M2, M3, labeled in order of forward light propagation. The dummy surfaces are used for analysis purposes and do not affect the light in anyway.
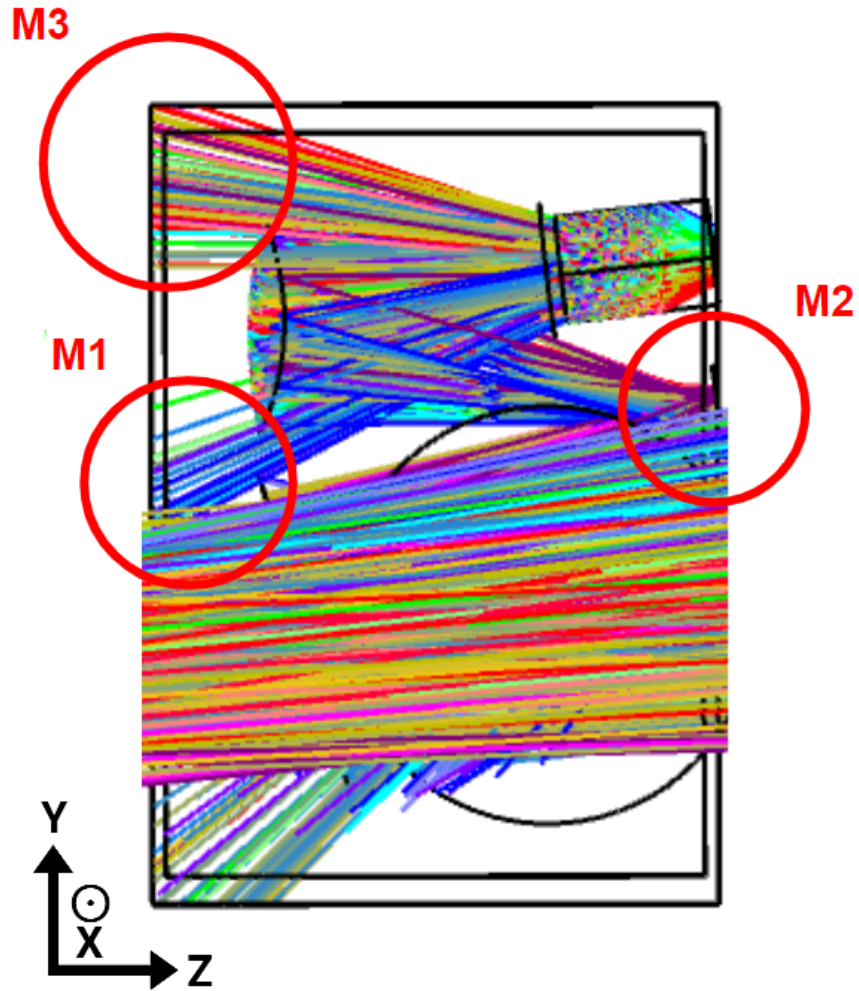
Figure 2.12: The results of the backward propagation of light rays in `OpticStudio`. The optical layout of NIRSPEC is the same as in Figure 2.11, but most of the instrument is removed for clarity. The colored lines represent the light rays emanating from the detector. As a ray hits a mirror, it is reflected in the diagram as would in the real instrument. Any rays that then miss a mirror represent photons that may originate from outside of the regular optical path. The encircled regions represent the locations in which light rays miss the associated TMA mirror. These regions are potential locations for the source of the light leak.

CHAPTER 3

Concept for Calibration of OSIRIS with a Fabry-Pérot Etalon

3.1 Introduction

In this work, we aim to determine the feasibility, requirements, and basic design of a Fabry-Pérot etalon calibrator for the OSIRIS instrument on the Keck I telescope. OSIRIS is an R~3800 near-infrared, lenslet based integral field spectrograph (IFS) designed to take full spectra from 1 - 2.4 μm (Larkin et al., 2003, 2006; Mieda et al., 2014). Due to differences in the optical paths taken by the light, the wavelength solution for each lenslet, differs from each other in the array. These differences underscore that care must be taken to obtain accurate wavelength solutions. Traditionally this can be done through spectral template matching using arc lamps and telluric OH lines, but the lines are not uniform in frequency space nor brightness, making these methods difficult and time consuming.

With a dense grid of spectral lines, the spectral calibration can be enhanced, and in turn, improve OSIRIS's ability to measure the kinematics of astronomical objects. In addition to inconsistencies with the wavelength solution, there are variations between the lenslet PSFs. Each lenslet has its own unique imperfections and slightly different light paths which cause slight differences in the PSF between lenslets. A poor measure of the PSF is especially detrimental in decoupling neighboring spectra and mitigating crosstalk; this is acute because of the close packing of spectra in OSIRIS. With many consistent measures of the PSF, overlapping spectra can more accurately be decoupled which will help disentangle overlap-

ping spectra and mitigate crosstalk. Improvements in crosstalk mitigation allow for higher contrast observations and thus more accurate observations of AGN and exoplanets.

A Fabry-Pérot etalon calibrator can be used to create a dense grid of calibration lines and PSF references to improve the overall spectral calibration of OSIRIS. In Section 3.2 we discuss the basic properties of an ideal etalon. In Sections 3.3 and 3.4 we detail how the free spectral range and finesse are determined for an ideal etalon optimized for OSIRIS. Lastly, in Section 3.5 we introduce a realistic etalon and the consideration and exploration of design limitations, optical imperfections, and other design requirements.

3.2 An Ideal Etalon

A Fabry-Pérot etalon, consists of a pair of reflective surfaces separated by a small cavity that only transmits light in resonance with the cavity (Hernandez, 1988). Light that enters the etalon is reflected repeatedly across the cavity, transmitting some of this light with every reflection. This process produces an interference pattern of maxima and minima, that when paired with a spectrograph, create numerous evenly spaced lines in frequency space. These etalon lines can then be used similarly to arc lamp lines for the purpose of spectral calibration on OSIRIS. By comparison, arc lamps tend to produce fewer lines that are spaced out unevenly across the spectrum.

Basic properties of the calibration produced by an etalon are described by the free spectral range (FSR) and the finesse. The FSR is defined as the spacing between neighboring maxima of transmitted light; a larger FSR correlates to a larger gap between neighboring maxima. The finesse is defined as the ratio between the FSR and the full width at half maximum (FWHM) of an etalon line (Equation 3.2). Higher finesse correlates to sharper lines relative to the spacing between maxima. These quantities determine the density and quality of the calibration lines produced by the etalon and are tuned by setting the physical properties of the etalon. The basic physical properties of an ideal etalon are the cavity width (d), group

refractive index of the cavity (n_g), incident angle (θ) and the reflective coatings. The first three properties: d, n_g, and θ, collectively set the FSR of the etalon (Equation 3.1). On the other hand, the finesse, or "reflectivity finesse" is set only by the reflective coating and is higher for higher reflectivity. The determination of the FSR and finesse set the design requirements for the etalon in the "ideal" regime. In Section 3.5 we explore the ways in which the requirements of a realistic etalon may differ from the ideal scenario.

$$\text{FSR}: \Delta\lambda = \frac{\lambda_0^2}{2n_g l \cos\theta} \tag{3.1}$$

$$\text{finesse}: \mathcal{F} = \frac{\Delta\lambda}{\delta\lambda} \tag{3.2}$$
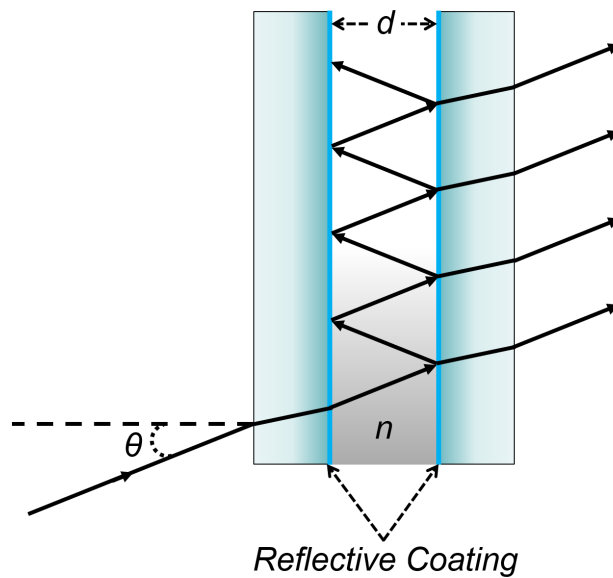
Figure 3.1: Diagram of an ideal flat mirror etalon. Light enters the etalon from the lower left-hand side of the diagram. Where d is the cavity width, n is the group refractive index, and θ is the incident angle.

3.3 Etalon Free Spectral Range

3.3.1 Standard Calibration Line Density

The OSIRIS spectral calibration process traditionally uses a combination of OH lines and arc lamp lines to determine a wavelength solution. This method works well when there is sufficient line coverage across a band. However, for OSIRIS, calibration lines are not uniformly dense and not evenly distributed across each band, leading to significant gaps between neighboring spectral lines, especially in K broadband (Kbb). See Fig. 3.2. We use the median line spacing as a measure of calibration line density and uniformity. This metric measures the spacing between every spectral line and uses the median in each band to characterize the spread. Using this method we find a median line spacing of 6.20 nm, 7.99 nm, 11.43 nm, and 15.94 nm in each band Zbb, Jbb, Hbb and Kbb respectively (Figure 3.2). These values act as the lower limits of line density that an etalon must achieve to be favorable. This lower limit corresponds to an FSR of ∼1000 GHz. The etalon must have an FSR less than this value in order to exceed the the median line density of the OH lines.

3.3.2 Determining the ideal FSR

Ideally, we wish to have as high of a line density as possible. As the FSR is inversely dependent on the distance between the plates, widely spaced plates cause the etalon to have a very small FSR, and thus spectral modes will be very closely spaced together in wavelength. This introduces a limiting factor on the distance between the plates, as it is key to ensure that the data points do not overlap and bleed into each other. To find this maximum distance between the plates that an etalon could have, it is key to inspect how the introduction of a neighboring mode would affect the behavior and shape of the original mode. The criterion chosen to reflect this is the shift in the peak location of some data point depending on how close a neighboring point lay. To explore this, a super-sampled PSF representative of the OSIRIS system is used. The gradient of the PSF is employed, calculated with a standard
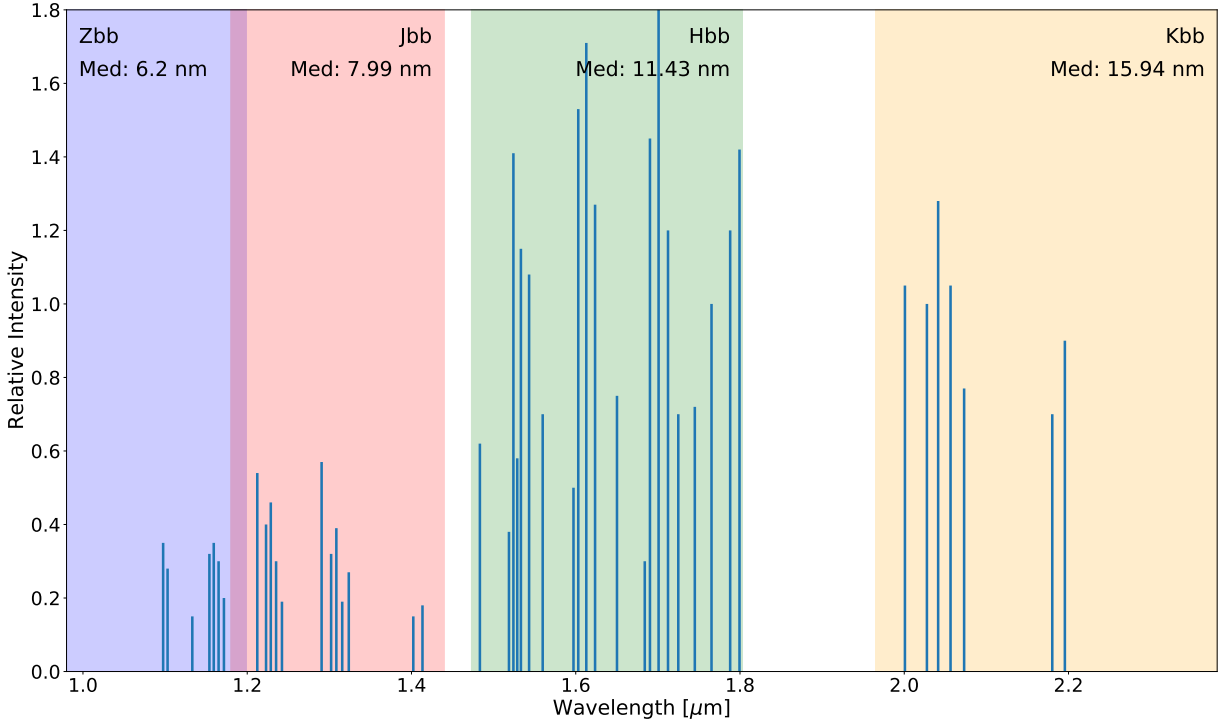
Figure 3.2: Empirical OH line list taken from OSIRIS in the Zbb, Jbb, Hbb, and Kbb broad bands. The wavelengths and relative intensities of these lines are found using the OH line list provided in Rousselot et al. (2000)

second order approximation $f_i(x) = \frac{f(x_{i+1}) - f(x_{i-1})}{2d}$, the d parameter being 0.01 due to the oversampling factor. A spline is used to smoothly approximate the gradient.

To examine how close two neighboring modes can get without affecting the peak's position, two gradients are separated at a certain distance, and the incoming intensity values from the gradient of the neighboring mode are added to those of the first mode's gradient at the overlapping locations. From there, it can be seen whether this introduction has shifted the location of the peak of the original PSF, which is easily measured at the location of the original gradient's inflection point, or where the gradient crosses the x-axis. The relationship between the separation of the two modes and the "shift" that moves the peak location places a limit in the distances between two neighboring modes.
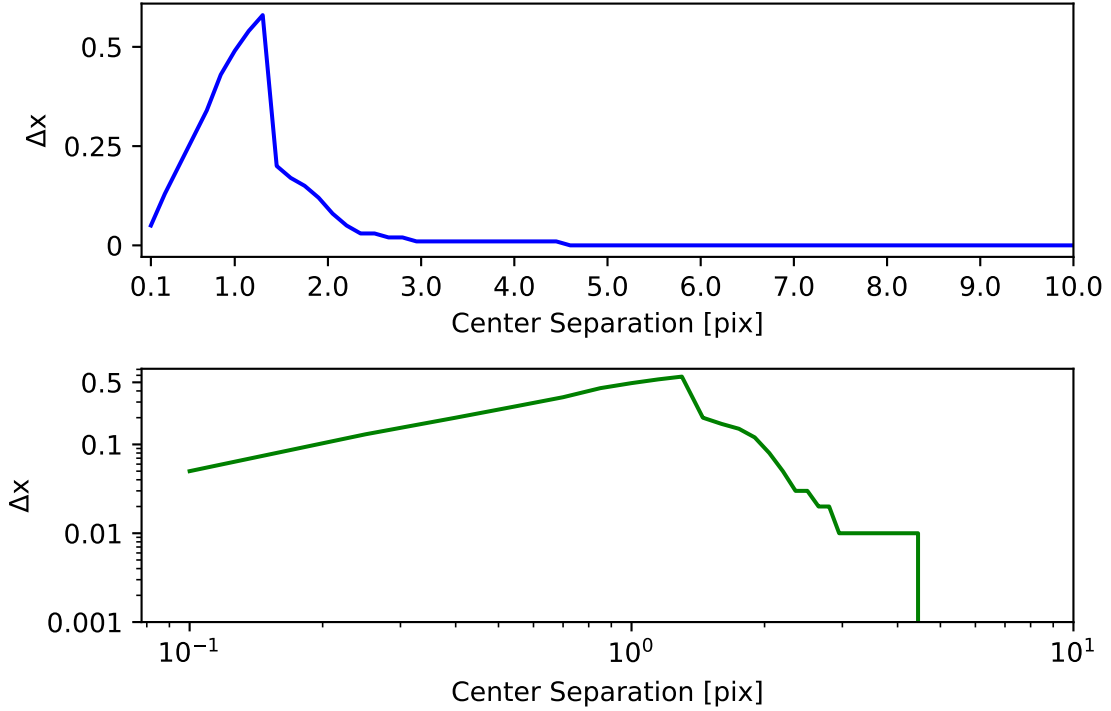
Figure 3.3: Relationship between the change in peak position (Δx) and the separation between neighboring data peaks, each measured in pixels. The bottom plot shows a log description of the relationship.

Figure 3.3 shows that a separation between PSFs of at least 5 pixels would produce a negligible shift in the peak position of the PSF. This is clearly seen in the log description of the relationship, as the peak shift drops off significantly before 5 pixels, which corresponds to a separation of 220 GHz. Translating this pixel width into an etalon cavity width gives a maximum separation of 0.68 mm (See Eq. 3.1, assuming $n_g = 1.0$, and $\theta = 0$).

3.3.2.1 Etalon line density at the upper limit

The upper line density limit is set at 220 GHz, and while the FSR is constant in frequency space, it increases with wavelength in wavelength space. As a result, the minimum spacing of 5 pixels is set at the high frequency end of Zbb. The same FSR results in a larger 14.76 pixel separation at the low frequency end of Kbb. Even with this line spacing increase, an
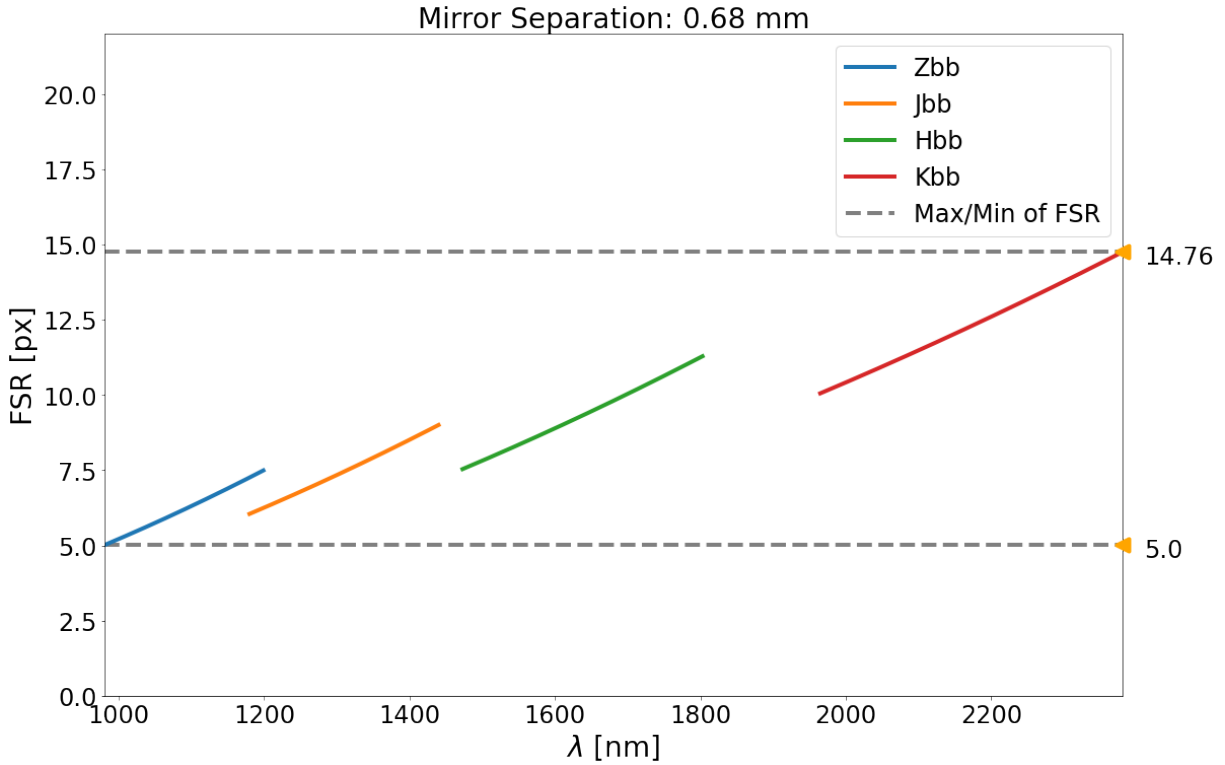
Figure 3.4: The free spectral range (FSR) in wavelength space in units of pixels (FSR = 220 GHz) for an etalon of mirror separation $d = 0.68\ mm$, group refractive index $n_g = 1.0$, and incident angle $\theta = 0$. The separation between neighboring maxima is closest in Zbb setting the minimum spacing at 5 pix. The end of Kbb has the largest spacing at ~15 pix, yet is still dense enough to provide a much denser grid of lines than typical calibration sources.

etalon would perform significantly better than traditional calibration lines. The median line spacing for an etalon with an FSR of 220 GHz is described in Table 3.1. We see a dramatic improvement in line density compared to OH lines, and the inherent uniformity produced by the etalon creates excellent coverage over each band. As such, the median spacing at the high density limit is much smaller than that of the OH lines.

This significant improvement, relative to the telluric OH line density, means that the FSR requirement can be relaxed if needed; between 220 GHz and 1000 GHz. In addition, the group refractive index (n_g) and cavity spacing (d) are degenerate when determining the FSR

(Note: we assume the angle of incidence θ is 0), making these properties relaxable as well. In general, for any specific value of FSR, d decreases as n_g increases for different materials. In Figure 3.5, we plot the degeneracy curve for 5 FSR values and note a sample of a few different materials. For simplicity, the final specifications that we use are at the upper limit of FSR = 220 GHz, which, for a vacuum etalon, corresponds to $n_g = 1.0$ and d = 0.68 mm, but can be altered depending on build requirements.
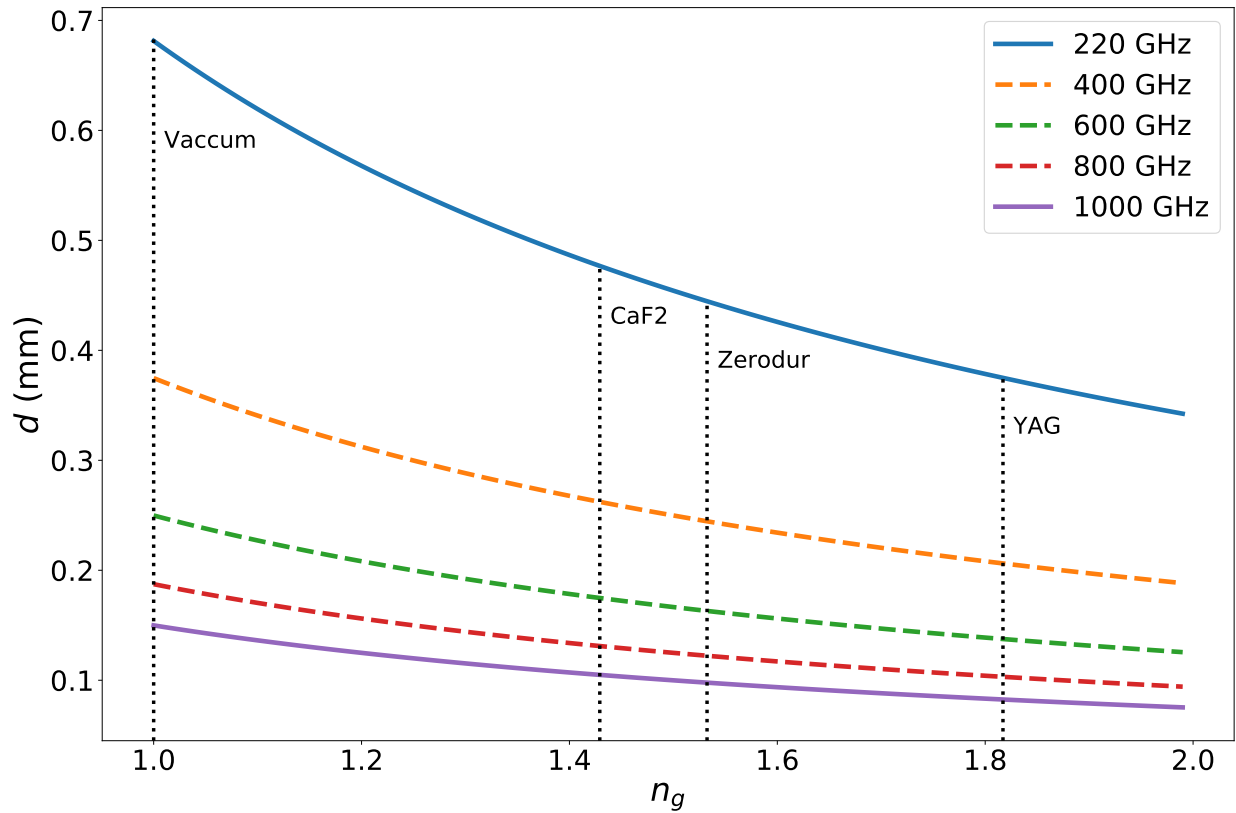
Figure 3.5: FSR degeneracy plot between the group refractive index (n_g) and cavity spacing (d) for 5 values of FSR. The upper and lower FSR limits are denoted by solid lines. The dotted vertical lines denote 4 cavity materials with different group refractive indexes: Vacuum, CaF2, Zerodur, and YAG.

Table 3.1: Median line spacing comparison between OH lines and etalon lines

Band	OH Lines (nm)	Etalon (nm)
Zbb	6.20	0.86
Jbb	7.99	1.24
Hbb	11.43	1.93
Kbb	15.94	3.4

3.4 Finesse

The finesse requirement is more challenging to determine than the FSR and is still in the process of being refined. We estimate the required finesse by first determining how OSIRIS lenslets spread light onto the detector. More accurately, we want to get an idea of how well the OSIRIS PSF can be measured using an etalon of a given finesse. Low finesse produces higher deviation from the ideal PSF shape. Thus, the finesse needs to be high enough such that the PSF can be determined to an acceptable accuracy. To simulate this effect, we convolve an etalon line with a super-sampled OSIRIS PSF to get an order of magnitude estimate of the line spreading. Ideally, delta function-like etalon lines would provide a perfect measure of the PSF, but real lines are not infinitely thin. Instead, the etalon line shape can be easily approximated using a Lorentzian function (Ismail et al., 2016), and the transmission function of an etalon can be approximated by a large sum of Lorentzians. Because of this equivalency, we use a Lorentzian function to represent the etalon lines for the rest of our calculations. The finesse can then be mapped onto the width of the Lorentzian using $\gamma(\mathcal{F}) = \delta\lambda = \frac{\Delta\lambda}{\mathcal{F}}$, where $\mathcal{F}$ is the finesse and $\Delta\lambda$ is the FSR calculated using Equation 3.1.

To simulate how OSIRIS widens an etalon line, the Lorentzian is convolved with the OSIRIS PSF. The true PSF is a two dimensional Kbb super-sampled PSF, composed of a spatial and spectral dimension (Figure 3.6a). We collapse the spatial dimension to reduce the dimensionality and simplify the calculation. We use the Kbb PSF centered at $\sim 2.2~\mu$m
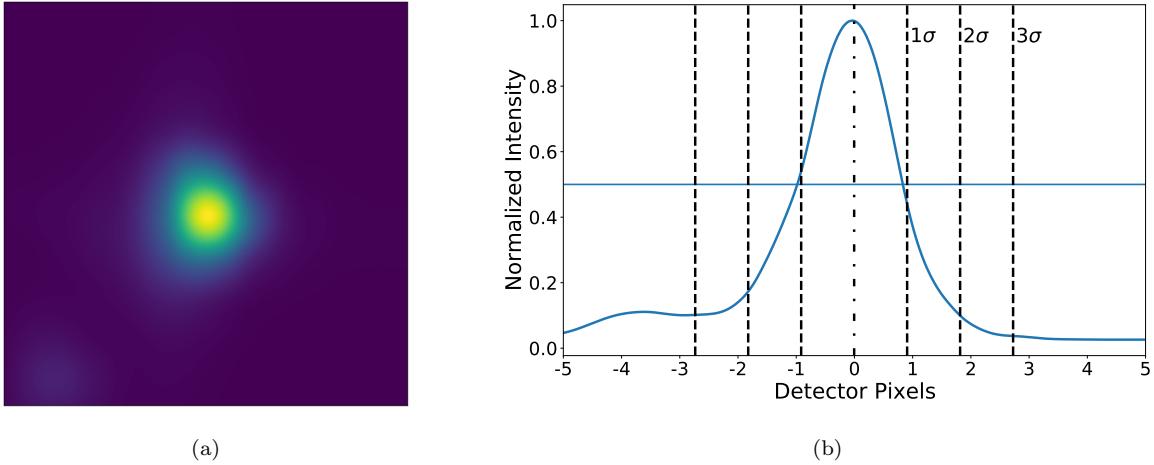
Figure 3.6: (a) Kbb super-sampled OSIRIS PSF (b) Collapsed version of the PSF on the left with vertical lines representing multiples of the HWHM (σ)

because it is currently the only super-sampled PSF readily available, and thus may not reflect the true shape of the PSF for every band. Regardless, this process is sufficient for an order of magnitude estimate of the line spreading.

The etalon line is much narrower than the PSF, so the resulting convolution very closely resembles the original PSF. The residuals between the convolution and original PSF are then scaled by the original PSF to determine the fractional change of the convolution. The residuals are not constant across the full PSF; the center tends to underestimate the PSF while the wings tend to overestimate it. As a result, the tolerance for how well the PSF can be recovered depends on the part of the distribution that is of interest. To differentiate between these areas of interest, we show the collapsed OSIRIS PSF with multiples of the HWHM labeled as σ in Figure 3.6b. The convolution is repeated for multiple values of finesse to measure the changes in the residuals with increasingly thinner etalon lines (Figure 3.7).

In essence, Figure 3.7 illustrates the ability of retrieving information about the original PSF by using an etalon as a PSF reference. It also functions as a map of the regions where the PSF tends to be overestimated and underestimated. The required etalon finesse for OSIRIS is

45

then set by the required PSF retrieval tolerance, which may vary depending on the scientific application. Here we choose a relatively moderate tolerance of 5% out to 2σ, which requires a finesse of at least $\sim$100 or a reflectivity of $\sim$97%. Getting to a tolerance of 3% across the entire PSF for example, requires a very high finesse of 300. This tolerance, however, is not final and will be tuned further as we determine how the etalon will be used and as our requirements become more defined.
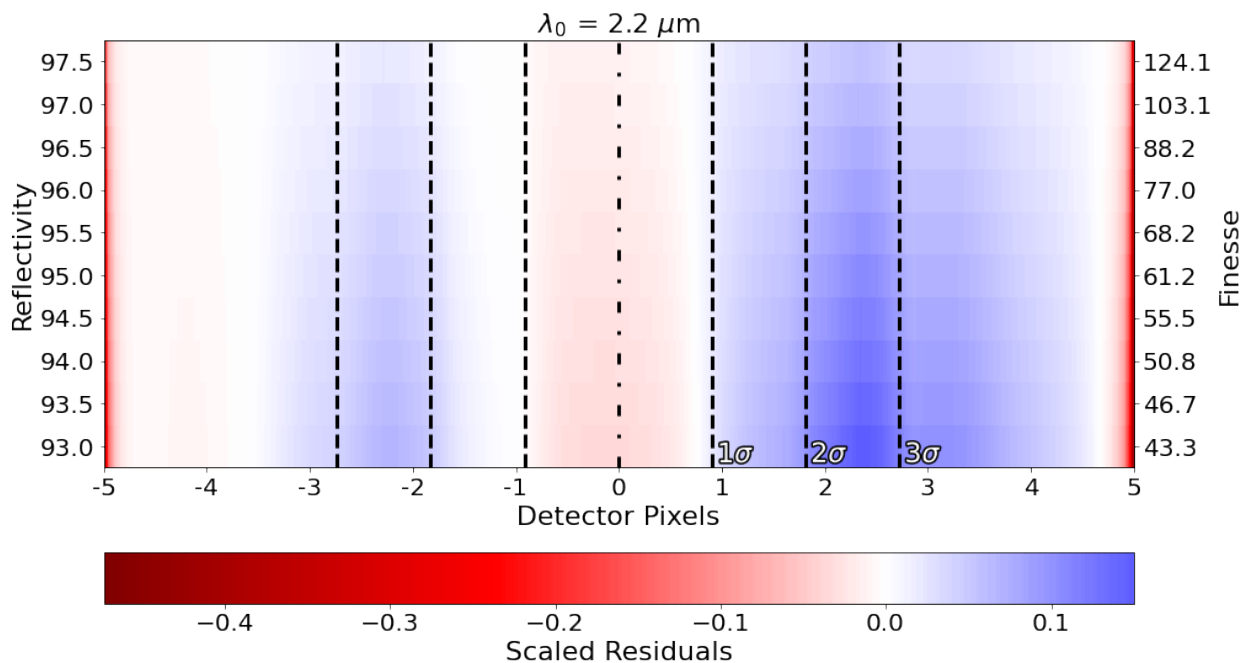
Figure 3.7: Fractional difference between OSIRIS PSF and convolved PSF as a function of finesse/reflectivity. Red corresponds to a negative residual (lower than OSIRIS PSF) and blue corresponds to a positive residual (higher than OSIRIS PSF). The vertical lines are the same as in Figure 3.6b, representing multiples of the HWHM (σ).

3.5 Realistic Etalon

In previous sections of this paper we explain the processes taken to determine the basic requirements for the use of an etalon on OSIRIS. The final specifications of which are outlined in Table 3.2. We will now touch on the aspects of a real etalon that muddle the "ideal"

scenario and discuss how they affect the architecture, the FSR, and the finesse of the etalon.

3.5.1 Etalon Architecture

The first aspect of a realistic etalon that we will address is the etalon architecture. The simplest etalon is a flat-flat etalon consisting of two reflective surfaces separated by a cavity. This cavity can be air spaced, vacuum spaced or filled by some clear material. Each case has its own advantages and disadvantages that we plan to explore. In addition to flat-flat etalons, there are curved etalons capable of higher finesses than their flat counterparts (Hercher, 1968), yet they tend to be more expensive. Etalons can also be manufactured within fibers (Rao et al., 2007, 2008), which may be desirable for OSIRIS. Each architecture will be compared for their finesse capabilities, feasibility, and price point.

The reflective coating is another important area of consideration. While it is true that higher reflectivity produces higher finesse, a higher reflectivity reduces the transmitted light through the etalon and therefore lowers the throughput. Using a brighter light source on the other hand may heat the optics to undesired temperatures causing changes in the FSR.

Finally, the overall layout of the etalon within the OSIRIS calibration system is still under consideration, but the proposed layout is illustrated in Figure 3.8. A light source is first connected by a single-mode fiber to a collimating lens. The collimated light then passes through the etalon and is focused back into another fiber which carries the light to the Keck I AO bench, in particular its integrating sphere, and finally to OSIRIS.

3.5.2 Manufacturing Imperfections

The next set of challenges that we plan to explore come from manufacturing imperfections. Small errors in the assembly of the etalon cause changes and inconsistencies that affect the FSR and finesse. The theoretical finesse discussed in Sections 3.2 and 3.4 is more accurately referred to as the "reflectivity finesse," but the "effective finesse" is always lower due to these

Table 3.2: Final specifications for an etalon for OSIRS

Specification	Value
FSR	220 GHz
finesse	100-300
d	0.68 mm
n_g	1.0 (Vacuum)
θ	0
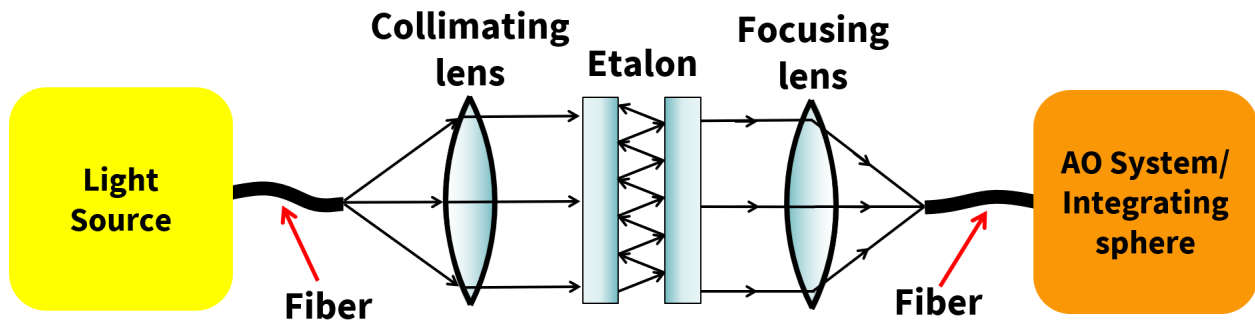
Figure 3.8: Block diagram of proposed etalon layout. The etalon will be installed as part of the Keck I AO bench and telescope simulator

imperfections. Parallelism defects, spherical defects, and surface roughness all contribute to lowering the total finesse of the etalon (Palik et al., 1996). Additionally, etalons can be sensitive to thermal changes, which most notably can expand or contract the cavity, altering the FSR, and thus changing the position of the reference lines. Minimizing the effects of these imperfections comes at a price and is limited by manufacturing capabilities. Through careful examination of these variables, we will adjust the requirements and manufacturing tolerances needed to design an etalon for use on OSIRIS.

3.6 Conclusion

Overall, the concept of designing an etalon calibrator for OSIRIS is feasible. We have demonstrated that an etalon with an FSR of 220 GHz will provide more than enough calibration lines to outperform standard calibration lines. Achieving the goal of an FSR of 220 GHz can be reasonably done without requiring unrealistic cavity sizes, materials, or geometry. Imperfections in the etalon may cause uncertainties in this value, but we plan on exploring these effects in great detail. While the finesse requirement is more challenging to define than the FSR, we have taken steps to constrain this requirement. High finesses of over 100 are difficult, especially with optical imperfections, but with further study of our requirements, this number may change. Various etalon architectures may also be capable of reaching these levels of finesse if needed, but tend to increase the cost as a result. The initial exploration of using an etalon calibrator for OSIRIS has gone well and we plan on continuing this work into the near future.

CHAPTER 4

The Peculiar Warp of HD 110058's Debris Disk

4.1 Introduction

Stars with substantial infrared excesses often harbor a reservoir of dust in their systems. Debris disks are generally known to be optically thin and gas poor, primarily composed of dust. Generally, dust is quickly removed from the system through radiation, stellar winds, and Poynting-Robertson drag. As such, the lifetime of dust is significantly shorter than the age of main sequence stars. This is especially true for micron-sized dust grains or smaller that scatter light in the near-infrared and visible range. In order for a system to retain enough dust of this size to remain detectable in the near-infrared after a few tens of millions of years, there needs to exist a reservoir of parent bodies (planetesimals) that actively replenish the disk (Wyatt et al., 2015). Thus, detections of debris disks around main-sequence stars suggests active dust creation through sublimation or through collisional cascades driven by dynamical stirring of planetesimals (Hughes et al., 2018b).

The thousands of exoplanet discoveries in the past few decades have fundamentally changed the way we think of planet formation. Many planetary systems have shown vastly different architectures to that of our own solar system, and have motivated the deeper exploration of system demographics and dynamics. The interaction between radiation, planetesimals, planets and possible other external forces work to regulate the creation, destruction, and distribution of dust around a star. These dynamical interactions determine the structure

and composition of debris disks and shape them into unique morphologies. Disk features, such as warps, gaps, and asymmetries, are interesting because they provide evidence of significant or large-scale dynamical interactions (Wyatt et al., 1999). Stellar fly-bys, large collisions, ISM interactions, and planets have all been proposed as plausible phenomena for the creation of these large scale disk features (Lee & Chiang, 2016).

Many debris disks have been spatially resolved to date, and several of these disks have shown unique features and warps. In perhaps the most archetypal example, β Pictoris possesses a debris disk with an asymmetric vertical warp (Smith & Terrile, 1984). The shape has been characterized by an inner disk that is inclined relative to a flat outer disk (Kalas & Jewitt, 1995). It was originally hypothesized that this feature could be the result of perturbations caused by an inner planet on an inclined orbit relative to the disk (Mouillet et al., 1997; Heap et al., 2000). Subsequent observations have revealed the existence of the planet β Pictoris b, which matches the planet properties necessary to account for the warp in the disk (Lagrange et al., 2008; Dawson et al., 2011).

Additionally, the HD 61005 debris disk appears to have asymmetries in both its morphology and brightness profile. The disk was originally discovered by Hines et al. (2007) and was observed to have a "swept-back" morphology. This special morphology was originally hypothesized to be due to interactions with the ISM through secular perturbation of grains by low-density interstellar gas (Debes et al., 2009; Maness et al., 2009). However, Buenzli et al. (2010) showed that the star is offset from the center of the disk, suggesting that a planet may be involved in perturbing the structure of the disk. This hypothesis was further explored in Esposito et al. (2016), which presents a model involving a perturbing planet with the properties needed to produce each of the aforementioned asymmetries.

In both cases, direct imaging has revealed information on the dynamical response from the disk by external sources, such as planets. Through scattered-light imaging we can measure properties of the disk that cannot easily be obtained through thermal emission. Observing

dust in scattered light points to the existence of small dust grains in the system. Grains smaller than a characteristic radiation blowout size are known to have very short lifetimes and thus must be newly created if they are to be observable. Micron-sized dust grains can more easily interact with and scatter infrared radiation but this light can be much fainter than light from the star. This contrast difference can be overcome through modern high-contrast imaging techniques and instruments, such as those using adaptive optics and coronagraphs to suppress and control starlight (e.g. GPI, (Macintosh et al., 2014), SCExAO/CHARIS (Jovanovic et al., 2015; Groff et al., 2015), SPHERE (Beuzit et al., 2019)).

Imaging of optically thin, edge-on debris disks are simpler than other disk geometries, but are particularly challenging to analyze due to the degeneracies inherent in the observed brightness of the disk. The brightness profile of the disk is a function of both its density distribution and the dust's scattering properties, which is challenging to untangle due to projection effects. However, these images more easily reveal deviations from flat geometries and provide a framework for probing dynamics through asymmetries. In this paper, we examine the edge-on disk around HD 110058 and explore the factors that lead to the observed warp in its midplane. In Section 4.2, we present the GPI observations analyzed in this work, as well as briefly summarize previous observations of the disk with other instruments. In Section 4.3, we describe the data reduction methods used to retrieve total intensity images of the disk. In Section 4.4, we explore the morphology of the disk and discuss the intricacies of the midplane, scale height, and brightness profile. In Section 4.5, we examine the effects of viewing angle and disk orientation on the observable midplane using simulated radiative transfer models. Lastly, in Section 4.6, we discuss the dynamical processes in which a planet on a misaligned orbit may warp a disk to a shape like that of HD 110058.

4.2 Observations

4.2.1 GPI Observations

Gemini Planet Imager (GPI) is a high-contrast integral field spectrograph optimized for direct imaging of exoplanets, originally built for the Gemini South Telescope (Macintosh et al., 2006). As part of the Gemini Planet Imager Exoplanet Survey (GPIES) starting in 2014, GPI completed a ~ 4 year direct imaging survey of 104 young, nearby stars with large infrared excesses for the purpose of detecting and studying circumstellar disks via scattered-light imaging (Esposito et al., 2020). The survey resolved 26 debris disks in both polarized intensity and total intensity using the H-band ($1.6\mu m$) coronagraphic polarimetry mode on GPI.

HD 110058 is a 17 Myr old A0V type star in the Scorpius–Centaurus OB association located $129.91^{+1.72}_{-0.85}$ pc away (Gaia Collaboration, 2022). The disk was observed in polarimetry mode on January 26, 2016 and March 19, 2016. The first night consisted of eighteen, 60 second exposures, followed up by a longer observation totalling thirty-two, 60 second exposures spanning a total paralactic angle off 25.2° (See Table 4.1). These data were first presented in Esposito et al. (2020), and included polarized intensity images of the disk. In this paper, we take a closer look at the total intensity data to characterize the disk around HD 110058. The structure of the disk is best characterized in total intensity images which contain morphological information not seen in polarized light alone. For an analysis of the HD 110058 debris disk in polarized light, see Crotts & Matthews (2023). Additionally, we only use the data taken from the second night of observations due to the longer total integration time and higher signal-to-noise (SNR). Our primary data were obtained through the GPI exoplanet survey, but we supplement analysis with other observations.

Date	Mode	t_{exp} (s)	t_{int} (s)	ΔPA (°)
01-26-2016	H-band Pol (Snap)	59.65	1073.64	14.1
03-19-2016	H-band Pol (Deep)	59.65	2147.27	25.2

Table 4.1: Table of Observations oh HD 110058. The disk is detected in total intensity on two nights using GPI's polarimetry mode. The first night observed the disk in "snapshot" (Snap) mode using a shorter total integration time, and the second night observed the disk in "deep" mode, using a longer total integration time. Only the second night is used in this analysis. The observation parameters listed are as follows: t_{exp}, exposure time in units of seconds, t_{int}, total integration time in units of seconds, and ΔPA, field rotation in units of degrees.

4.2.2 Other Observations

HD 110058 was first identified as a debris disk candidate by Mannings & Barlow (1998). Using JCMT/SCUBA, Sylvester et al. (2001) the disk went undetected, but observations placed an upper limit on the dust mass of $< 1.7 M_\oplus$. The presence of a disk was finally confirmed by Moór et al. (2006) using the data from the Infrared Space Observatory (ISO) database. HD 110058 was later observed by Wahhaj et al. (2013) and Meshkat et al. (2015), but up to this point, no disk had been resolved and no planetary companion had been identified. The first direct detection of the disk in scattered-light was presented in Kasper et al. (2015) with images of the disk taken in Y-, J-, and H-bands with VLT/SPHERE. The data show a nearly edge-on disk extending out to $0.6''$ (65 au) with bright "knots" at $0.3''$ or 32 au. These observations also provide the first evidence of an asymmetric warp in the disk. New VLT/SPHERE and archival HST/STIS data expand on these findings in Ren et al. (2023) and Stasevic et al. (2023), which we will discuss in more detail in Sections 4.4, 4.5, and 4.6.

The disk around HD 110058 has also been observed twice with ALMA (Lieman-Sifry et al., 2016; Hales et al., 2022), the second of which will be discussed further in Section 4.4. In both cases, they find strong evidence of circumstellar gas in the disk. Optical observations

taken with the Anglo - Australian Telescope and Magellan Telescopes provide additional evidence for the presence of gas in the system (Hales et al., 2017). The star has also been observed with *Spitzer* several times. Initial observations in Chen et al. (2006) do not detect strong spectral features from the disk, giving no estimates on the dust mass, but using follow up observations with *Spitzer* MIPS, (Chen et al., 2012) puts a dust mass estimate of $\sim 0.48 M_{moon}$ at ~ 24.8 au. Further analysis of the infrared excess using *Spitzer* Infrared Spectrograph (IRS) examine the dust grain properties in more detail, proposing a 2-disk model consisting of two populations of grains (Jang-Condell et al., 2015). This includes an inner disk at 0.205 ± 0.02 au consisting of $4.1 \pm 0.12 \mu m$ dust grains with a total dust mass of $2.12e - 07 M_{moon}$, and an outer disk at 15.2 ± 1.2 au consisting of $13.4 \pm 0.2 \mu m$ dust grains with a total dust mass of $2.93e - 02 M_{moon}$.

4.3 Data Reduction

The raw data were reduced using the methods in the GPI `Data Reduction Pipeline` (DRP), as outlined in Maire et al. (2010) and Perrin et al. (2014). The DRP first conducts basic systematic reductions such as dark subtraction, destriping, bad-pixel mapping, and flexure corrections. These data are then run through a series of polarimetry-specific reductions that produce polarization data cubes consisting of two orthogonal polarization states. For simple polarimetry mode reductions, these data cubes are then combined along with parallactic and waveplate angles to construct a Stokes data cube. The Stokes cube is then transformed to the radial Stokes basis and results in a 3D radial Stokes cube containing the I, Q_r, U_r and V stokes parameters. The disk is resolved in polarized intensity Q_r, but we do not include this image in our analysis. For a look into polarized intensity data of HD 110058 see Crotts & Matthews (2023). The Stokes I image contains large contributions from the residual stellar PSF that is not fully blocked by the coronagraph (Fig 4.1), which must be subtracted to reveal the disk signal.
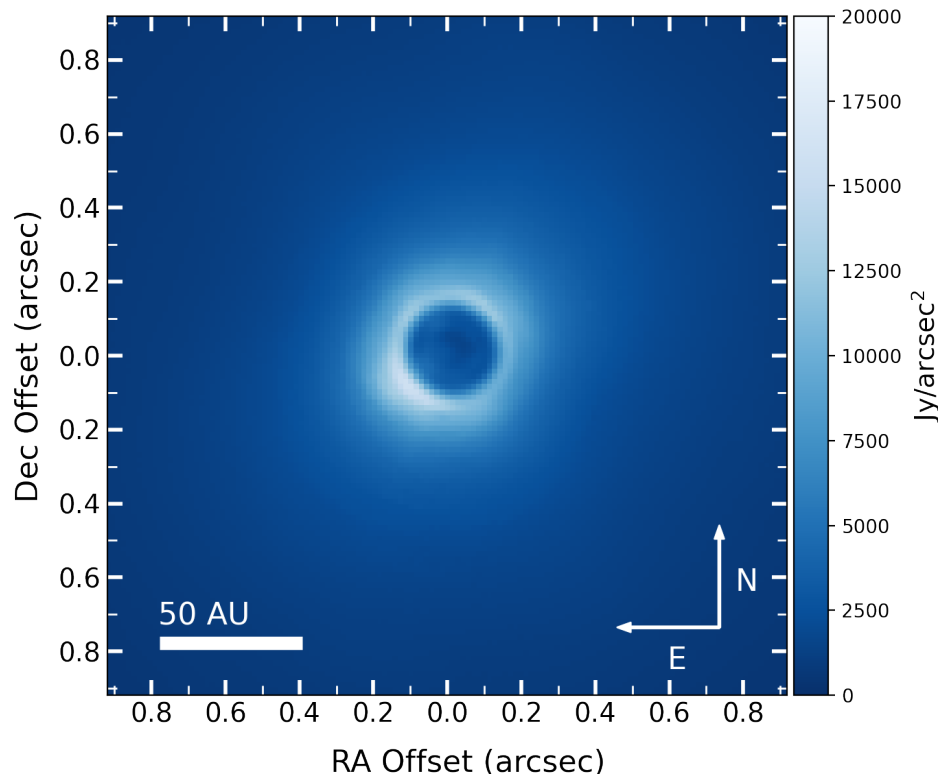
Figure 4.1: Total intensity image of the HD 110058 debris disk in H band before PSF subtraction. The color bar is in Jy/arcsec^2.
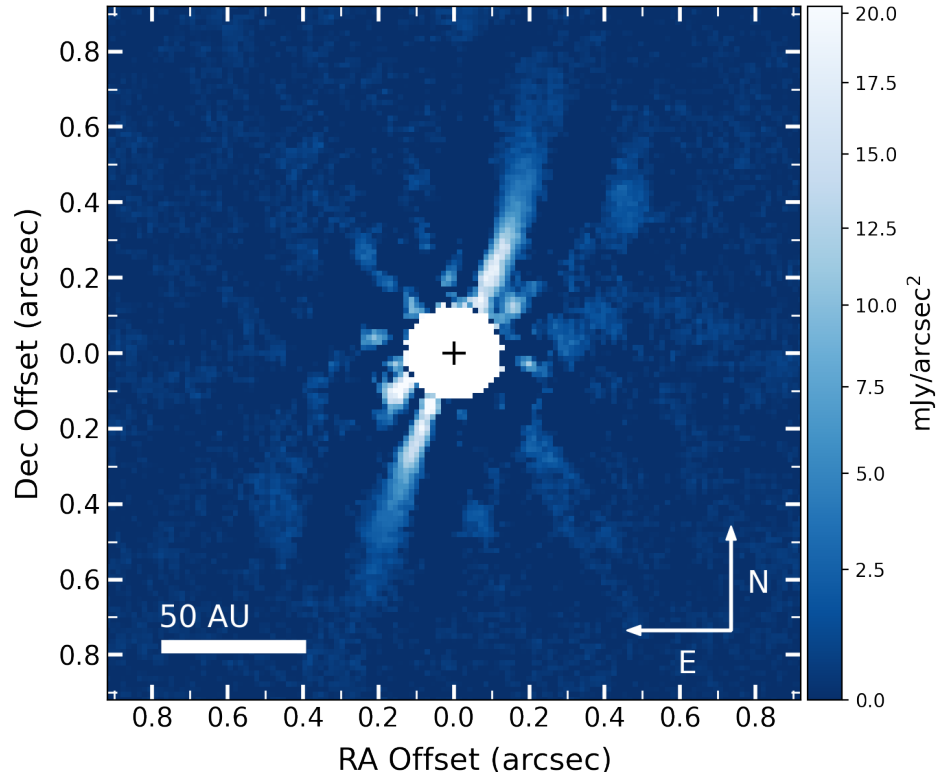
Figure 4.2: (PSF subtracted image of the HD 110058 debris disk in H-band total intensity. The disk is revealed after PSF subtraction using `pyKLIP` + ADI with the following KLIP parameters: `subsections` = 1, `annuli` = 1, `minrot` = 10, and `numbasis` = 2. The disk midplane extends on the southeast and northwest sides of the disk and an asymmetric warp can be seen in its midplane. The star location is indicated the symbol '+' and the data and colorbar are in units of mJys/arcsec^2.

4.3.1 KLIP

To detect the disk in total intensity, we remove the residual stellar point-spread function (PSF). This removal process is done using `pyKLIP`(Wang et al., 2016). `pyKLIP` is a Karhunen-Loève Image Processing (KLIP) package which uses principal component analysis to perform PSF subtraction for high-contrast imaging (Soummer et al., 2012). For GPI data, `pyKLIP` employs angular differential imaging (ADI) (Marois et al., 2006), which takes advantage of the field rotation introduced in images produced by an alt-az telescope such as Gemini. For GPI, the instrument is mounted directly onto the back telescope at the Cassegrain focus, and thus naturally, objects in the sky rotate relative to the optics of the instrument, while instrument artifacts remain stationary. This rotation is used to differentiate between real astrophysical signals and signals produced by instrumental effects. The KLIP algorithm takes in the set of reduced total intensity data and constructs a basis of eigenimages, which is then used to model the starlight and subtract out the PSF of the star. Most of the starlight is removed in the lowest-order modes, revealing the disk in total intensity.

For these low-order modes, the majority of light is residual starlight, but may contain trace amounts of disk signal (Mazoyer et al., 2020). Removal of these modes may result in self-subtraction and a bias of the disk signal. We optimize the KLIP reduction to attain the highest possible signal-to-noise ratio (SNR) while minimizing the self-subtraction of the disk. We choose the optimal combination of the following `pyKLIP` parameters: `subsections`, `annuli`, `minrot`, and `numbasis`. The `subsections` and `annuli` are both set to 1 as they result in a smoother reduction, and the minimum rotation (`minrot`) parameter is set to 10 to minimize self-subtraction in the disk. The `numbasis` parameter is set to 2 in order to retain the disk signal but remove some of the larger residual speckles. Even with a careful selection of KLIP parameters, some self-subtraction still occurs, especially close to the star, due to the presence of disk signal in the low-order modes. This self-subtraction introduces a

bias in the scale-height, photometry, and potentially midplane measurements of the disk.

4.3.2 Flux Calibration

In practice, the flux calibration is done through the "Calibrate Photometric Flux in Pol Mode" primitive in the GPI DRP. This method uses satellite spots imprinted on the polarization cubes to conduct flux calibrations on the data (Hung et al., 2016). These satellite spots are secondary images of the star created by a periodic grid imprinted on the apodizer and are necessary for the location of the star and the extraction of flux information (Sivaramakrishnan & Oppenheimer, 2006). In polarimetric mode, these spots are extended ovals due to the chromatic nature of the spots. The satellite spot flux is determined by fitting elliptical apertures to each spot and summing the total flux spread across the spot. The flux measurement is compared to the flux of the host star in order to provide a conversion from ADUs to $\mathrm{Jy\,arcsec^{-2}}$ which is then applied to every pixel in the image. The resulting flux calibrated total intensity image is shown in Figure 4.2.

4.4 Disk Characterization

The disk around HD 110058 is optically thin and nearly edge-on. As a result, the light received by the detector originates from a column of dust integrated along the line of sight and blurred by the instrumental response. The measured surface brightness of the disk at a given radius contains contributions from light scattering off dust grains at a variety of scattering angles and semi-major axes. Thus, the observed radial structure of the disk is degenerate with dust properties. For the purposes of this paper, we do not attempt to constrain dust grain properties, but instead examine the morphological structure of the disk. We aim to examine the disk's warp and asymmetries, and their implications on the dynamical history of the system. To do so we examine the position angle (PA), midplane, scale height, and surface brightness profile of the disk in detail. The disk midplane traces the peak surface brightness along the spine of the disk as a function of the 2D projected

stellocentric radius. To trace the midplane, we use a simple, yet robust method to estimate the midplane with sub-pixel precision. The scale height and brightness profile extraction depend on this midplane position, which we determine after first establishing a coordinate system using the disk PA.

4.4.1 Position Angle

First we estimate the position angle (PA) of the disk on sky. The position angle is determined using weighted least-squares or weighted linear regression. We treat the disk as a straight line where each pixel value is sampled from distribution with some spread: the scale height, in this case. Each pixel is treated as a point with coordinates (x_i, y_i). Each point, is then assigned a weight equal to the corresponding pixel value normalized by the value of brightest pixel ($W_i = I_i/I_{max}$, where I is the pixel value). This is described in Equation 4.1.

$$\beta = (X^T W X)^{-1} X^T W y \tag{4.1}$$

Where β is the vector describing the slope and y-intercept of a line, X is a matrix of pixel positions, and y is an array of y_i positions. We isolate the inner region ($r < 0.39''$) of the disk in this calculation due to its flatness relative to the more curved outer regions of the disk. We mask out as much of the background as possible to avoid biasing the fit with other bright pixels that are not part of the disk (Fig. 4.3). Here, the position angle is determined by the inverse tangent of the slope of the best fit line along the spine. (Fig. 4.3). The uncertainties in the line parameters are calculated using Equation 4.2

$$\sigma_i = \sqrt{M_{ii}^\beta}$$
$$M^\beta = (X^T W X)^{-1} \tag{4.2}$$

The resulting PA is $154.6° \pm 1.0°$. This measurement of PA differs from the one found in Stasevic et al. (2023) by 1.5 sigma ($156.2° \pm 0.7°$). Slight differences in these measurements are can be due to small differences in the data, the measurement method, and potential biases from the particulars of self-subtraction.
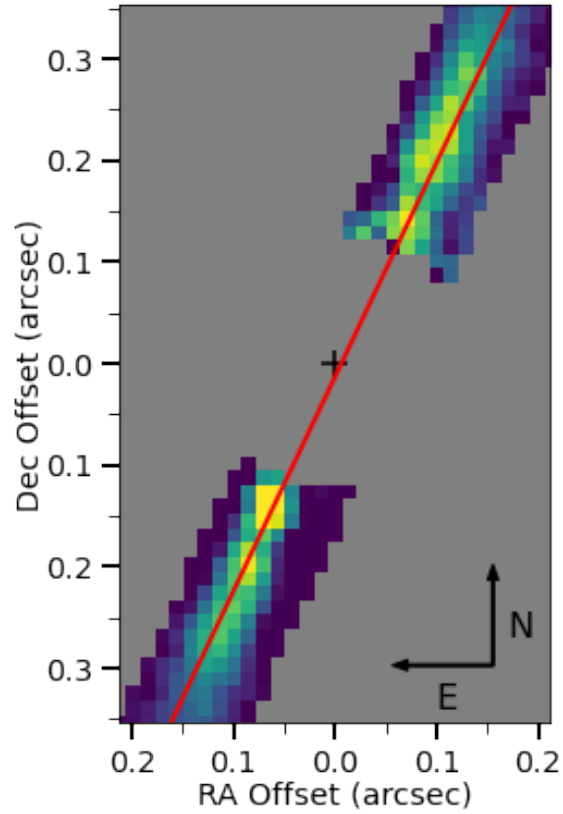
Figure 4.3: The inner region of the disk used in the calculation of the position angle. We use linear regression with the normalized pixel values as weights. The gray pixels are masked out and not included in the fit. The red line represent the best fitting slope to the midplane. This slope is then used to calculate the position angle of $154.6° \pm 1.0°$.

4.4.2 Midplane Trace

For the disk spine trace, we use the position angle calculated above to define the reference line bisecting the star and the disk (Fig. 4.4). The disk image is rotated clockwise by 64.6° (PA - 90°) to orient the bisecting line, and disk, horizontally. The full image frame is truncated to an area of 21×91 pixels ($0.3'' \times 1.4''$) to isolate the disk and limit the influence of speckle noise.

Due to the self-subtraction of the disk introduced by PSF subtraction with KLIP + ADI, pixels located close the disk may contain unphysical, negative brightness values. We therefore apply a cutoff at a value of 0 Jy arcsec^{-2} across the truncated frame. These values are not included in the analysis of the midplane. Bright speckles still present near the disk after PSF subtraction, that are not part of the main disk midplane, are manually masked out to remove their influence on the midplane trace. We then take vertical cuts of the truncated frame on a pixel by pixel basis and fit a Gaussian profile to the disk to estimate both the location of peak surface brightness and the scale height of the disk. A Gaussian surface brightness does well to fit the data, but the true profile may follow a more complex distribution dependent on the dust density distribution, viewing angle, and the GPI PSF. The profile is fully described by amplitude (A), deviation (z), and profile width (w). The amplitude of the Gaussian fit measures the peak brightness along the profile, the deviation gives an estimate for the location of peak brightness and thus the vertical deviation from a flat midplane, and the profile width gives an estimate for the scale height of the disk. The uncertainties on the "location" and thus the uncertainties on the midplane, are the FWHM/SNR of the profile. Here FWHM $= 2w$ and the SNR is the summed signal over the profile divided by the noise at the radius of the profile. In Figure 4.5, we plot the disk midplane as a function of radius, as determined by the procedure described above.
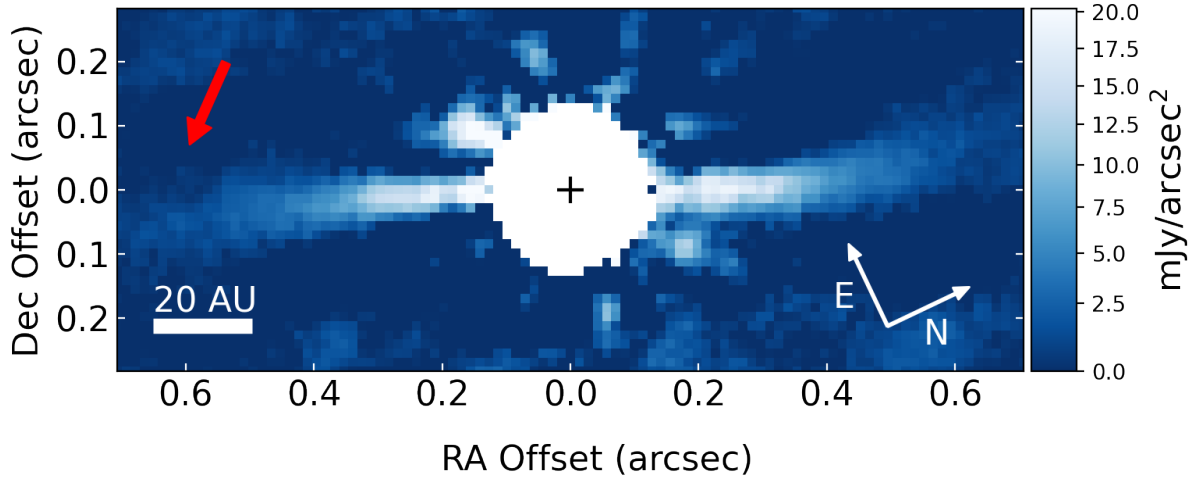
Figure 4.4: *H*-band total intensity image of the disk rotated by 64.6° clockwise from North up and East left to align the reference line with the horizontal axis. The star location is denoted by a '+'. The red arrow denotes the portion of the midplane with sudden drop off in disk brightness. We refer to this as the "notch". The scale and stretch are the same as in Fig.4.2 and the colorbar is in mJys/arcsec²

4.4.3 The Warp

The midplane shows evidence for an apparent asymmetric warp in the edge-on disk around HD 110058. The NW ansa warps northward while the opposite is true for the SE ansa, resulting in an 'S' shape. The asymmetry in the warp is seen as a stronger vertical deviation in the NW side of the disk when compared to the SE side. It is important to note the potential bias of the midplane trace due to the "notch" feature in the southeast side of the disk (4.4). This "notch" could be the location of the end of a warped inner disk and the beginning of a flat outer disk, or could be a residual artifact of PSF subtraction. There is no strong evidence for or against each scenario without further investigation. For the purposes of this paper, we will conduct the midplane analysis with these points included to avoid biasing the quantitative results, but may be important in the interpretation.

In characterizing the general shape of the warp, we fit a polynomial to the midplane positions found in Section 4.4.2. We found that a third-order polynomial was ill fitted to the asym-
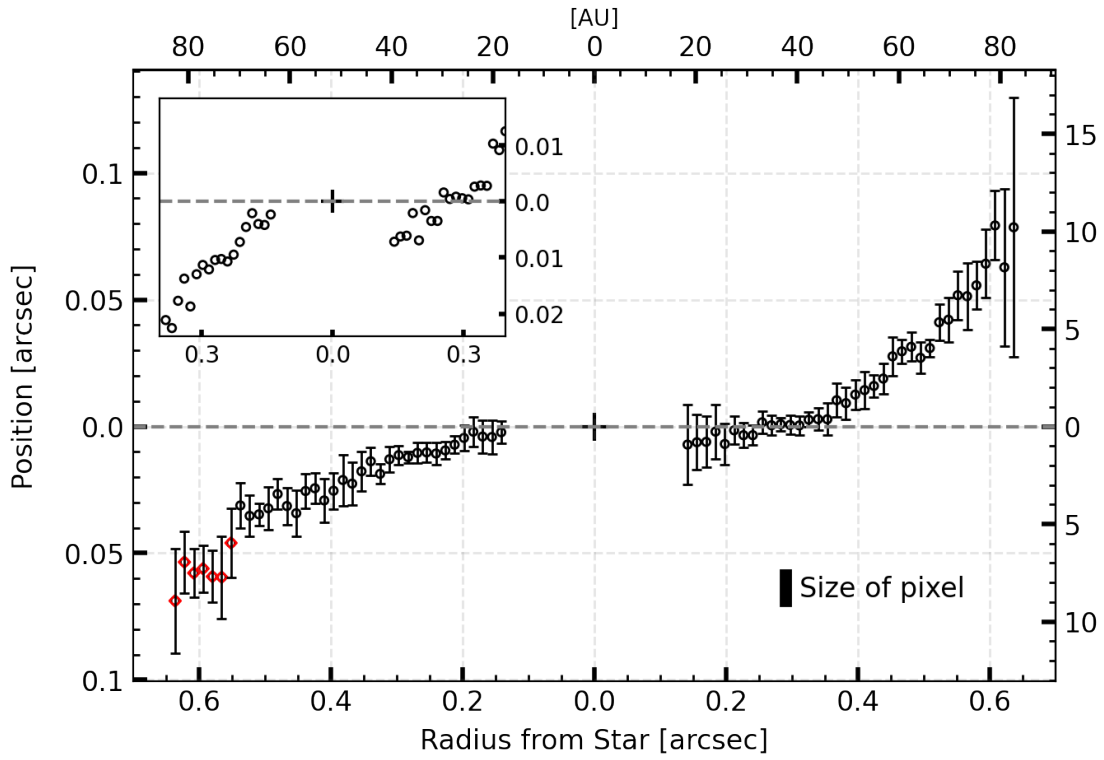
Figure 4.5: The disk midplane trace from PSF subtracted total intensity data of HD 110058 in H band. The circles denote the position of peak brightness as a function of radius from the star where error bars are calculated using the FWHM/SNR. The red points denoted potentially biased measurements due to an artifact introduced by the reduction/PSF subtraction of the data. The upper left plot is a magnified version of the midplane plot, focusing on just the inner regions of the disk. It can be seen that the two sides of the disk do not line up with each other.

metric shape of the midplane. Instead, we attempt to fit each side of the disk independently in order to characterize the asymmetry. The southeast side of the disk is sufficiently fit by a 2nd order polynomial, whereas the northwest side of the disk is better fit by a 3rd order polynomial. The northwest side of the disk curves substantially more than the southeast side, even with the bias caused by the "notch" (Fig. 4.6). Additionally, the innermost midplane points on each side of the disk do not appear to be symmetric about the star. This offset can be seen in the upper left-hand plot in Figure 4.5. This may be caused by additional wiggles in the midplane, viewing effects from an inclined and rotated disk, or an effect of the data reduction. The degree of this offset can also be dependent on the choice of reference PA as well, as there is a small error introduced by the interpolation from the rotation of the disk image. It is difficult to differentiate between these scenarios without seeing the innermost region of the disk, but Stasevic et al. (2023) report a similar misalignment, giving credence to the possibility that it is a real feature.

4.4.4 Scale Height

The scale height of the disk is measured jointly with the midplane using the half width at half maximum (HWHM) ($\sigma\sqrt{2\log 2}$) from the Gaussian profiles described in Section 4.4.2. We measure the scale height using Equation 4.3.

$$h(r) = h_0 \left(\frac{r}{r_0}\right)^{\beta} \tag{4.3}$$

Where h_0 is the scale height at $r = r_0$, and β is the flaring exponent. We find that the scale height generally increases with radius until $\sim 0.55''$ (~ 70 au) at which both the "notch" feature and noise begin to dominate. The measured scale height defined at $r_0 = 35.0$ au is $h_0 = 2.82 \pm 0.1$ au with a flaring exponent of $\beta = 0.76 \pm 0.09$ on the northwest side, and $h_0 = 2.94 \pm 0.07$ au, $\beta = 1.01 \pm 0.05$ on the southeast side. The northwest side of the disk has a smaller flaring exponent than the southeast side. This could due to speckle noise and other effects from the PSF subtraction. Effects from the self-subtraction at these radii can be seen in the brightness profile out to $0.225''$ (~ 29 au) (See Fig. 4.8). The linear

65
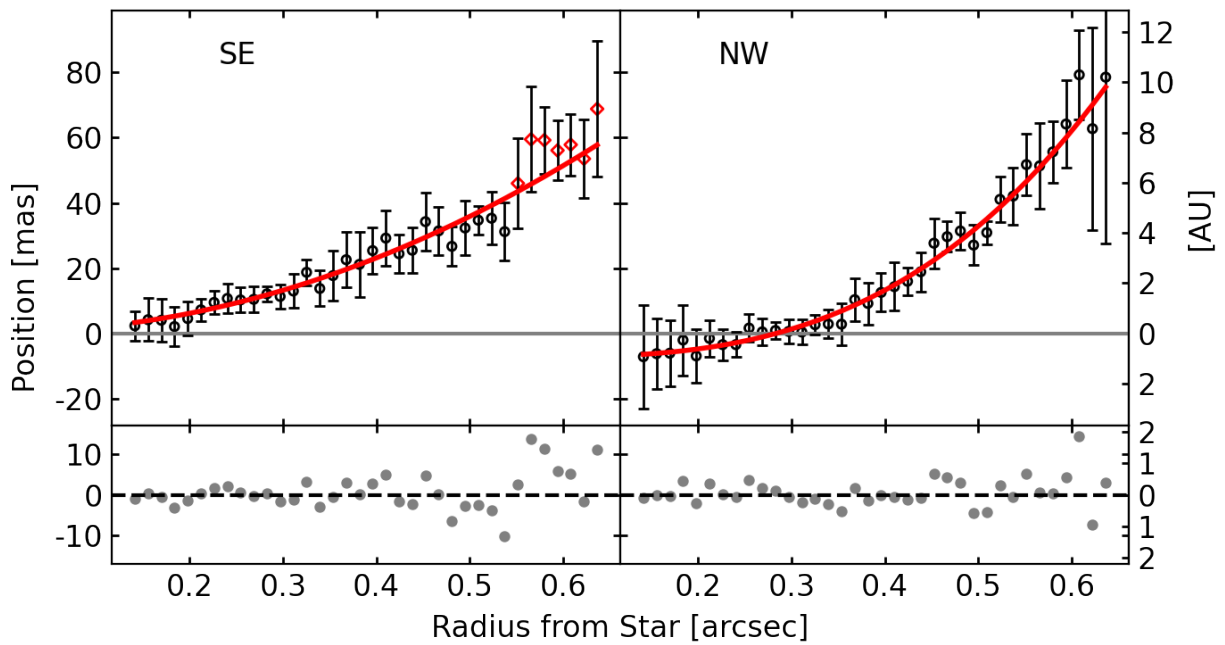
Figure 4.6: The disk midplane as a function radius from the star with independent polynomial fits with residuals. For visual comparison the southeast side of the disk is oriented such that deviations southward of the reference line are positive. The southeast side of the disk is fit with a 2nd order polynomial. The residuals of this fit show the potential bias in the midplane introduced by an artifact of the reduction. The northwest side of the disk is better fit with a 3rd order polynomial, illustrating a significant asymmetry.

increase in scale height seen in the southeast side is also convoluted. These measurements are susceptible to bias by self-subtraction, viewing effects, and effects from the warped geometry itself. However, a similar trend is found in Stasevic et al. (2023).

In general, the scale height is highly susceptible to bias from self-subtraction. Scale height measurements of the HD 32297 disk in Currie et al. (2012), Boccaletti et al. (2012), and Esposito et al. (2014) show a similar increasing trend with radius, but follow-up analysis by Duchêne et al. (2020) suggest that this is possibly caused by PSF subtraction effects that remove part of the disk signal. As such, it would be inadvisable to put strong constraints on the physical scale height without a deeper investigation into these effects. On the other hand, in the case where the "notch" is truly physical, this could be a peak at the outer edge of a potential warped inner disk. Otherwise, this feature presents a bias in the scale height measurements of the disk at $0.55''$.

4.4.5 Brightness profile

The brightness profile is a measure of the surface brightness along the disk midplane and is a function of density, 3D morphology, and grain scattering properties. The brightness profile of the disk was measured using the original non-rotated disk image. Each point in Figure 4.8 represents the summed signal of a small aperture at that radius. The size of the aperture is 8 pixels wide and 1 pixel long corresponding to an aperture area of $0.11'' \times 0.014''$. The polynomial fits from Section 4.4.3 were used to determine the centroids of each aperture. The noise was determined using apertures of the same size in a ring at the same radius as the disk signal. We sum the signal in each aperture around the ring and take the standard deviation of these measurements as the noise. The disk has a relatively low SNR, but the signal is strong enough to detect the disk out to $\sim 0.6''$. The brightness profile peaks at $\sim 0.225''$ ($\sim$29 au), but the northwest side of the disk appears slightly brighter than the southeast side out to full extent of the disk.
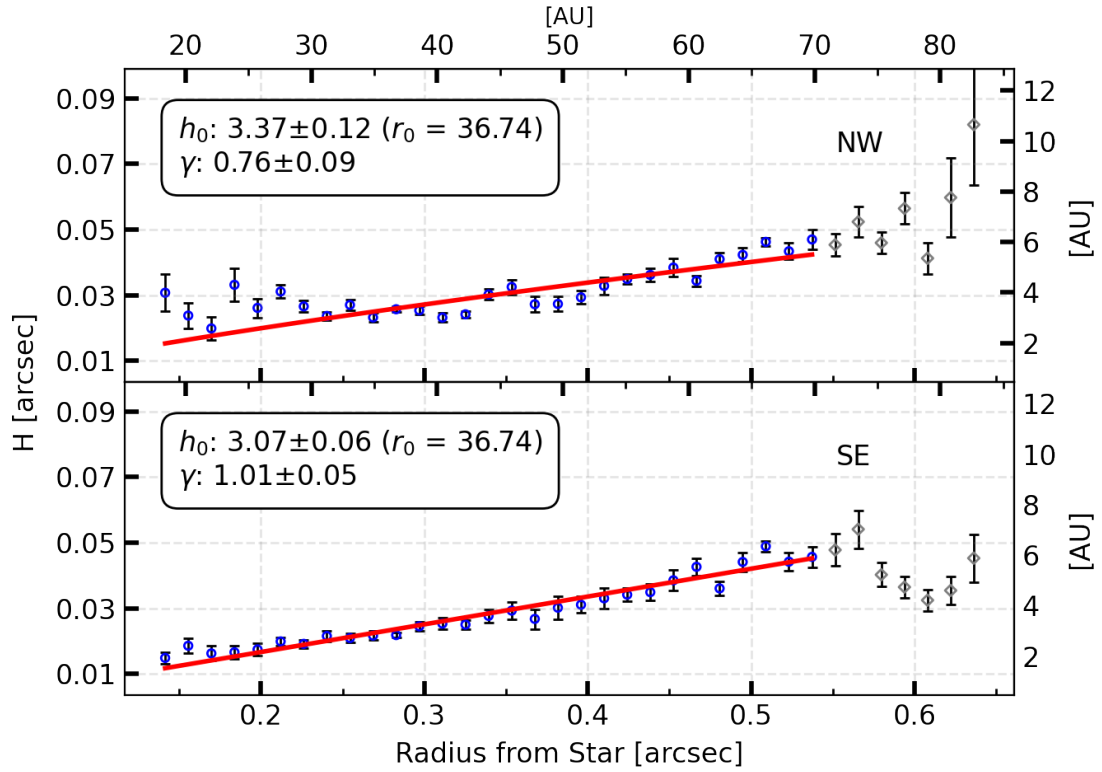
Figure 4.7: The vertical extent as a function of radius with linear fits. In blue are the measurements of the half width at half maximum (HWHM) of the disk taken from the Gaussian fits to the disk surface brightness profile. In gray are points that are omitted from the linear fit due to the influence of the reduction artifact biasing them down. This can be seen in Figure 4.4. For the remaining measurements, the scale height increases with radius, but is susceptible to self-subtraction and artifacts left over from PSF subtraction.
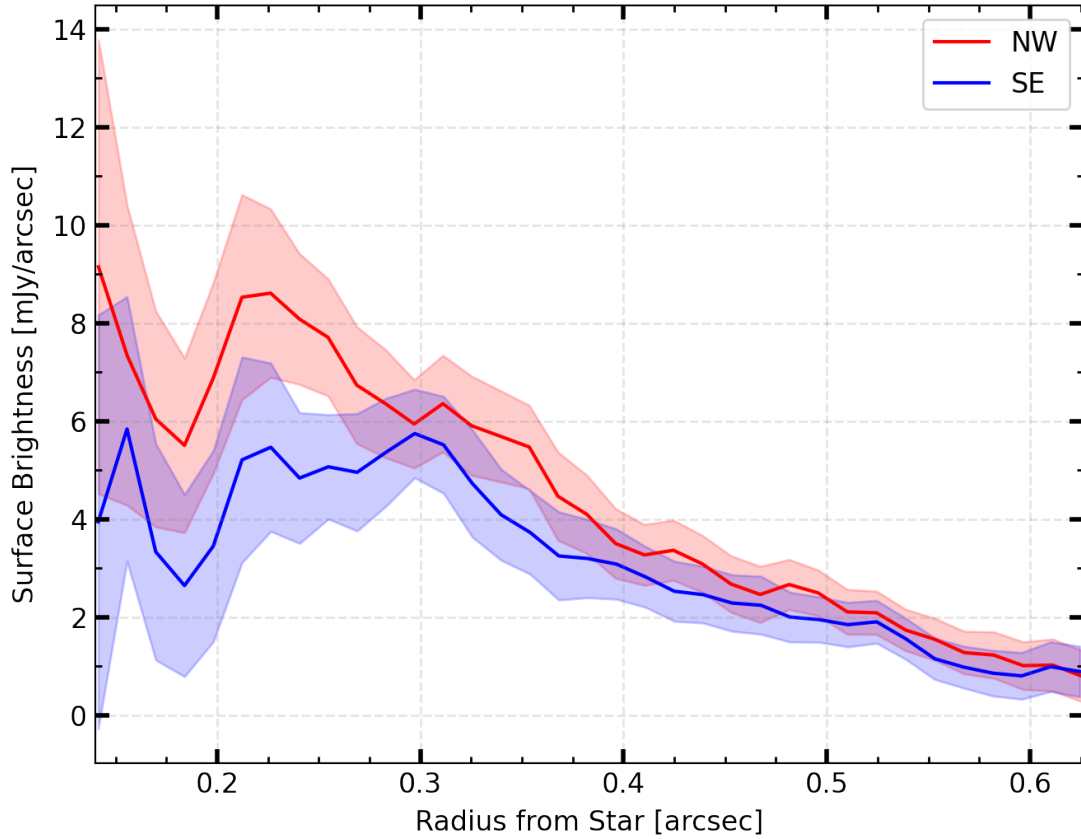
Figure 4.8: Surface brightness of the HD 110058 disk in *H*-band total intensity. The red and blue lines denote the northwest and southeast sides of the disk respectively, and the shading represents the uncertainty in these values. The brightness profile peaks at roughly the same radius for both sides of the disk at $\sim 0.225''$ ($\sim$29 au), but the brightness on northwest wide of the disk is higher. The dip in the inner region of the brightness profile is possibly caused by self-subtraction in the disk from the PSF subtraction process.

4.5 Disk Midplane Modeling

Polynomials only give a low-order approximation to 2D structure, but we want greater insight on the real structure of the disk. With the goal of characterizing 3D morphology, we explore simulated images of disk models using radiative transfer that attempt to reproduce the midplane found in the data; the purpose of this modeling is not to rigorously reproduce the disk with a physically motivated model, but instead to explore the effects of viewing angle on the perceived shape of the midplane. With this modeling, we attempt to constrain the inclination and azimuth of the disk, and deconstruct the 2D projection of the disk on sky.

4.5.1 MCFOST

For this modeling, we use `MCFOST`, which is a code that uses the Monte Carlo method to handle the full radiative transfer problem given a full 3-dimensional density distribution. We use `MCFOST` to propagate light through these distributions to simulate disk images. We first define a computational grid in which to inject a 3D dust density distribution. An input parameter file defines the model properties such as dust grain properties, star properties, and the geometry of the disk. `MCFOST` then simulates radiative transfer from the star and thermal emission from the dust grains to simulate various observables. For a more detailed description of `MCFOST`, see Pinte et al. (2006) and Pinte et al. (2009).

Here, we use `MCFOST` to simulate scattered light images of a warped debris disk that resemble the geometry of HD 110058 as viewed from Earth. in this effort, we focus only on the geometric properties of the disk. The simplified disk models are generated using four free parameters: warp strength w, inclination i, azimuth α, and deviation in position angle δPA. The warp strength is defined as the vertical deviation of the midplane from a flat disk at the critical radius r_c. The warp strength is the only parameter that affects the density distribution of the dust. The intrinsic midplane is determined using the polynomial described in Equation 4.4 where w is the warp strength, θ represents the angle around the disk in the

direction of the argument of periapsis, and z is the vertical deviation from a flat midplane.

$$z(r) = w \left(\frac{r}{r_c} \right)^3 \cos(\theta) \tag{4.4}$$

While the warp strength is not a physical property of the disk, it can be viewed as a proxy for a changing inclination distribution of dust grain orbits within the system. The inclination parameter determines the inclination of the disk relative to the observer. The azimuth parameter describes the longitude of ascending node relative to the observer. Lastly, the δPA parameter determines the rotation of the disk on sky relative to the observer.

Fitting for dust grain properties, and matching the brightness distribution of the data through forward modeling are not primary goals for this analysis. However, the dust density distribution of the models are tuned to resemble the surface brightness profile of the real data, but are only roughly estimated and fixed. The density distribution is described in Equation 4.5 (Augereau et al., 1999), and the density parameters are listed in Table (4.2).

$$\rho(r, z) = \rho_0 \left\{ \left(\frac{r}{r_c} \right)^{-2p_{\text{in}}} + \left(\frac{r}{r_c} \right)^{-2p_{\text{out}}} \right\}^{-1/2} \times \exp \left(- \left(\frac{|z|}{h(r)} \right)^{\gamma_{\text{vert}}} \right) \tag{4.5}$$

In the equation above, ρ_0 is a constant with units of density set by the mass of the disk M_{disk}, R_c is the critical radius that defines the radial density profile, p_{in}, and p_{out} define two power laws describing the increase and decrease of the density profile, and γ is the exponent of vertical density profile. $h(r)$ is defined in Equation 4.3 and z is a variable representing the vertical offset. Lastly, r_{in} and r_{out} modify the density distribution by adding sharp cutoffs to the density at their respective radii. To simulate the scattering effects of the disk, we use a Henyey-Greenstein phase function (Eq. 4.6) where θ is the scattering angle, and is parameterized by g where g equals the average of the cosine of the scattering angle ($g = \langle \cos \theta \rangle$). the g parameter determines the degree of back-scattering when negative, or forward-scattering when positive ($-1 < g < 1$).

$$p(\theta) = \frac{1}{4\pi} \frac{1 - g^2}{[1 + g^2 - 2g \cos \theta]^{3/2}} \tag{4.6}$$

Fixed Parameter	Value
r_{in} (au)	10
r_{out} (au)	100
M_{disk} ($M_\odot$)	1×10^{-10}
r_c (au)	30.0
p_{in}	2.0
p_{out}	-2.0
h_0 (au)	3.0
r_0 (au)	50.0
β	1.0
γ_{vert}	1.0
g	0.6

Table 4.2: Fixed parameters for the disk density distribution for the viewing angle model fits. This set of parameters remains constant as the viewing angle changes. r_{in} and r_{out} define the inner and outer radii, ρ_0 is a constant with units of density, R_c is the critical radius that defines the radial density profile, p_{in}, and p_{out} define two power laws describing the increase and decrease of the density profile. h_0 is the scale height defined at r_0, β is the flaring exponent, γ is the exponent of vertical density profile, and g is the Henyey-Greenstein parameter.

For a given model, we vary the four free parameters described above to generate a simulated disk image and trace its midplane using the same method described in Section 4.4.2. In this case, a Gaussian distribution does a poor job fitting the vertical profile of the disk and biases the midplane measurement. Instead, we use a Lorentzian distribution as described in Equation 4.7, where the maximum of this function is the vertical deviation of the midplane z, and the scale parameter Γ is equal to the HWHM.

$$I = I_0 \left[\frac{\Gamma^2}{(z - z_0)^2 + \Gamma^2} \right] \tag{4.7}$$

The measurement of the model's midplane is dependent not only on the 3D structure of the disk, but also on the viewing angle and orientation of the disk. We use a variety of sets of input parameters (free parameters) to generate disk images with unique midplanes and recover their synthetic midplane profiles.

4.5.2 Modeling Results

We run a grid of 54 posterior maximizing searches via chi-squared minimization, each starting from a random initial position within the range set by the uniform priors described in Table 4.3. Here, the priors have a sharp cutoff at the values listed. This technique ensures we are robust to getting stuck in local minima, and makes it more likely to find the global maximum posterior. Through this exploration of the parameter space, we discover that the posterior space is multimodal or oddly shaped. Ideally, a robust sampling of the parameter space would reveal the intricacies of this complex distribution, but a full MCMC treatment is out of the scope of this work. To account for this multimodal parameter space, we present the parameter values for each minimum along with its chi-squared value and the number of runs that converged to each specific local minimum. We select the lowest chi-squared value found via this process, which also corresponds to the minimum with the most converging points in parameter space, and use this parameter vector as our best estimate of the global maximum of the posterior. This process makes it difficult to estimate the uncertainty in the best-fit parameters, thus we report the uncertainties determined using the covariance matrix

Parameter	Prior
i (°)	$85.0 - 95.0$
α (°)	$-50.0 - 50.0$
w (au)	$0.5 - 5.0$
δPA (°)	$-3.0 - 3.0$

Table 4.3: The priors for each free parameter in the midplane chi-squared fitting process. i is inclination, w is the warp parameter , (α) is azimuth, and δPA is the deviation in position angle where 0° is horizontal.

during the exploratory phase of the fitting process. These uncertainties are representative of the local minimum and should not be taken as measures of confidence of the disk's true orientation. There are two minima found using this method. For the first minimum, 41/54 (76%) of the total runs converged to the global minimum with a chi-squared value of ∼20. For the second minimum, 13/54 (24%) of the total runs converged to a local minimum with a chi-squared value of ∼29.

Many of the model parameters affect the shape of the disk in similar ways, which can be a potential factor in the existence of multiple local minima. We discuss these modalities in the context of the parameter degeneracies in more detail in Section 4.5.3. By definition, the global minimum represents the best fitting model, however, due to the nature of the posterior distribution, other local minima may have chi-squared values very close to the global minimum. In these cases, the overall shape of the disk may look very similar to the best fitting values. This suggests that the true viewing angles of the disk cannot be constrained to one set of values using this midplane fitting method. This is most likely because either (i) random errors such as speckles or artifacts in the data the data introduced by the reduction process severely affect the disk, (ii) the disk model is overly idealized, leading to a poor fit, or most likely, (iii) a combination of both.

Figure 4.9 shows the calculated midplane generated using the best fit values for i, w, α,

w (au) at $r = 30$ au	i (°)	α (°)	δPA (°)	# converged	χ^2
2.23 ± 0.10	93.2 ± 0.4	-22.6 ± 5.4	-1.3 ± 0.2	41	20.1
2.03 ± 0.10	93.2 ± 0.4	-0.6 ± 5.4	-1.3 ± 0.2	13	29.1

Table 4.4: Best fit values for disk inclination (i), warp parameter (w), azimuth (α), and deviation in position angle (δPA). These values were generated using chi-squared minimization of the difference between the simulated midplane and the HD 110058 disk midplane. The "# converged" column refers to the amount of runs that converged to the respective local minimum. Lastly, χ^2 is the chi-squared value for the local minimum.

δPA. The resulting best fit parameters are described in Table 4.4. For the sake of clarity, we define inclination to be between 0° and 180° ($0° < i < 180°$), where $i < 90°$ corresponds to the angle where near side of the disk is above the bisecting line, and $i > 90°$ is below.

4.5.3 Degeneracies in viewing angle parameters

We explore trends in the midplane as a function of changing parameters to disentangle viewing geometry and intrinsic geometry from observed morphology. When considering the inclination of the disk, deviations from a completely edge-on orientation ($i = 90°$) result in changes to the midplane. If the disk is mostly forward scattering and the front-facing side of the disk is below the reference line, the measured midplane will shift below the reference line as well, whereas the opposite is true when the front of the disk is above the reference line (Fig. 4.10 a).

The inclination is degenerate with a Henyey-Greenstein (HG) scattering phase function. The value of the HG scattering phase function affects the amount of forward scattering that occurs in the disk. Disks with higher g values are more forward scattering, and thus, in slightly inclined disks, the surface brightness peaks further north or south than in the isotropic scattering case. This change, in turn, shifts the midplane above or below the reference line (Fig. 4.10 c and d).
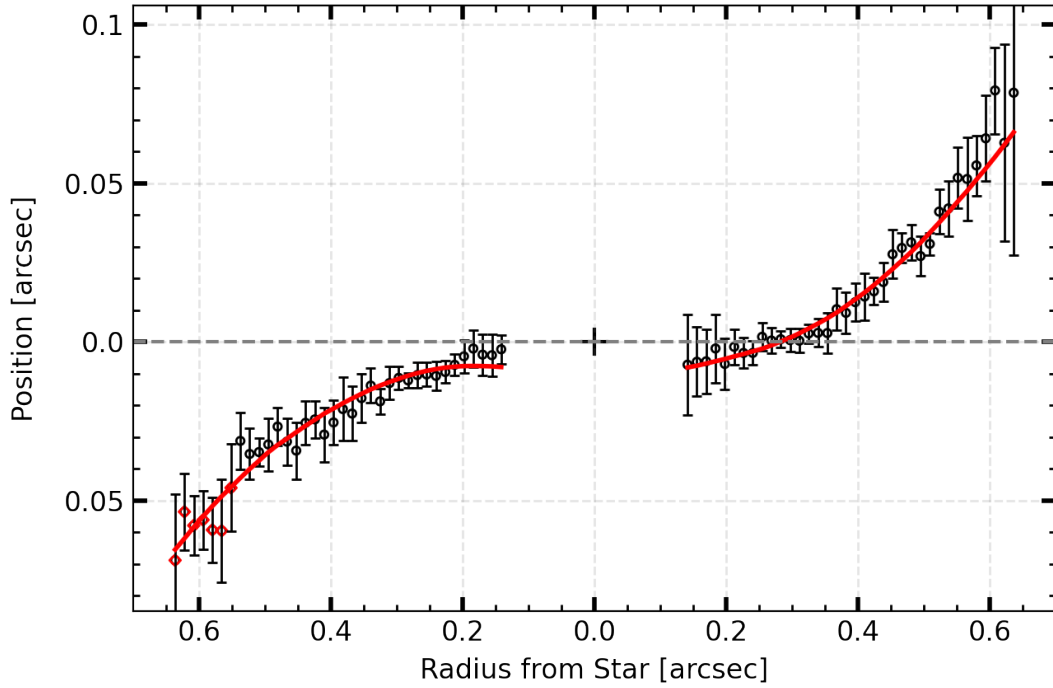
Figure 4.9: The results of midplane parameter fitting using simulated disk images. The plot shows the HD 110058 midplane (black circles) over-plotted with the midplane described by the optimized parameters: i, w, α, and δPA (red line). There appears to be no viewing angle that can fully account for the asymmetry in the disk using this family of models, and further forward modeling is required to constrain the disk properties further.

Furthermore, the warp and azimuth both play some part in determining the curvature of the warp in the midplane. The warp parameter describes how sharply the midplane deviates from the flat reference line (Fig. 4.10 e), but changes in azimuth have a similar effect. Changes in azimuth act as changes in the longitude of ascending node relative to where the warp occurs. These rotations change the integrated column of dust in the line of sight of the observer and the projection of the warped arms approach each other. This change makes the disk appear to be warped more strongly (Fig. 4.10 d).

Lastly, the disk PA rotates the entire disk midplane, but introduces slight changes in the warp strength (Fig. 4.10 b). This should not occur, as a change in δPA does not change how light propagates through the disk. Instead, this is most likely due to the surface brightness profile fitting, which is always perpendicular to the reference line, but not always perpendicular to the disk. As the disk rotates, the normal to the radius vector becomes misaligned with the orientation of the profile fit.

For our analysis, we only consider the disk midplane when determining the disk viewing geometry. This process is limited in effectiveness due to the degenerate parameters that affect the midplane. We predict that some of these degeneracies can either be broken or more tightly constrained using additional fitting parameters such as scale height, eccentricity, and surface brightness. These disk properties may rule out certain viewing angles in the disk due to a mismatch of brightness. Ultimately, we conclude that a more conclusive examination of the de-projected structure of the disk requires more in-depth forward modeling. Midplane fitting alone does not strongly constrain the disk geometry.

4.6   Physical Interpretation

In the previous section, we explored how viewing angle affects the projected shape of the midplane using simulated images of warped debris disk models. These models did well to capture the shape of the midplane and its asymmetries, but were not made to be physical.
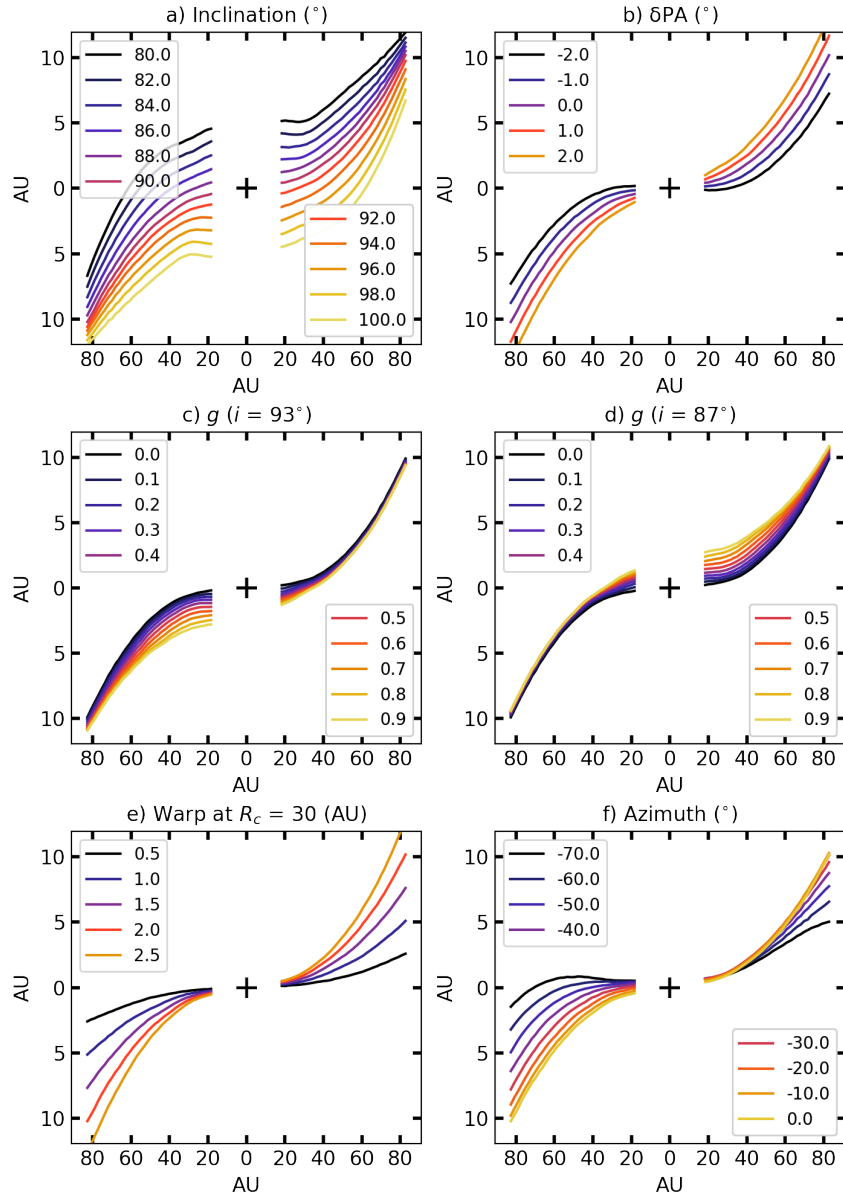
Figure 4.10: In general we plot the midplane of a model disk generated with `MCFOST` to qualitatively demonstrate how the midplane is affected by the warp and viewing angle. Each model contains an initial set of parameters that remain constant ($i_0 = 90.0°$, $\delta \text{PA}_0 = 0.0°$, $g_0 = 0.6$, $w_0 = 2.0$ au, $\alpha_0 = 0.0°$). For the testing of a specific value, the initial value is replaced with a set of test values. (a) The change in the midplane as a function of inclination. (b) The change in the midplane as a function of position angle. (c and d) The change in the midplane as a function of g for a disk of $i_0 = 93°$ and $i_0 = 87°$ respectively. (e) The change in the midplane as a function of warp strength. (f) The change in the midplane as a function of azimuth.

In this section we do not attempt to reproduce the midplane, but instead, qualitatively examine physically motivated models to give insight on the dynamics of the system. Multiple dynamical scenarios have been consistent with warps of many types. ISM interactions have been theorized to make "bowlike" warps, but the shape of these disks do not tend to resemble the asymmetric warp that HD 110058 has. Massive collisions and stellar fly-bys have the opportunity to produce asymmetric warps, but work done by Stasevic et al. (2023) show that these scenarios are unlikely. Instead, we examine the feasibility of the planet perturbing scenario as a potential cause for the warp in the HD 110058 debris disk.

4.6.1 The Secular Precession Timescale

HD 110058 appears to share morphological similarities to β Pictoris and the warped structure of the disk strongly hints at the existence of an unseen planet. In this section, we explore the planet perturbing scenario as a cause for the warp observed in HD 110058's debris disk using dynamical modeling. In particular, we examine the timescale in which a planet on a misaligned orbit induces perturbations on dust grain orbits. Over long timescales compared to the individual orbits, the gravitational force from an inclined/eccentric planet introduces so-called "secular" perturbations, which result in oscillations in the inclination and eccentricity of dust grain orbits. The timescale on which secular perturbations can warp a disk is known as the secular precession timescale t_{sec} described in Equation 4.8.

$$t_{sec} = 4\left[\alpha_p\overline{\alpha}_p b_{3/2}^1(\alpha_p)\left(\frac{a_\oplus}{a}\right)^{3/2}\left(\frac{M_p}{M_*}\right)\sqrt{\frac{M_*}{M_\odot}}\right]^{-1} \tag{4.8}$$

where $b_{3/2}^1$ is the Laplace coefficient, M_p is the mass of the perturber, a_p is the semi-major axis of the perturber, and α_p, $\overline{\alpha}_p$ are defined as such:

$$\begin{aligned}
\alpha_p &= a_p/a, \overline{\alpha}_p = 1, &&\text{for } a_p < a \\
\alpha_p &= \overline{\alpha}_p = a_p/a, &&\text{for } a_p > a
\end{aligned} \tag{4.9}$$

For a single perturber, the oscillation timescale of a dust grain's orbit increases with distance and decreases with the mass of the perturber. However, the amplitude of the oscillations is

independent of these factors, and oscillations in inclination will peak at $2I_p$ (inclination of the perturber). A planet will need to have a sufficiently large mass to create the warp in HD 110058's debris disk during the star's lifetime. In Figure 4.11 we plot the possible range of masses M_p and semi-major axes a_p of a perturbing planet capable of creating a warp at $a = 38$ au. We limit the semi-major axis to 150 au and the mass to 700 $M_\oplus$, but values outside these ranges are possible. The outermost boundary corresponds to the system age of 17 Myr, beyond which a planet will not have had enough time to warp the disk. It is important to note that both planets interior and exterior to 38 au are capable of warping the disk at that location in the secular perturbation model.

4.6.2 Dynamical Modeling

In Section 4.5 we attempt to reproduce the midplane through simulated images generated with MCFOST. The disk models used in this analysis are useful for probing the 3D structure of the disk, but do not give insight into the underlying physics of the system. In this section, we take a different approach to get at the dynamics of the system. We expand on the analysis done in the previous section by simulating the effect of secular perturbations acting on a flat disk with similar properties to HD 110058. We create simple dust density models and evolve them over 17 Myr using the analytical solution to secular perturbations caused by a single perturbing mass. Specifically, we examine two planet perturbing scenarios: a planet on an orbit interior to the disk, and a planet orbiting exterior to the disk. We construct representative models for both scenarios using secular perturbation theory and run these models through radiative transfer simulations using MCFOST. These images can then be used to qualitatively compare the dynamical models to the image of HD 110058 for the purposes of exploring the feasibility of the planet warping scenario.

The timescale of the oscillations produced by perturbations from a planet is much longer than the orbital period of a single grain of dust. As such, we can treat dust grains with the same orbit as a single ring of material, ignoring their individual true anomalies. For a
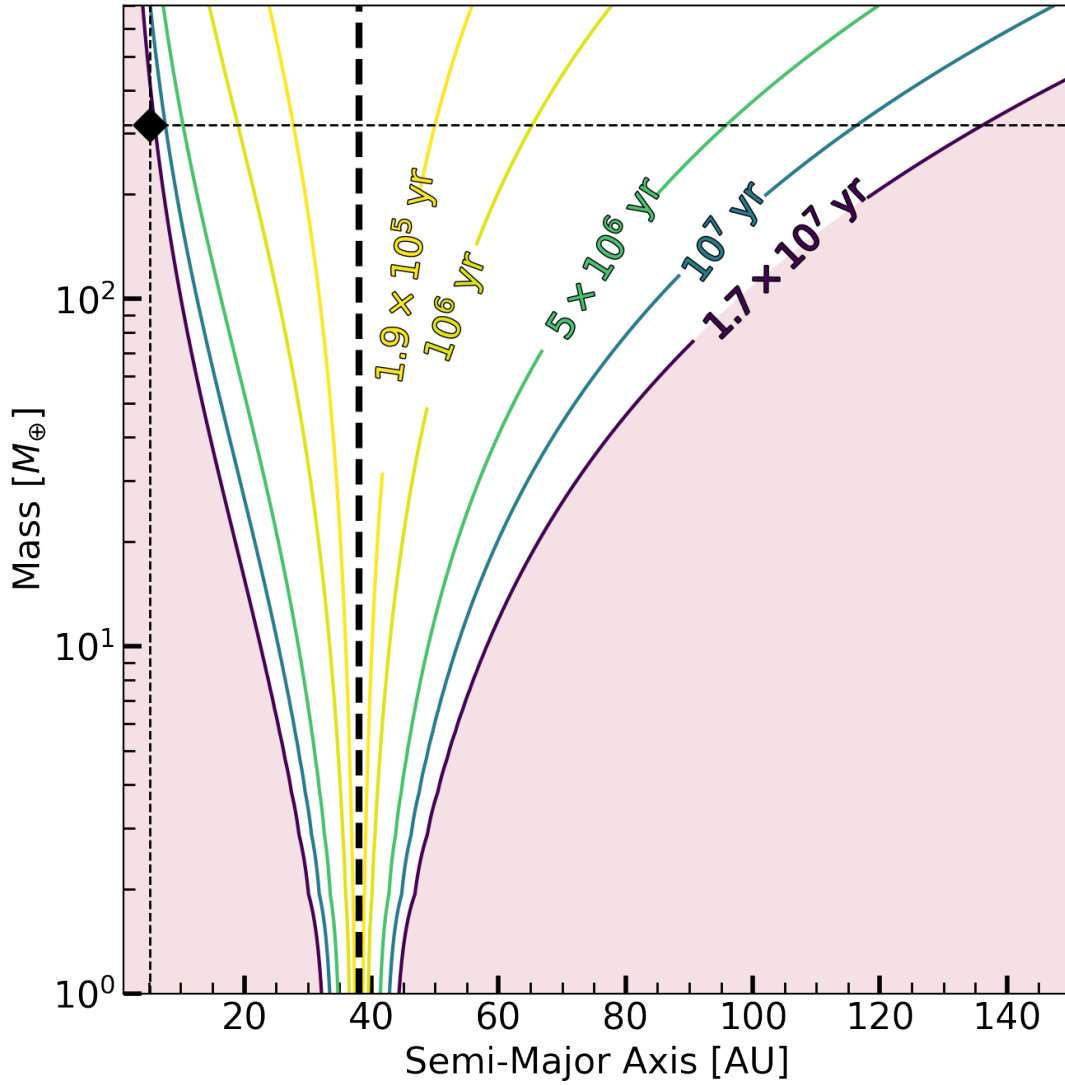
Figure 4.11: A contour diagram displaying the parameter space of allowable planet mass that could physically warp the disk at 38 au given the age of the system. The outermost, limiting contour in purple (1.7×10^7 yr) is set by the system age of 17 Myr. Anything outside of this contour, shaded in red, is ruled out by the system age. The vertical dashed line is the semi-major axis where the warp becomes prominent. The mass and semi-major axis of Jupiter are denoted with a black diamond as a reference.

ring with a mass much smaller than the mass of the perturber, we can also treat its mass as negligible for the purposes of self-gravitation and interaction. To create a warped model disk, we first construct an unperturbed flat disk made from concentric rings of dust. For the purposes of this paper, we only look at a simple model where $e = 0$. Thus, each ring has a constant radius with semi-major axis $a_{0,i}$. We can fully describe the ring using the following orbital elements: $a_{0,i}$, $I_{0,i}$, and $\Omega_{0,i}$, with $e = 0$, and ignoring the true anomaly of individual dust grains. To give the disk an intrinsic non-zero scale height, we sample the inclination $I_{0,i}$ 200 times and the longitude of ascending node $\Omega_{0,i}$ 200 times from uniform distributions. Each ring is assigned a density $\rho_i(a, i)$, which is only dependent on $a_{0,i}$ and $I_{0,i}$, using the density distribution described in Equation 4.5. The density is dependent on z which is a function of a and I. This density distribution sets the bounds for both the semi-major axis and inclination distributions of the disk. The initial conditions for the disk are described in Table 4.5.

The unperturbed rings are run through the analytical solutions describing secular perturbations caused by a single planet with properties M_p, a_p, I_p, Ω_p, and $e_p = 0$. The inclined planet induces oscillations on the complex inclinations y of dust grain orbits. A single perturber provides a constant forcing term y_{force} on the complex inclination, but the time dependence arrives from the proper term y_{prop}. In the case of a singular perturbing planet, the orbital parameters of the perturber also remain constant. The evolution of the dust grain orbits follow Equation 4.10 where I is the inclination and Ω is the longitude of ascending node.

$$y(t) = y_{force} + y_{prop}(t) = I_p e^{i(\Omega t)} + I_{prop} e^{i(-B_1 t)} \tag{4.10}$$

where

$$B_1 = \frac{n}{4 - \beta_{rad}} \left(\frac{M_p}{M_*} \right) \alpha_p \overline{\alpha}_p b_{3/2}^1(\alpha_p) \tag{4.11}$$

and

$$n = \frac{2\pi}{t_{yr}} \left[(1 - \beta_{rad}) \left(\frac{a_\oplus}{a} \right)^3 \left(\frac{M_*}{M_\odot} \right) \right]^{1/2} \tag{4.12}$$

Parameter	Value
r_{in} (au)	10
r_{out} (au)	120
ρ_0 (arbitrary)	1.0
r_c (au)	40.0
p_{in}	2.0
p_{out}	-2.0
h_0 (au)	3.0
r_0 (au)	40.0
β	1.0
γ_{vert}	1.0
g	0.0

Table 4.5: The fixed parameters defining the dust density distribution described in Equation 4.5 for the secularly perturbed models. r_{in} and r_{out} define the inner and outer radii, ρ_0 is a constant with units of density, R_c is the critical radius that defines the radial density profile, p_{in}, and p_{out} define two power laws describing the increase and decrease of the density profile. h_0 is the scale height defined at r_0, β is the flaring exponent, γ is the exponent of vertical density profile, and g is the Henyey-Greenstein parameter.
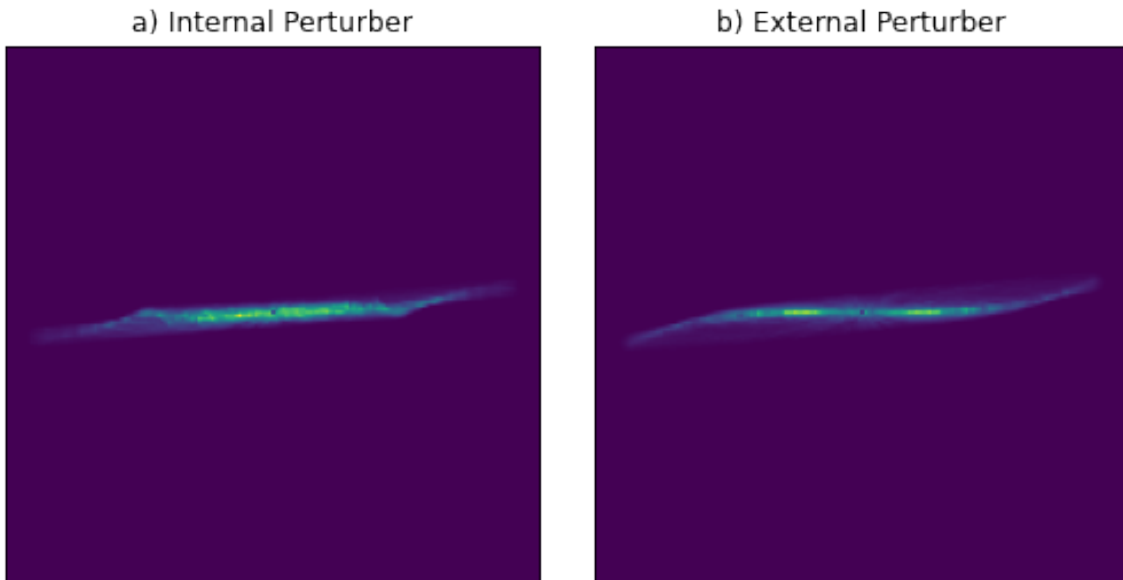
Figure 4.12: (a) Dynamical modeling with `MCFOST` for a disk with an internal perturber. (b) The same as in (a) but for an external perturber. Both scenarios warp the disk, but the shape of the disk differs slightly.

In the above equations, t_{yr} is 1 year, and β_{rad} is the ratio between radiation pressure and gravity, described in Gustafson (1994) which we define as 0.5, where grains become unbound.

Over a timescale T, each initial orbit evolves to a new set of orbital parameters $a_{f,i}$, $I_{f,i}$, $\Omega_{f,i}$, and $e_{f,i} = 0$. These new orbits are then sampled in true anomaly 1000 times throughout the full 2π radians of the orbit to create rings in 3-dimensional space. For a more in depth explanation of the secular perturbation process, see Wyatt et al. (1999).

The above ultimately constructs a 3d density distribution that can be processed through `MC-FOST` to simulate disk model images. We construct models for two disk perturbing scenarios: a planet internal to the disk and a planet external to the disk. We do not attempt to recreate and fit models to the data, but instead, use these models as tools to test the two dynamical scenarios. For simplicity, we do not consider the eccentricity of the perturber or the dust in making these models. Additionally, we convolve the disk images with a one pixel Gaussian kernel for display purposes, but all analysis is done with the original image. Here one pixel

	Mass (M_{Jup})	a (au)	I (°)	e	Ω (°)
Inner Perturber	5	6	3.0	0.0	0.0
Outer Perturber	10	600	4.0	0.0	0.0
Disk	massless	$10 - 110$	$0.0 - 0.5$	0.0	$0 - 360$

Table 4.6: Initial conditions for the disk and inner and outer perturbing planets.

has the same dimensions as one GPI pixel (14.14 mas pixel pitch). The initial conditions for the disk and perturbing planets in each case are shown in Table 4.6.

4.6.2.1 Inner Planet

An interior perturbing planet has been shown to be consistent with warping the β Pictoris disk (Lagrange et al., 2008; Dawson et al., 2011). Given the morphological similarities, there is a possibility that HD 110058's warp may also be caused by a similar dynamical history. An internal perturber induces oscillations in the inclination of dust grains near the planet. For the dust grains closest to the planet, their oscillation timescale is short enough that they oscillate many times before the grains on outer orbits have time to oscillate once. These oscillations cause the inner regions of the disk to mix together, puffing up the disk. The outer regions of the disk, on the other hand, may not have enough time to oscillate through a full period, and so these oscillations decay with radius back to a flat midplane. This structure can be seen in Figure 4.12 a. An internal perturber tilts and puffs up the inner disk relative to a flat outer disk. In Section 4.4.2 we define the position angle so that the inner regions of the disk are flat and the outer regions deviate from horizontal. To better match the model to HD 110058, we rotate the disk by 6° and as a result, the disk begins to better resemble HD 110058. Still, while this type of disk architecture is consistent with β Pictoris, it does not explain the gradual curvature of HD 110058's midplane. It is possible that the outer regions of HD 110058 ($r > 0.7''$) are not seen in the GPI data, and therefore it is possible that the outer disk does return back to a flat midplane. This is secondarily

supported by the midplane analysis done by Stasevic et al. (2023) which shows that the in the VLT/SPHERE data, the disk brightness appears to decrease as a function of radius until it cannot be seen at ~70 au while the disk imaged with HST/STIS extends out to ~150 au.

4.6.2.2 Outer Planet

Qualitatively, the externally perturbing planet scenario produces a model that resembles the data, including the gradual curvature of the midplane. A flat interior midplane with bright lobes can be seen in Figure 4.12 b, but the general increase in scale height is not reproduced in the simulated images. An external perturbing planet with a very wide orbit is capable of perturbing the outer regions of the disk while leaving the interior regions relatively untouched. An example of this is the case of HD 106906, which has a confirmed external companion consistent with orbital intricacies found in the disk (Nesvold et al., 2017; Farhat et al., 2023). For this scenario to take place, the timescale of oscillations must be long enough such that the outer regions of the disk is perturbed, but short enough such that the inner regions remain unperturbed. For a warped disk, the timescale required to induce the warp at a given radius with a given strength depends on the mass and semi-major axis of the planet. The timescale decreases with increasing planet mass and increases with increasing semi-major axis. Once again, it is important to recognize that the GPI HD 110058 disk data used as a reference is limited in field of view. Observations taken with HST/STIS show a larger outer disk unseen by GPI (Ren et al., 2023) extending out to ~150 au. An external perturber would induce oscillations on the outer disk at shorter timescales than it would on the inner disk. This perturber would also produce a "puffy" outer disk rather than an inner one. An external perturber may explain the puffy disk seen by Hubble, but the inclination of the disk ($80° < i < 84°$) reported in Stasevic et al. (2023) may also play a large part in the appearance of the disk. Additionally, planet occurrence rates are higher at closer distances to their host star than at wide orbits, and large planets on wide orbits are more likely to be seen through direct imaging, yet no such planet has been found. While this scenario

produces a disk with more similar morphology to observations than the internal perturbing case, it may be a more physically unlikely explanation for the warp.

4.7 Conclusions

In this work, we examined the overall morphology of HD 110058's debris disk using H-band total intensity images taken with GPI polarimetry mode. We find interesting and unexpected features of the disk and summarize these findings below.

1. We traced the midplane of the disk oriented at a position angle of $154.6° \pm 1.0°$ and found an asymmetry in the strength of the warp. The midplane's odd structure suggests large-scale dynamics taking place in the disk.

2. The vertical extent appears to be increasing with radius with the southeast side of the disk ($\beta = 0.76 \pm 0.09$) increasing at a steeper rate than the northwest side ($\beta = 1.01 \pm 0.05$). This difference, however, may be biased due to PSF-subtraction artifacts. Most importantly, the disk scale height for each side of the disk is roughly the same. The disk scale height was measured to be $h_0 = 2.82 \pm 0.1$ au on the northwest side and $h_0 = 2.94 \pm 0.07$ au on the southeast side with an average value of 2.88 ± 0.13 au at $r_0 = 35.0$ au.

3. The surface brightness profile peaks at $\sim 0.225''$ (~ 29 au) and decays with radius, but we found an asymmetry between the two sides of the disk. Further investigation is needed to determine if this asymmetry an be explained by the same dynamical process that creates the warp.

4. We find that fitting the midplane by varying viewing angle can produce simulated scattered light images with model midplanes consistent with that of HD 110058. The asymmetry in the warp on each side of HD 110058's disk is captured by the best fit viewing angle parameters. Concurrently, this exercise sheds light on the degeneracies

that affect our measurement of the disk and its midplane. Some of these degeneracies may be broken by including additional disk properties, such as surface brightness, scale height, and disk eccentricity, in models.

5. While viewing angle may account for some of the asymmetries in HD 110058's disk midplane, it does not account for the warp itself. Such a warp can be caused by different dynamical scenarios such as stellar fly-bys and massive collisions, but the planet perturbing scenario has been shown to be consistent with similarly warped disks. With this in mind, we put constraints on the mass and semi-major axis of planets that are consistent with the warp at 38 au.

6. We constructed disk models using secular perturbations on dust grain orbits and run them through radiative transfer simulations using `MCFOST`. The general shape of the disk is can be matched by both scenarios, but an outer perturber seems to better match the more gradual and smooth deviation seen in the data. The asymmetries however, were not captured by the dynamical modeling alone. In each case, dynamical simulations produce warped disk models with warps similar to that of HD 110058, suggesting that a planet-perturbing scenario is consistent with the warp in HD 110058's debris disk.

Future work, including forward modeling, will help illuminate the true structure of the disk. Higher signal-to-noise data from JWST and new and upgraded ground-based instruments with smaller inner working angles will help with these endeavours. Although the peculiarity of the disk presents challenges to determining the disk structure, the disk resembles others seen before. Disks such as β Pictoris and HD 106906 have warps consistent with internal or external planetary perturbers. These systems may be used as templates for insight into the dynamics of HD 110058. Overall, further study of this disk can place more detailed quantitative constraints on the possible perturber, potentially setting up HD 110058 as a target for a future planet search.

CHAPTER 5

Conclusions

I am motivated by the goal of understanding the history of exoplanetary systems and the instruments that guide us. In particular, my work contributes to the field through work in direct imaging, spectroscopy, and near-infrared instrumentation. A full picture of planet formation and planetary system evolution has yet to be completed, and much can still be learned by new observations. Through development of novel instrumentation and modern observational techniques, we can expand the number of detected and characterized exoplanets and explore new regions of the exoplanet mass/semi-major axis parameter space. These observations will require increasingly more sensitive instruments and an even better understanding of the data produced by the instruments. In this work, I present a close look into the development, improvement, and characterization of near-infrared instrumentation and discuss the science that results from these advanced instruments.

I characterized the performance of the upgraded detectors for the spectrometer (SPEC) and slit-viewing camera (SCAM) on NIRSPEC. For the SCAM detector I reported the pixel scale, and magnitude zero points for the first three NIRSPEC filters: N1, N3, and N5, as well as the first four filters with their short bandpass filters including N7. We also illustrate the geometric distortion of the SCAM detector and provide a distortion solution used to correct for optical aberrations. The characterization of the SPEC detector included a quantification of the gain, persistence, flux zero points, pixel scale, spectral dispersion, and throughputs of four NIRSPEC filters: N1, N3, N5, and N7. Upgrading the SPEC detector to an H2RG

infrared array not only improved spectral resolution through increased spectral sampling, but also increased the size of the detector and thus expanded the wavelength range of operation. I assessed the spectral performance of the detector in these new regimes, creating a map of spectral performance that can be used by observers. In the exploration of the SPEC detector readnoise and dark current, an elevated instrument background was detected, suggestive of a thermal light leak in the system. Using backward propagation of light rays, I discover possible origins of the light leak and eliminate some of these options.

We presented the design requirements and initial design concept for a Fabry-Pérot etalon calibration system for use on the OSIRIS instrument on the Keck I telescope. OSIRIS is an R~3800 near-infrared integral field spectrograph that can produce ~3000 spectra simultaneously. Such a complex instrument requires a very good understanding of each of the system's components and systematics. However, small differences between lenses and thermal instability can cause fluctuations in the light path, leading to complications in the calibration process. The layout of the tightly packed spectra can cause cross-talk between neighboring spectra, and OH lines and arc lamps do not have sufficient density and sampling to fully compensate for these effects. Proper spectral calibration of these data requires a dense grid of spectral lines, which is challenging to achieve with traditional calibration sources. An etalon calibration system is well suited to produce evenly spaced calibration lines at high densities. These lines, tuned specifically for OSIRIS, can be used to find more accurate wavelength solutions and provide PSF references that can be used to disentangle confused neighboring spectra. Adding an etalon to the calibration unit on OSIRIS will improve the overall spectral calibration process and lay the groundwork for more advanced calibration systems on future facility class integral field spectrographs such as KECK/LIGER (Wright et al., 2019).

Finally, I presented a deeper look into the total intensity images of HD 110058 debris disk, and characterize its morphology. I find that the disk is not only warped, but asymmetric

in its warp, with the northwest extent reaching a greater distance away from the bisecting line than the southeast extent. The asymmetries of the disk continue with a difference in brightness as well, though we are not yet able to determine if the asymmetry in brightness can be explained by the same dynamical processes that create the asymmetric warp. We explored the effect that viewing angle plays on the 2D projected images of the disk to disentangle the degeneracies between true morphological properties and projection effects on the disk. We found that many of the effects caused by viewing angles are degenerate with one another and that additional properties, such as disk brightness are needed to disentangle the projection effects from the true shape of the disk. Despite this, there remains strong evidence for the presence of a planet responsible for the warp in HD 110058's disk. We explored the effects of both an inner and outer planet on the disk, and found that both scenarios produce disk properties found in the data.

I have presented novel contributions to the development, upkeep, and improvement of instrumentation. These projects were chosen to advance the field of extrasolar system science through both instrumentation and observation. In turn they will improve our ability to answer increasingly complex questions and inform new theoretical models of planet formation. These works act as steps towards the ultimate goal of finding signs of life through the imaging and characterization of Earth-like planets around Sun-like stars.

Bibliography

Augereau, J. C., Lagrange, A. M., Mouillet, D., Papaloizou, J. C. B., & Grorod, P. A. 1999, A&A, 348, 557, doi: 10.48550/arXiv.astro-ph/9906429

Bean, J. L., Raymond, S. N., & Owen, J. E. 2021, Journal of Geophysical Research (Planets), 126, e06639, doi: 10.1029/2020JE006639

Beuzit, J. L., Vigan, A., Mouillet, D., et al. 2019, A&A, 631, A155, doi: 10.1051/0004-6361/201935251

Blank, R., Anglin, S., Beletic, J. W., et al. 2012, in High Energy, Optical, and Infrared Detectors for Astronomy V, ed. A. D. Holland & J. W. Beletic, Vol. 8453, International Society for Optics and Photonics (SPIE), 280 – 295, doi: 10.1117/12.926752

Boccaletti, A., Augereau, J. C., Lagrange, A. M., et al. 2012, A&A, 544, A85, doi: 10.1051/0004-6361/201219320

Buenzli, E., Thalmann, C., Vigan, A., et al. 2010, A&A, 524, 1, doi: 10.1051/0004-6361/201015799

Burns, J. A., Soter, S., & Lamy, P. L. 1976, in Bulletin of the American Astronomical Society, Vol. 8, 471–472

Chen, C. H., Pecaut, M., Mamajek, E. E., Su, K. Y. L., & Bitner, M. 2012, ApJ, 756, 133, doi: 10.1088/0004-637X/756/2/133

Chen, C. H., Sargent, B. A., Bohac, C., et al. 2006, ApJS, 166, 351, doi: 10.1086/505751

Crotts, K., & Matthews, B. 2023, in American Astronomical Society Meeting Abstracts, Vol. 55, American Astronomical Society Meeting Abstracts, 154.03

Currie, T., Rodigas, T. J., Debes, J., et al. 2012, ApJ, 757, 28, doi: 10.1088/0004-637X/757/1/28

Dawson, R. I., Murray-Clay, R. A., & Fabrycky, D. C. 2011, ApJ, 743, L17, doi: 10.1088/2041-8205/743/1/L17

Debes, J. H., Weinberger, A. J., & Kuchner, M. J. 2009, ApJ, 702, 318, doi: 10.1088/0004-637X/702/1/318

Dohnanyi, J. S. 1969, J. Geophys. Res., 74, 2531, doi: 10.1029/JB074i010p02531

Duchêne, G., Rice, M., Hom, J., et al. 2020, AJ, 159, 251, doi: 10.3847/1538-3881/ab8881

Dugan, O., Robinson, T., Carmeci, F., & Tock, K. 2019, Journal of Double Star Observations, 15, 119

Esposito, T. M., Fitzgerald, M. P., Graham, J. R., & Kalas, P. 2014, ApJ, 780, 25, doi: 10.1088/0004-637X/780/1/25

Esposito, T. M., Fitzgerald, M. P., Graham, J. R., et al. 2016, The Astronomical Journal, 152, 85, doi: 10.3847/0004-6256/152/4/85

Esposito, T. M., Kalas, P., Fitzgerald, M. P., et al. 2020, AJ, 160, 24, doi: 10.3847/1538-3881/ab9199

Farhat, M. A., Sefilian, A. A., & Touma, J. R. 2023, MNRAS, 521, 2067, doi: 10.1093/mnras/stad316

Gaia Collaboration. 2022, VizieR Online Data Catalog, I/355

Groff, T. D., Kasdin, N. J., Limbach, M. A., et al. 2015, in Society of Photo-Optical Instrumentation Engineers (SPIE) Conference Series, Vol. 9605, Techniques and Instrumentation for Detection of Exoplanets VII, ed. S. Shaklan, 96051C, doi: 10.1117/12.2188465

Gustafson, B. A. S. 1994, Annual Review of Earth and Planetary Sciences, 22, 553, doi: 10.1146/annurev.ea.22.050194.003005

Hales, A. S., Barlow, M. J., Crawford, I. A., & Casassus, S. 2017, MNRAS, 466, 3582, doi: 10.1093/mnras/stw3274

Hales, A. S., Marino, S., Sheehan, P. D., et al. 2022, ApJ, 940, 161, doi: 10.3847/1538-4357/ac9cd3

Heap, S. R., Lindler, D. J., Lanz, T. M., et al. 2000, The Astrophysical Journal, 435, doi: 10.1086/309188

Hercher, M. 1968, Appl. Opt., 7, 951, doi: 10.1364/AO.7.000951

Hernandez, G. 1988, Fabry-Perot Interferometers, Cambridge Studies in Modern Optics (Cambridge University Press). https://books.google.com/books?id=og7uKhM01K8C

Hines, D. C., Schneider, G., Hollenbach, D., et al. 2007, The Astrophysical Journal, 671, L165, doi: 10.1086/525016

Hughes, A. M., Duchêne, G., & Matthews, B. C. 2018a, ARA&A, 56, 541, doi: 10.1146/annurev-astro-081817-052035

—. 2018b, ARA&A, 56, 541, doi: 10.1146/annurev-astro-081817-052035

Hung, L.-W., Bruzzone, S., Millar-Blanchaer, M. A., et al. 2016, in (International Society for Optics and Photonics), 99083A, doi: 10.1117/12.2233665

Ismail, N., Calil Kores, C., Geskus, D., & Pollnau, M. 2016, Optics Express, 24, 16366, doi: 10.1364/OE.24.016366

Jang-Condell, H., Chen, C. H., Mittal, T., et al. 2015, ApJ, 808, 167, doi: 10.1088/0004-637X/808/2/167

Jovanovic, N., Martinache, F., Guyon, O., et al. 2015, PASP, 127, 890, doi: 10.1086/682989

Kalas, P., & Jewitt, D. 1995, The Astronomical Journal, 110, 794, doi: 10.1086/117565

Kasper, M., Apai, D., Wagner, K., & Robberto, M. 2015, Astrophysical Journal Letters, 812, L33, doi: 10.1088/2041-8205/812/2/L33

Lagrange, A.-M., Gratadour, D., Chauvin, G., et al. 2008, Astronomy & Astrophysics, 493, L21, doi: 10.1051/0004-6361:200811325

Larkin, J., Barczys, M., Krabbe, A., et al. 2006, in Society of Photo-Optical Instrumentation Engineers (SPIE) Conference Series, Vol. 6269, Society of Photo-Optical Instrumentation Engineers (SPIE) Conference Series, ed. I. S. McLean & M. Iye, 62691A, doi: 10.1117/12.672061

Larkin, J. E., Quirrenbach, A., Krabbe, A., et al. 2003, in Society of Photo-Optical Instrumentation Engineers (SPIE) Conference Series, Vol. 4841, Instrument Design and Performance for Optical/Infrared Ground-based Telescopes, ed. M. Iye & A. F. M. Moorwood, 1600–1610, doi: 10.1117/12.461775

Lee, E. J., & Chiang, E. 2016, ApJ, 827, 125, doi: 10.3847/0004-637X/827/2/125

Libralato, M., Bellini, A., Bedin, L. R., et al. 2014, A&A, 563, A80, doi: 10.1051/0004-6361/201322059

Lieman-Sifry, J., Hughes, A. M., Carpenter, J. M., et al. 2016, ApJ, 828, 25, doi: 10.3847/0004-637X/828/1/25

Lissauer, J. J. 1993, Annual Review of Astronomy and Astrophysics, 31, 129, doi: 10.1146/annurev.aa.31.090193.001021

López, R. A., von Raesfeld, C., Fitzgerald, M. P., & Do, T. 2022, in Society of Photo-Optical

Instrumentation Engineers (SPIE) Conference Series, Vol. 12184, Ground-based and Airborne Instrumentation for Astronomy IX, ed. C. J. Evans, J. J. Bryant, & K. Motohara, 121845O, doi: 10.1117/12.2629505

López, R. A., Hoffman, E. B., Doppmann, G., et al. 2020, in Society of Photo-Optical Instrumentation Engineers (SPIE) Conference Series, Vol. 11447, Ground-based and Airborne Instrumentation for Astronomy VIII, ed. C. J. Evans, J. J. Bryant, & K. Motohara, 114476B, doi: 10.1117/12.2563075

Macintosh, B., Graham, J., Palmer, D., et al. 2006, in Society of Photo-Optical Instrumentation Engineers (SPIE) Conference Series, Vol. 6272, Society of Photo-Optical Instrumentation Engineers (SPIE) Conference Series, ed. B. L. Ellerbroek & D. Bonaccini Calia, 62720L, doi: 10.1117/12.672430

Macintosh, B., Graham, J. R., Ingraham, P., et al. 2014, Proceedings of the National Academy of Science, 111, 12661, doi: 10.1073/pnas.1304215111

Maire, J., Perrin, M. D., Doyon, R., et al. 2010, in Society of Photo-Optical Instrumentation Engineers (SPIE) Conference Series, Vol. 7735, Ground-based and Airborne Instrumentation for Astronomy III, ed. I. S. McLean, S. K. Ramsay, & H. Takami, 773531, doi: 10.1117/12.858028

Maness, H. L., Kalas, P., Peek, K. M., et al. 2009, Astrophysical Journal, 707, 1098, doi: 10.1088/0004-637X/707/2/1098

Mannings, V., & Barlow, M. J. 1998, ApJ, 497, 330, doi: 10.1086/305432

Marois, C., Lafrenière, D., Doyon, R., Macintosh, B., & Nadeau, D. 2006, ApJ, 641, 556, doi: 10.1086/500401

Martin, E. C., Fitzgerald, M. P., McLean, I. S., et al. 2014, in Ground-based and Airborne

Instrumentation for Astronomy V, ed. S. K. Ramsay, I. S. McLean, & H. Takami, Vol. 9147, International Society for Optics and Photonics (SPIE), 2559 – 2565, doi: `10.1117/12.2056896`

Martin, E. C., Fitzgerald, M. P., McLean, I. S., et al. 2018, in Ground-based and Airborne Instrumentation for Astronomy VII, ed. C. J. Evans, L. Simard, & H. Takami, Vol. 10702, International Society for Optics and Photonics (SPIE), 63 – 74, doi: `10.1117/12.2312266`

Mayor, M., & Queloz, D. 1995, Nature, 378, 355, doi: `10.1038/378355a0`

Mazoyer, J., Arriaga, P., Hom, J., et al. 2020, in Society of Photo-Optical Instrumentation Engineers (SPIE) Conference Series, Vol. 11447, Ground-based and Airborne Instrumentation for Astronomy VIII, ed. C. J. Evans, J. J. Bryant, & K. Motohara, 1144759, doi: `10.1117/12.2560091`

McLean, I. S. 2005, in High Resolution Infrared Spectroscopy in Astronomy, ed. H. U. Käufl, R. Siebenmorgen, & A. F. M. Moorwood (Berlin, Heidelberg: Springer Berlin Heidelberg), 25–36

McLean, I. S., Graham, J. R., Becklin, E. E., et al. 2000, in Optical and IR Telescope Instrumentation and Detectors, ed. M. Iye & A. F. M. Moorwood, Vol. 4008, International Society for Optics and Photonics (SPIE), 1048 – 1055, doi: `10.1117/12.395422`

McLean, I. S., Becklin, E. E., Bendiksen, O., et al. 1998, in Infrared Astronomical Instrumentation, ed. A. M. Fowler, Vol. 3354, International Society for Optics and Photonics (SPIE), 566 – 578, doi: `10.1117/12.317283`

Meshkat, T., Bailey, V. P., Su, K. Y. L., et al. 2015, ApJ, 800, 5, doi: `10.1088/0004-637X/800/1/5`

Mieda, E., Wright, S. A., Larkin, J. E., et al. 2014, PASP, 126, 250, doi: `10.1086/675784`

Moór, A., Ábrahám, P., Derekas, A., et al. 2006, ApJ, 644, 525, doi: 10.1086/503381

Mortara, L., & Fowler, A. 1981, in Society of Photo-Optical Instrumentation Engineers (SPIE) Conference Series, Vol. 290, Society of Photo-Optical Instrumentation Engineers (SPIE) Conference Series, 28, doi: 10.1117/12.965833

Mouillet, D., Larwood, J. D., Papaloizou, J. C. B., & Lagrange, A. M. 1997, doi: 10.1093/mnras/292.4.896

Nesvold, E. R., Naoz, S., & Fitzgerald, M. P. 2017, ApJ, 837, L6, doi: 10.3847/2041-8213/aa61a7

Palik, E. D., Boukari, H., & Gammon, R. W. 1996, Appl. Opt., 35, 38, doi: 10.1364/AO.35.000038

Pan, M., & Schlichting, H. E. 2012, ApJ, 747, 113, doi: 10.1088/0004-637X/747/2/113

Pedregosa, F., Varoquaux, G., Gramfort, A., et al. 2011, Journal of Machine Learning Research, 12, 2825

Perrin, M. D., Maire, J., Ingraham, P., et al. 2014, in Society of Photo-Optical Instrumentation Engineers (SPIE) Conference Series, Vol. 9147, Ground-based and Airborne Instrumentation for Astronomy V, ed. S. K. Ramsay, I. S. McLean, & H. Takami, 91473J, doi: 10.1117/12.2055246

Pinte, C., Harries, T. J., Min, M., et al. 2009, A&A, 498, 967, doi: 10.1051/0004-6361/200811555

Pinte, C., Ménard, F., Duchêne, G., & Bastien, P. 2006, A&A, 459, 797, doi: 10.1051/0004-6361:20053275

Rao, Y. J., Ran, Z. L., & Deng, H. Y. 2008, in OFC/NFOEC 2008 - 2008 Conference on

Optical Fiber Communication/National Fiber Optic Engineers Conference, 1–3, doi: `10.1109/OFC.2008.4528552`

Rao, Y. J., Zhu, T., Yang, X. C., & Duan, D. W. 2007, Opt. Lett., 32, 2662, doi: `10.1364/OL.32.002662`

Ren, B. B., Rebollido, I., Choquet, É., et al. 2023, A&A, 672, A114, doi: `10.1051/0004-6361/202245458`

Rivera, E. J., & Lissauer, J. J. 2001, ApJ, 558, 392, doi: `10.1086/322477`

Rousselot, P., Lidman, C., Cuby, J. G., Moreels, G., & Monnet, G. 2000, A&A, 354, 1134

Schlimmer, J. 2015, Journal of Double Star Observations, 11, 149

Sivaramakrishnan, A., & Oppenheimer, B. R. 2006, The Astrophysical Journal, 647, 620, doi: `10.1086/505192`

Smith, B. A., & Terrile, R. J. 1984, Science (New York, N.Y.), 226, 1421, doi: `10.1126/science.226.4681.1421`

Snellen, I., de Kok, R., Birkby, J. L., et al. 2015, A&A, 576, A59, doi: `10.1051/0004-6361/201425018`

Soummer, R., Pueyo, L., & Larkin, J. 2012, doi: `10.1088/2041-8205/755/2/L28`

Stasevic, S., Milli, J., Mazoyer, J., et al. 2023, arXiv e-prints, arXiv:2308.05613, doi: `10.48550/arXiv.2308.05613`

Stevenson, D. J. 1982, Planet. Space Sci., 30, 755, doi: `10.1016/0032-0633(82)90108-8`

Sylvester, R. J., Dunkin, S. K., & Barlow, M. J. 2001, MNRAS, 327, 133, doi: `10.1046/j.1365-8711.2001.04672.x`

Tokunaga, A. T., & Vacca, W. D. 2005, The Publications of the Astronomical Society of the Pacific, 117, 421, doi: 10.1086/429382

Wahhaj, Z., Liu, M. C., Nielsen, E. L., et al. 2013, ApJ, 773, 179, doi: 10.1088/0004-637X/773/2/179

Wang, J. J., Graham, J. R., Pueyo, L., et al. 2016, The Astronomical Journal, 152, 97, doi: 10.3847/0004-6256/152/4/97

Williams, J. P., & Cieza, L. A. 2011, Annual Review of Astronomy and Astrophysics, 49, 67, doi: 10.1146/annurev-astro-081710-102548

Wright, S., Larkin, J. E., Jones, T., et al. 2019, in Bulletin of the American Astronomical Society, Vol. 51, 201

Wyatt, M. C., Dermott, S. F., Telesco, C. M., et al. 1999, ApJ, 527, 918, doi: 10.1086/308093

Wyatt, M. C., Dermott, S. F., Telesco, C. M., et al. 1999, The Astrophysical Journal, 527, 918, doi: 10.1086/308093

Wyatt, M. C., Panić, O., Kennedy, G. M., & Matrà, L. 2015, Astrophysics and Space Science, 357, 103, doi: 10.1007/s10509-015-2315-6